

# Shell Model Monte Carlo Methods

S.E. Koonin, D.J. Dean<sup>†</sup> and K. Langanke

*W.K. Kellogg Radiation Laboratory, California Institute of Technology,  
Pasadena CA 91125 USA*

## *Abstract*

We review quantum Monte Carlo methods for dealing with large shell model problems. These methods reduce the imaginary-time many-body evolution operator to a coherent superposition of one-body evolutions in fluctuating one-body fields; the resultant path integral is evaluated stochastically. We first discuss the motivation, formalism, and implementation of such Shell Model Monte Carlo (SMMC) methods. There then follows a sampler of results and insights obtained from a number of applications. These include the ground state and thermal properties of *pf*-shell nuclei, the thermal and rotational behavior of rare-earth and  $\gamma$ -soft nuclei, and the calculation of double beta-decay matrix elements. Finally, prospects for further progress in such calculations are discussed.

<sup>†</sup> Present address: Physics division, Oak Ridge National Laboratory, P.O. Box 2008, Oak Ridge, Tennessee 37831, U.S.A.

# 1 Introduction

The description of nuclear structure began more than 60 years ago with the discovery of the neutron. Major milestones were the discovery of single-particle shells [1], collective motion [2], and their reconciliation [3]. However, a number of recent developments impose new and more stringent tests of our ability to describe nuclear structure. Heavy-ion induced reactions allow the study of nuclear behavior at extremes of temperature, angular momentum, or isospin [4]. Increasingly precise experiments with electron [5], pion [6], kaon [7, 8], and nucleon [9, 10] beams probe new modes of excitation. As our understanding of supernovae [11] and nucleosynthesis [12] is refined there is a corresponding need to know more precisely the relevant nuclear properties. And new pictures of nuclear structure such as the Interacting Boson Model [13] make implicit or explicit assumptions about the solutions of the underlying fermion problem that demand verification.

The range and diversity of nuclear behavior (perhaps the greatest of any quantal many-body system) have naturally engendered a host of models. Short of a complete solution to the many-nucleon problem [14], the interacting shell model is widely regarded as the most broadly capable description of low-energy nuclear structure, and the one most directly traceable to the fundamental many-body problem. Many studies have demonstrated that exact diagonalizations of shell-model Hamiltonians can accurately and consistently describe a wide range of nuclear properties, *if* the many-body basis is sufficiently large. Pioneering papers include work in the  $0p$  [15],  $0s-1d$  [16] and  $0f_{7/2}$  [17] shells; more recent examples are [18, 19, 20]. Unfortunately, the combinatorial scaling of the many-body space with the size of the single particle basis or the number of valence nucleons restricts such exact diagonalizations to either light nuclei or to heavier nuclei with only a few valence particles [21].

The Shell Model Monte Carlo (SMMC) methods that have been developed in the past few years circumvent some of these difficulties while retaining the rigor, flexibility, and predictive power of traditional shell model calculations. These methods are based on a Monte Carlo evaluation of the path integral obtained by a Hubbard-Stratonovich (HS) transformation [22] of the imaginary-time evolution operator. The many-body problem is thus reduced to a set of one-body problems in fluctuating auxiliary fields [23]. The method enforces the Pauli principle exactly, and the storage and computation time scale gently with the single-particle basis or the number of particles. Auxiliary field methods have been applied to condensed matter systems such as the Hubbard Model [24, 25], yielding important information about electron correlations and magnetic properties.

A series of papers [26, 27, 28, 29] have described the development of SMMC methods. The purpose of the present exposition is to summarize, in one document, the philosophy, formalism, numerical methods, and computational implementation of these techniques. A coherent presentation is particularly useful, as there is a growing body of experience in such calculations and there have been a few missteps along the way. We also offer a sampler of “first-of” calculations that illustrate the power and limitations of the SMMC approach, as well as some interesting physics; some of the results presented have not been published previously.

Our presentation is organized as follows. In section 2 we review the rationale and definition of the interacting shell model, some of the important characteristics of the two-body

interaction, and discuss some of the successes that direct diagonalization calculations have had in describing a broad range of nuclear properties. In section 3, we give an overview of SMMC methods, showing how the HS transformation can be used to express physically interesting observables as ratios of high-dimensional integrals. In section 4, we discuss the various ways in which a realistic shell model hamiltonian can be cast in a form suitable for the HS transform. Section 5 is devoted to a summary of the relevant aspects of MC quadrature. In section 6, we discuss various details of implementation: subtleties of the algorithm, numerical issues, and computational implementation. In section 7 we discuss the notorious sign problems and a practical method for their solution as well as the validation of the overall method. Section 8 is a sampler of various types of SMMC calculations (virtually all intractable by other methods), and in section 9 we offer a perspective on future work. A brief appendix is devoted to the relevant properties of independent-fermion quantum mechanics. Our review covers work through December, 1995.

## 2 Review of the shell model

In this section, we present a brief definition and overview of the nuclear shell model. Our goals are to establish conventions and notation and to give the non-expert some appreciation for the special features of the nuclear problem relative to other quantal many-body systems. More detailed discussions can be found in several texts [3, 30, 31, 32, 33].

The notion of independent particles moving in a common one-body potential is central to our description of atoms, metals, and hadrons. It is also realized in nuclei, and the shell structure associated with the magic numbers was first put on a firm basis in 1949, when the magic numbers were explained by an harmonic oscillator spectrum with a strong, inverted (with respect to the atomic case) spin-orbit potential [1].

But nuclei differ from the other quantal systems cited above in that the residual interaction between the valence fermions is strong and so severely perturbs the naive single-particle picture. This interaction mixes together many different configurations to produce the true eigenstates and, because of its coherence, there emerge phenomena such as pairing, modification of sum rules, deformation, and collective rotations and vibrations. An accurate treatment of the residual interaction is therefore essential to properly describe nuclei.

The nuclear shell model is defined by a set of spin-orbit coupled single-particle states with quantum numbers  $ljm$  denoting the orbital angular momentum ( $l$ ) and the total angular momenta ( $j$ ) and its  $z$ -component,  $m$ . Although non-spherical one-body potentials are a common efficiency used in describing deformed nuclei, for the rotationally invariant hamiltonians used in SMMC so far, these states have energies  $\varepsilon_{lj}$  that are independent of  $m$ . The single-particle states and energies may be different for neutrons and protons, in which case it is convenient to include also the isospin component  $t_3 = \pm 1/2$  in the state description. We will use the label  $\alpha$  for the set of quantum numbers  $ljm$  or  $ljmt_3$ , as appropriate.

The particular single-particle states included in a given calculation depend upon the physics being addressed, but at least one major shell is believed to be necessary to adequately describe low-lying states of a given nucleus. We will use  $N_s$  to denote the number of such states. Thus, for example,  $N_s$  is (12, 20, 32, 44) for either neutrons or protons in the ( $1s0d$ ,  $1p0f$ ,  $2s1dg_{7/2}h_{11/2}$ ,  $2p1fh_{9/2}i_{13/2}$ ) shells.

The totality of Pauli-allowed configurations of the valence nucleons in the single particle states defines the model space in which the many-body Hamiltonian acts. Computing the dimension of this space (number of such many-body states) is a straightforward combinatorial exercise. As noted in the Introduction, the dimension increases strongly with either  $N_s$  or the number of valence nucleons, and can vastly exceed  $10^8$  for realistic applications of current interest. The size of the Hamiltonian matrix to be considered can be reduced somewhat by exploiting rotational and isospin invariance properties. Even so, constructing such a matrix and finding its lowest eigenvalues and eigenstates is difficult in some cases of interest and impossible in most, and thermal properties are completely inaccessible without *ad hoc* assumptions.

The shell model Hamiltonian can be written in the form  $\hat{H} = \hat{H}_1 + \hat{H}_2$  where

$$\hat{H}_1 = \sum_{\alpha} \varepsilon_{\alpha} a_{\alpha}^{\dagger} a_{\alpha} , \quad (2.1a)$$

$$\hat{H}_2 = \frac{1}{2} \sum_{\alpha\beta\gamma\delta} V_{\alpha\beta\gamma\delta} a_{\alpha}^{\dagger} a_{\beta}^{\dagger} a_{\delta} a_{\gamma} . \quad (2.1b)$$

Here,  $a^{\dagger}$  and  $a$  are fermion creation and annihilation operators, and the  $V$  are the uncoupled matrix elements of the two-body interaction. These latter must respect rotational and time-reversal invariance, and parity conservation. To make explicit the rotational invariance and shell structure, we can rewrite the two-body Hamiltonian as

$$\begin{aligned} \hat{H}_2 &= \frac{1}{2} \sum_{abcd} \sum_J V_J(ab, cd) \sum_M \hat{A}_{JM}^{\dagger}(ab) \hat{A}_{JM}(cd) \\ &= \frac{1}{4} \sum_{abcd} \sum_J [(1 + \delta_{ab})(1 + \delta_{cd})]^{1/2} V_J^A(ab, cd) \sum_M \hat{A}_{JM}^{\dagger}(ab) \hat{A}_{JM}(cd) , \end{aligned} \quad (2.2)$$

where the sum is taken over all proton and neutron single-particle orbits (denoted by  $a, b, c, d$ ) and the pair creation and annihilation operators are given by

$$\hat{A}_{JM}^{\dagger}(ab) = \sum_{m_a m_b} (j_a m_a j_b m_b | JM) a_{j_b m_b}^{\dagger} a_{j_a m_a}^{\dagger} = -[a_{j_a}^{\dagger} \times a_{j_b}^{\dagger}]^{JM} , \quad (2.3a)$$

$$\hat{A}_{JM}(ab) = \sum_{m_a m_b} (j_a m_a j_b m_b | JM) a_{j_a m_a} a_{j_b m_b} = [a_{j_a} \times a_{j_b}]^{JM} . \quad (2.3b)$$

The  $V_J(ab, cd)$  are the angular-momentum coupled two-body matrix elements (TBME) of a scalar potential  $V(\vec{r}_1, \vec{r}_2)$  defined as

$$V_J(ab, cd) = \langle [\psi_{j_a}(\vec{r}_1) \times \psi_{j_b}(\vec{r}_2)]^{JM} | V(\vec{r}_1, \vec{r}_2) | [\psi_{j_c}(\vec{r}_1) \times \psi_{j_d}(\vec{r}_2)]^{JM} \rangle , \quad (2.4)$$

(independent of  $M$ ) while the anti-symmetrized two-body matrix elements  $V_J^A(ab, cd)$  are given by

$$V_J^A(ab, cd) = [(1 + \delta_{ab})(1 + \delta_{cd})]^{-1/2} [V_J(ab, cd) - (-1)^{j_c + j_d - J} V_J(ab, dc)] . \quad (2.5)$$

There are a number of methods for deriving the residual interaction  $V$  (which acts in the model space) from the underlying "bare" internucleon interaction [34, 35, 36]. Although a

complete specification of  $V$  requires many two-body matrix elements [37, 38] (e.g., 63 in the complete  $sd$ -shell and 195 in the complete  $pf$ -shell), successful interactions that reproduce a large body of experimental data show a few simple features (e.g., isoscalar pairing, attractive quadrupole, repulsive dipole, ...), with the rest of the TBMEs being small and random [38, 39]. A venerable approximation is to truncate the interaction to just the isoscalar pairing and the quadrupole interaction [40].

Various aspects of the eigenstates of  $\hat{H}$  can be understood through such approximations as Hartree-Fock [41, 42] or Random Phase [43]. However, such approaches are unsuitable for precise work. The preferred method is to expand the wavefunction in a many-body basis (truncated by some criteria, if necessary) and then construct and diagonalize the resulting hamiltonian matrix. Several different approaches to these tasks have been followed over the years. In the *jj-coupling scheme*, developed by the Rochester-Oak Ridge group [17], the antisymmetric  $N$ -particle states in each  $j$ -shell are first built recursively, before the multishell model space is constructed from these single-shell states. The most time-consuming part of this method is the calculation of the single-particle coefficients of fractional parentage to form antisymmetric  $N$ -particle states and it has been found that this scheme has severe limitations when the shell dimensions are large. In the *m-scheme* approach [44, 45] each  $N$ -particle Slater determinant is represented by a computer bit using the binaries 0 and 1 to represent unoccupied and occupied levels. An advantage is that the *m-scheme* reduces the calculation of matrix elements (in second quantization) to very efficient logical operations. However, it becomes impractical when the dimensions involved get very large (i.e., with increasing numbers of particles and/or orbitals). The *OXBASH* code combines *jj*-coupling and *m-scheme* [46, 47] by constructing the basis states in the *m-scheme* approach, but following the *jj*-coupling scheme in the diagonalization of the Hamilton matrix. Recently, the Drexel group has developed an alternative approach based on a pair-truncated fermion model space and permutation group ideas [20]. A more detailed description of the various shell model concepts and codes can be found in [48].

In conventional shell model applications the dimension of the model space makes a complete diagonalization of the Hamiltonian impractical. As one is usually interested only in the nuclear spectrum at low energies, the diagonalization is often performed using the Lanczos algorithm, which is an efficient way to find the few lowest (or highest) eigenvalues and eigenvectors of a large matrix [49, 50].

Physical applications of the shell model were pioneered by Lawson and by Kurath and Cohen in the  $p$ -shell [30, 15]. As the dimensions of the model spaces in the  $sd$ -shell are still not too large, the conventional shell model approaches are well suited and have been quite extensively and successfully applied. In particular, Wildenthal has performed systematic studies of all  $sd$ -shell nuclei and, using a specially designed effective interaction [37], has been able to reproduce energies and transition moments in these nuclei [21]. However, Figure 2.1 illustrates that accurate results can be obtained only in an untruncated basis.

Beyond the  $sd$ -shell, applications of the conventional shell model become more problematic as the large dimensions of the model space make diagonalization impossible. To date, systematic studies of the  $A = 48$  isobars, involving model spaces with about  $10^6$  Slater determinants, have been the limit for the conventional shell model approaches [51]. Nevertheless the successful description of these nuclei underlines again that the shell model concept is also the method of choice in heavier nuclei – if such applications were only possible. As noted by

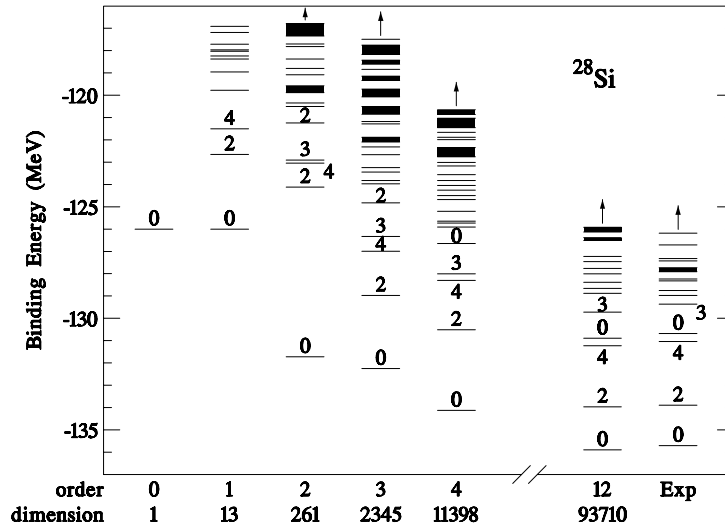


FIG 2.1 Convergence of the spectrum of  $^{28}\text{Si}$  with increasing dimension of the model space; “order 12” corresponds to the complete  $sd$ -shell space [21].

Caurier *et al.* [51], it took two generations of hardware and software development to extend shell model calculations from  $A = 44$  to  $A = 48$ . Thus, conventional shell model calculations for nuclei heavier than  $A = 50$  appear out of reach in the near future, even assuming an optimistic increase of computer capabilities.

Facing the impracticality of complete shell model calculations, Poves, Zuker, and collaborators [52] have used a truncation method for the shell model in the  $1p0f$  space. When applied to observables like the ground state energy or Gamow-Teller strength, the convergence appears fast enough to obtain reasonable approximations to the (complete) shell model results after a few truncation scheme iterations. As an example, Fig. 2.2 shows the Gamow-Teller strengths in  $^{54}\text{Fe}$  and  $^{56}\text{Fe}$  calculated at various levels of truncation; there is clear convergence to the complete result obtained with the SMMC methods (see Section 8).

### 3 Overview of Monte Carlo Methods

In this section, we give an overview of SMMC methods. In particular, we describe what the methods are (and are not) capable of calculating. We then discuss the essence of the HS transformation, which is at the heart of the calculations.

The SMMC methods rely on an ability to deal with the imaginary-time many-body evolution operator,  $\exp(-\beta\hat{H})$ , where  $\beta$  is a real  $c$ -number. While this does not result in a complete solution to the many-body problem in the sense of giving all eigenvalues and eigenstates of  $\hat{H}$ , it can result in much useful information. For example, the expectation value of some observable  $\hat{\Omega}$  in the grand canonical ensemble can be obtained by adding to  $\hat{H}$  a term  $-\mu_n\hat{N} - \mu_p\hat{Z}$ , ( $\mu_n$  and  $\mu_p$  are the neutron and proton chemical potentials) and then calculating

$$\langle\hat{\Omega}\rangle = \frac{\text{Tr} e^{-\beta\hat{H}}\hat{\Omega}}{\text{Tr} e^{-\beta\hat{H}}}. \quad (3.1)$$

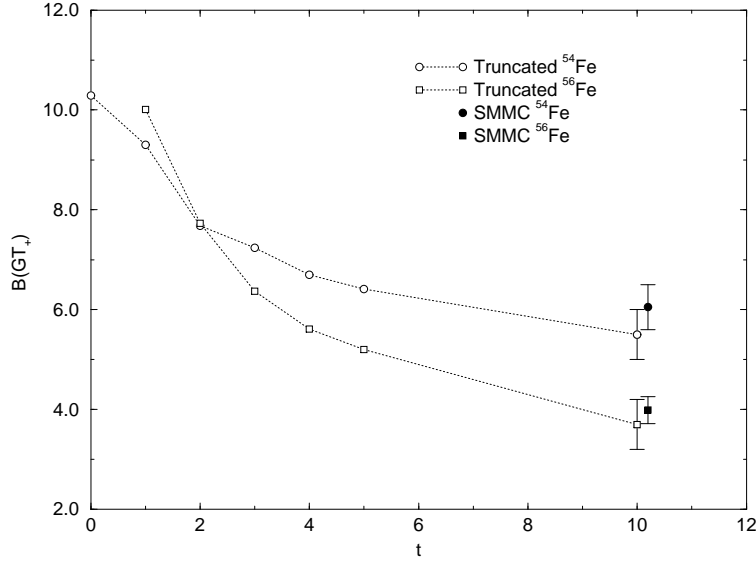


FIG 2.2 Comparison of the total Gamow-Teller strengths  $B(\text{GT}_+)$  for  $^{54,56}\text{Fe}$  in a series of direct diagonalizations with decreasing level of truncation [52] with the complete results obtained with the SMMC method (solid symbols at  $t = 10$ ) [55]. The open symbols at  $t = 10$  show the extrapolated no-truncation results of [52].

Here,  $\beta \equiv T^{-1}$  is interpreted as the inverse of the temperature  $T$ , and the many-body trace is defined as

$$\text{Tr } \hat{X} \equiv \sum_i \langle i | \hat{X} | i \rangle, \quad (3.2)$$

where the sum is over *all* many-body states of the system. Similarly, if  $\hat{P}_A = \delta(A - \hat{N})$  is the projector onto states with  $A$  nucleons (actually the product of separate neutron and proton projectors), the canonical ensemble is defined by

$$\text{Tr}_A \hat{X} \equiv \sum_i \langle i | \hat{P}_A \hat{X} | i \rangle, \quad (3.3)$$

and the associated expectation value is

$$\langle \hat{\Omega} \rangle_A = \frac{\text{Tr}_A e^{-\beta \hat{H}} \hat{\Omega}}{\text{Tr}_A e^{-\beta \hat{H}}}. \quad (3.4)$$

In the limit of low temperature ( $T \rightarrow 0$  or  $\beta \rightarrow \infty$ ), both the grand-canonical and canonical traces reduce to ground state expectation values. Alternatively, if  $|\Phi\rangle$  is a many-body trial state not orthogonal to the exact ground state,  $|\Psi\rangle$ , then  $e^{-\beta \hat{H}}$  can be used as a filter to refine  $|\Phi\rangle$  to  $|\Psi\rangle$  as  $\beta$  becomes large. An observable can be calculated in this “zero temperature” method as

$$\frac{\langle \Phi | e^{-\frac{\beta}{2} \hat{H}} \hat{\Omega} e^{-\frac{\beta}{2} \hat{H}} | \Phi \rangle}{\langle \Phi | e^{-\beta \hat{H}} | \Phi \rangle} \xrightarrow{\beta \rightarrow \infty} \frac{\langle \Psi | \hat{\Omega} | \Psi \rangle}{\langle \Psi | \Psi \rangle}. \quad (3.5)$$

If  $\hat{\Omega}$  is the hamiltonian, then (3.5) at  $\beta = 0$  is the variational estimate of the energy, and improves as  $\beta$  increases. Of course, the efficiency of the refinement for any observable depends upon the degree to which  $|\Phi\rangle$  approximates  $|\Psi\rangle$ .

Beyond such static properties,  $e^{-\beta\hat{H}}$  allows us to obtain some information about the dynamical response of the system. For operators  $\hat{\Omega}^\dagger$  and  $\hat{\Omega}$ , the response function  $R_\Omega(\tau)$  in the canonical ensemble is defined as

$$R_\Omega(\tau) \equiv \frac{\text{Tr}_A e^{-(\beta-\tau)\hat{H}} \hat{\Omega}^\dagger e^{-\tau\hat{H}} \hat{\Omega}}{\text{Tr}_A e^{-\beta\hat{H}}} \equiv \langle \hat{\Omega}^\dagger(\tau) \hat{\Omega}(0) \rangle_A, \quad (3.6)$$

where  $\hat{\Omega}^\dagger(\tau) \equiv e^{\tau\hat{H}} \hat{\Omega}^\dagger e^{-\tau\hat{H}}$  is the imaginary-time Heisenberg operator. As we shall see in section 8 below, interesting choices for  $\hat{\Omega}$  are the  $a_j$  for particular orbitals, the Gamow-Teller,  $M1$ , or quadrupole moment, etc. Inserting complete sets of  $A$ -body eigenstates of  $\hat{H}$  ( $\{|i\rangle, |f\rangle\}$  with energies  $E_{i,f}$ ) shows that

$$R_\Omega(\tau) = \frac{1}{Z} \sum_{if} e^{-\beta E_i} |\langle f | \hat{\Omega} | i \rangle|^2 e^{-\tau(E_f - E_i)}, \quad (3.7)$$

where  $Z = \sum_i e^{-\beta E_i}$  is the partition function. Thus,  $R_\Omega(\tau)$  is the Laplace transform of the strength function  $S_\Omega(E)$ :

$$R_\Omega(\tau) = \int_{-\infty}^{\infty} e^{-\tau E} S_\Omega(E) dE; \quad (3.8a)$$

$$S_\Omega(E) = \frac{1}{Z} \sum_{fi} e^{-\beta E_i} |\langle f | \hat{\Omega} | i \rangle|^2 \delta(E - E_f + E_i). \quad (3.8b)$$

Hence, if we can calculate  $R_\Omega(\tau)$ ,  $S_\Omega(E)$  can be determined. Short of a full inversion of the Laplace transform (which is often numerically difficult; see section 6.4 below), the behavior of  $R_\Omega(\tau)$  for small  $\tau$  gives information about the energy-weighted moments of  $S_\Omega$ . In particular,

$$R_\Omega(0) = \int_{-\infty}^{\infty} S_\Omega(E) dE = \frac{1}{Z} \sum_i e^{-\beta E_i} |\langle f | \hat{\Omega} | i \rangle|^2 = \langle \hat{\Omega}^\dagger \hat{\Omega} \rangle_A \quad (3.9)$$

is the total strength,

$$-R'_\Omega(0) = \int_{-\infty}^{\infty} S_\Omega(E) E dE = \frac{1}{Z} \sum_{if} e^{-\beta E_i} |\langle f | \hat{\Omega} | i \rangle|^2 (E_f - E_i) \quad (3.10)$$

is the first moment,

$$R''_\Omega(0) = \int_{-\infty}^{\infty} S_\Omega(E) E^2 dE = \frac{1}{Z} \sum_{if} e^{-\beta E_i} |\langle f | \hat{\Omega} | i \rangle|^2 (E_f - E_i)^2 \quad (3.11)$$

is the second moment, and so on. (In these expressions, the prime denotes differentiation with respect to  $\tau$ .)

It is important to note that we cannot usually obtain detailed spectroscopic information from SMMC calculations. Rather, we can calculate expectation values of operators in the

thermodynamic ensembles or the ground state. Occasionally, these can indirectly furnish properties of excited states. For example, if there is a collective  $2^+$  state absorbing most of the  $E2$  strength, then the centroid of the quadrupole response function will be a good estimate of its energy. But, in general, we are without the numerous specific excitation energies and wavefunctions that characterize a direct diagonalization. This is both a blessing and a curse. The former is that for the very large model spaces of interest, there is no way in which we can deal explicitly with all of the wavefunctions and excitation energies. Indeed, we often don't need to, as experiments only measure average nuclear properties at a given excitation energy. The curse is that comparison with detailed properties of specific levels is difficult. In this sense, the SMMC method is complementary to direct diagonalization for modest model spaces, but is the only method for treating very large problems.

It remains, of course, to describe the Hubbard-Stratanovich "trick" by which  $e^{-\beta\hat{H}}$  is managed. In broad terms, the difficult many-body evolution is replaced by a superposition of an infinity of tractable one-body evolutions, each in a different external field,  $\sigma$ . Integration over the external fields thus reduces the many-body problem to quadrature. The following schematic discussion serves to illustrate the central idea; important details will be added in the following sections.

With some rearrangement, as discussed in Section 4, the many-body Hamiltonian (2.1) can be written schematically as

$$\hat{H} = \varepsilon\hat{O} + \frac{1}{2}V\hat{O}\hat{O}, \quad (3.12)$$

where  $\hat{O}$  is a density operator of the form  $a^\dagger a$ ,  $V$  is the strength of the two-body interaction, and  $\varepsilon$  a single-particle energy. In the full problem, there are many such quantities with various orbital indices that are summed over, but we omit them here for the sake of clarity.

All of the difficulty arises from the two-body interaction, that term in  $\hat{H}$  quadratic in  $\hat{O}$ . If  $\hat{H}$  were solely linear in  $\hat{O}$ , we would have a one-body quantum system, which is readily dealt with (see the Appendix). To linearize the evolution, we employ the Gaussian identity

$$e^{-\beta\hat{H}} = \sqrt{\frac{\beta|V|}{2\pi}} \int_{-\infty}^{\infty} d\sigma e^{-\frac{1}{2}\beta|V|\sigma^2} e^{-\beta\hat{h}}; \quad \hat{h} = \varepsilon\hat{O} + sV\sigma\hat{O}. \quad (3.13)$$

Here,  $\hat{h}$  is a one-body operator associated with a  $c$ -number field  $\sigma$ , and the many-body evolution is obtained by integrating the one-body evolution  $\hat{U}_\sigma \equiv e^{-\beta\hat{h}}$  over all  $\sigma$  with a Gaussian weight. The phase,  $s$ , is 1 if  $V < 0$  or  $i$  if  $V > 0$ . Equation (3.13) is easily verified by completing the square in the exponent of the integrand and then doing the integral; since there is only a single operator  $\hat{O}$ , there is no need to worry about non-commutation.

With an expression of the form (3.13), it is now straightforward to write observables as the ratio of two integrals. For example, the canonical expectation value (3.4) becomes

$$\langle \hat{\Omega} \rangle_A = \frac{\int d\sigma e^{-\frac{\beta}{2}|V|\sigma^2} \text{Tr}_A \hat{U}_\sigma \hat{\Omega}}{\int d\sigma e^{-\frac{\beta}{2}|V|\sigma^2} \text{Tr}_A \hat{U}_\sigma}, \quad (3.14)$$

which can be more conveniently written as

$$\langle \hat{\Omega} \rangle_A = \frac{\int d\sigma W_\sigma \Omega_\sigma}{\int d\sigma W_\sigma}; \quad (3.15a)$$

$$W_\sigma = G_\sigma \text{Tr}_A \hat{U}_\sigma; \quad G_\sigma = e^{-\frac{\beta}{2}|V|\sigma^2}, \quad \Omega_\sigma = \frac{\text{Tr}_A \hat{U}_\sigma \hat{\Omega}}{\text{Tr}_A \hat{U}_\sigma} \quad (3.15b)$$

Thus, the many-body observable is the weighted average (weight  $W_\sigma$ ) of the observable  $\Omega_\sigma$  calculated in a canonical ensemble involving only the one-body evolution  $\hat{U}_\sigma$ . Similar expressions involving two  $\sigma$  fields (one each for  $e^{-\tau\hat{H}}$  and  $e^{-(\beta-\tau)\hat{H}}$ ) can be written down for the response function (3.6) and all are readily transcribed to the grand-canonical ensemble (3.1) or zero-temperature case (3.5).

An expression of the form (3.15) has a number of attractive features. First, the problem has been reduced to quadrature—we need only calculate the ratio of two integrals. Second, all of the quantum mechanics (which appears in  $\Omega_\sigma$ ) is of the one-body variety, which is simply handled by the algebra of  $N_s \times N_s$  matrices. The price to pay is that we must treat the one-body problem for all possible  $\sigma$  fields.

For a realistic hamiltonian, there will be many non-commuting density operators  $\hat{O}_\alpha$  present, but we will always be able to reduce the two-body term to diagonal form. Thus for a general two-body interaction in a general time-reversal invariant form we write

$$\hat{H} = \sum_\alpha (\epsilon_\alpha^* \hat{O}_\alpha + \epsilon_\alpha \hat{O}_\alpha) + \frac{1}{2} \sum_\alpha V_\alpha \{ \hat{O}_\alpha, \hat{O}_\alpha \}, \quad (3.16)$$

where  $\hat{O}_\alpha$  is the time reverse of  $\hat{O}_\alpha$ . Since in general,  $[\hat{O}_\alpha, \hat{O}_\beta] \neq 0$  we must split the interval  $\beta$  into  $N_t$  “time slices” of length  $\Delta\beta \equiv \beta/N_t$ ,

$$e^{-\beta\hat{H}} = [e^{-\Delta\beta\hat{H}}]^{N_t}, \quad (3.17)$$

and for each time slice  $n = 1, \dots, N_t$  perform a linearization similar to (3.16) using auxiliary fields  $\sigma_{\alpha n}$ :

$$e^{-\Delta\beta\hat{H}} \approx \int_{-\infty}^{\infty} \prod_n \left( \frac{d\sigma_{\alpha n} d\sigma_{\alpha n}^* \Delta\beta |V_\alpha|}{2\pi} \right) e^{-\Delta\beta \sum_\alpha |V_\alpha| |\sigma_{\alpha n}|^2} e^{-\Delta\beta \hat{h}_n};$$

$$\hat{h}_n = \sum_\alpha (\epsilon_\alpha^* + s_\alpha V_\alpha \sigma_{\alpha n}) \hat{O}_\alpha + (\epsilon_\alpha + s_\alpha V_\alpha \sigma_{\alpha n}^*) \hat{O}_\alpha. \quad (3.18)$$

Note that because the various  $\hat{O}_\alpha$  need not commute, (3.18) is accurate only through order  $\Delta\beta$  and that the representation of  $e^{-\Delta\beta\hat{h}}$  must be accurate through order  $\Delta\beta^2$  to achieve that accuracy.

Upon composing (3.18) many times according to (3.17), we can write expressions for observables as the ratio of two field integrals. For example, (3.15) becomes

$$\langle \hat{\Omega} \rangle_A = \frac{\int \mathcal{D}\sigma W_\sigma \Omega_\sigma}{\int \mathcal{D}\sigma W_\sigma}, \quad (3.19a)$$

where

$$W_\sigma = G_\sigma \text{Tr}_A \hat{U}; \quad G_\sigma = e^{-\Delta\beta \sum_{\alpha n} |V_\alpha| |\sigma_{\alpha n}|^2};$$

$$\Omega_\sigma = \frac{\text{Tr}_A \hat{U} \hat{\Omega}}{\text{Tr}_A \hat{U}}; \quad \mathcal{D}\sigma \equiv \prod_{n=1}^{N_t} \prod_\alpha d\sigma_{\alpha n} d\sigma_{\alpha n}^* \left( \frac{\Delta\beta |V_\alpha|}{2\pi} \right), \quad (3.19b)$$

and

$$\begin{aligned}\hat{U} &= \hat{U}_{N_t} \dots \hat{U}_2 \hat{U}_1 ; & \hat{U}_n &= e^{-\Delta\beta \hat{h}_n}; \\ \hat{h}_n &= \sum_{\alpha} (\varepsilon_{\alpha}^* + s_{\alpha} V_{\alpha} \sigma_{\alpha n}) \hat{\mathcal{O}}_{\alpha} + (\varepsilon_{\alpha} + s_{\alpha} V_{\alpha} \sigma_{\alpha n}^*) \hat{\mathcal{O}}_{\alpha} .\end{aligned}\tag{3.19c}$$

This is, of course, a discrete version of a path integral over  $\sigma$ . Because there is a field variable for each operator at each time slice, the dimension of the integrals  $\mathcal{D}\sigma$  can be very large, often exceeding  $10^5$ . Note that because of the errors in (3.18), the errors in Eqs. (3.19) are of order  $\Delta\beta$ , so that high accuracy requires large  $N_t$  and perhaps extrapolation to  $N_t = \infty$  ( $\Delta\beta = 0$ ).

Two steps are then necessary to implement a SMMC calculation. First, we must learn how to write expressions like (3.16, 3.19) for a realistic hamiltonian. Second, we must learn how to efficiently compute the resulting ratio of high-dimensional integrals. These tasks are, respectively, the subjects of the following two sections.

## 4 Decomposition of the Hamiltonian

To realize the HS transformation, the two-body parts of  $\hat{H}$  must be cast as a quadratic form in one-body density operators  $\hat{\mathcal{O}}_{\alpha}$ . As discussed in Ref. [27], there is considerable freedom in doing so. In the simplest example, let us consider an individual interaction term,

$$\hat{H} = a_1^{\dagger} a_2^{\dagger} a_4 a_3 ,\tag{4.1}$$

where  $a_i^{\dagger}, a_i$  are anti-commuting fermion creation and annihilation operators.

There are then two ways to proceed: we can group (1, 3) and (2, 4) to get

$$\hat{H} = \overbrace{a_1^{\dagger} a_3} a_2^{\dagger} a_4 - a_1^{\dagger} a_4 \delta_{23}\tag{4.2a}$$

$$= -a_1^{\dagger} a_4 \delta_{23} + \frac{1}{2} [a_1^{\dagger} a_3, a_2^{\dagger} a_4] + \frac{1}{4} (a_1^{\dagger} a_3 + a_2^{\dagger} a_4)^2 - \frac{1}{4} (a_1^{\dagger} a_3 - a_2^{\dagger} a_4)^2 ,\tag{4.2b}$$

or group (1, 4) and (2, 3) to get

$$\hat{H} = -\overbrace{a_1^{\dagger} a_4} a_2^{\dagger} a_3 + a_1^{\dagger} a_3 \delta_{24}\tag{4.3a}$$

$$= a_1^{\dagger} a_3 \delta_{24} - \frac{1}{2} [a_1^{\dagger} a_4, a_2^{\dagger} a_3] - \frac{1}{4} (a_1^{\dagger} a_4 + a_2^{\dagger} a_3)^2 + \frac{1}{4} (a_1^{\dagger} a_4 - a_2^{\dagger} a_3)^2 .\tag{4.3b}$$

The commutator terms in both (4.2b, 4.3b) are one-body operators, but now the quadratic forms are squares of density operators. We refer to Eq. (4.2b) as the ‘direct’ decomposition and Eq. (4.3b) as the ‘exchange’ decomposition. At the formal level, it is also possible to consider a pairing decomposition [27], although no practical calculations have been done with that scheme.

For any general two-body Hamiltonian, there is the freedom to choose between the direct and exchange formulations and it is particularly convenient to use quadratic forms of density operators that respect rotational invariance, isospin symmetry, parity conservation, and the

shell structure of the system. Although the exact path integral result is independent of the scheme used, different schemes will lead to different results under certain approximations (e.g., mean field or static path approximation [56]). The choice of decomposition will also affect the rate of convergence of numerical results as  $N_t \rightarrow \infty$ , as well as the statistical precision of the Monte Carlo evaluation.

We note that the two-body Hamiltonian for fermion systems is completely specified by the set of anti-symmetrized two-body matrix elements  $V_J^A(ab, cd)$  of Eq. (2.5) that are the input to many standard shell model codes such as OXBASH [46]. Indeed, we can add to the  $V_J^A(ab, cd)$  any set of (unphysical) symmetric two-body matrix elements  $V_J^S(ab, cd)$  satisfying

$$V_J^S(ab, cd) = (-1)^{j_c + j_d - J} V_J^S(ab, dc) , \quad (4.4)$$

without altering the action of  $\hat{H}_2$  on any many-fermion wave function. However, note that although the  $V_J^S(ab, cd)$  do not alter the eigenstates and eigenvalues of the full Hamiltonian, they can (and do) affect the character of the decomposition of  $\hat{H}_2$ , as is shown below. In what follows, we define the set of two-body matrix elements  $V_J^N(ab, cd)$  that may have no definite symmetries as

$$V_J^N(ab, cd) = V_J^A(ab, cd) + V_J^S(ab, cd) , \quad (4.5)$$

allowing us to write the two-body Hamiltonian (2.2) as

$$\hat{H}_2 = \frac{1}{4} \sum_{abcd} \sum_J [(1 + \delta_{ab})(1 + \delta_{cd})]^{1/2} V_J^N(ab, cd) \sum_M \hat{A}_{JM}^\dagger(ab) \hat{A}_{JM}(cd) . \quad (4.6)$$

To decompose  $\hat{H}_2$ , we perform a Pandya transformation to recouple  $(a, c)$  and  $(b, d)$  into density operators with definite multipolarity,

$$\hat{\rho}_{KM}(ab) = \sum_{m_a, m_b} (j_a m_a j_b m_b | KM) a_{j_a m_a}^\dagger \tilde{a}_{j_b m_b} , \quad (4.7)$$

where  $\tilde{a}_{j_a m_a} = (-1)^{j_a + m_a} a_{j_a - m_a}$ . Then  $\hat{H}_2$  can be rewritten as

$$\hat{H}_2 = \hat{H}'_2 + \hat{H}'_1 ; \quad (4.8)$$

$$\hat{H}'_2 = \frac{1}{2} \sum_{abcd} \sum_K E_K(ac, bd) \sum_M (-1)^M \hat{\rho}_{K-M}(ac) \hat{\rho}_{KM}(bd) , \quad (4.9)$$

where the particle-hole matrix elements of the interaction are

$$E_K(ac, bd) = (-1)^{j_b + j_c} \sum_J (-1)^J (2J + 1) \left\{ \begin{array}{ccc} j_a & j_b & J \\ j_d & j_c & K \end{array} \right\} \\ \times \frac{1}{2} V_J^N(ab, cd) \sqrt{(1 + \delta_{ab})(1 + \delta_{cd})} , \quad (4.10)$$

and  $\hat{H}'_1$  is a one-body operator given by

$$\hat{H}'_1 = \sum_{ad} \epsilon'_{ad} \hat{\rho}_{00}(a, d) , \quad (4.11)$$

with

$$\epsilon'_{ad} = -\frac{1}{4} \sum_b \sum_J (-1)^{J+j_a+j_b} (2J+1) \frac{1}{\sqrt{2j_a+1}} V_J^N(ab, bd) \sqrt{(1+\delta_{ab})(1+\delta_{cd})}. \quad (4.12)$$

Note that adding symmetric matrix elements is equivalent to using the exchange decomposition for some parts of the interaction. The freedom in choosing the combinations of direct and exchange decomposition is then embodied in the arbitrary symmetric part of the matrix elements  $V_J^N$ .

Introducing the shorthand notation  $i = (ac), j = (bd)$ , we can write Eq. (4.9) as

$$\hat{H}'_2 = \frac{1}{2} \sum_{ij} \sum_K E_K(i, j) (-1)^M \hat{\rho}_{KM}(i) \hat{\rho}_{K-M}(j). \quad (4.13)$$

Upon diagonalizing the matrix  $E_K(i, j)$  to obtain eigenvalues  $\lambda_{K\alpha}$  and associated eigenvectors  $v_{K\alpha}$ , we can represent  $\hat{H}'_2$  as

$$\hat{H}'_2 = \frac{1}{2} \sum_{K\alpha} \lambda_K(\alpha) (-1)^M \hat{\rho}_{KM}(\alpha) \hat{\rho}_{K-M}(\alpha), \quad (4.14)$$

where

$$\hat{\rho}_{KM}(\alpha) = \sum_i \hat{\rho}_{KM}(i) v_{K\alpha}(i). \quad (4.15)$$

Finally, if we define

$$\hat{Q}_{KM}(\alpha) \equiv \frac{1}{\sqrt{2(1+\delta_{M0})}} \left( \hat{\rho}_{KM}(\alpha) + (-1)^M \hat{\rho}_{K-M}(\alpha) \right), \quad (4.16a)$$

$$\hat{P}_{KM}(\alpha) \equiv -\frac{i}{\sqrt{2(1+\delta_{M0})}} \left( \hat{\rho}_{KM}(\alpha) - (-1)^M \hat{\rho}_{K-M}(\alpha) \right), \quad (4.16b)$$

then  $\hat{H}'_2$  becomes

$$\hat{H}'_2 = \frac{1}{2} \sum_{K\alpha} \lambda_K(\alpha) \sum_{M \geq 0} \left( \hat{Q}_{KM}^2(\alpha) + \hat{P}_{KM}^2(\alpha) \right). \quad (4.17)$$

This completes the representation of the two-body interaction as a diagonal quadratic form in density operators. We then couple auxiliary fields  $\sigma_{KM}(\alpha)$  to  $\hat{Q}_{KM}$  and  $\tau_{KM}(\alpha)$  to  $\hat{P}_{KM}$  in the HS transformation. (The latter are not to be confused with the ‘‘imaginary time’’  $\tau$ .)

In the treatment thus far, protons and neutrons were not distinguished from each other. Although the original Hamiltonian  $\hat{H}_2$  conserves proton and neutron numbers, we ultimately might deal with one-body operators  $\rho_{KM}(a_p, b_n)$  and  $\rho_{KM}(a_n, b_p)$  ( $n, p$  subscripts denoting neutron and proton) that individually do not do so. The one-body hamiltonian  $\hat{h}_\sigma$  appearing in the HS transformation then mixes neutrons and protons. The single-particle wavefunctions in a Slater determinant then contain both neutron and proton components and neutron and proton numbers are not conserved separately in each Monte Carlo sample; rather the conservation is enforced only statistically.

It is, of course, possible to recouple so that only density operators separately conserving neutron and proton numbers ( $\hat{\rho}_{KM}(a_p, b_p)$  and  $\hat{\rho}_{KM}(a_n, b_n)$ ) are present. To do so, we write the two-body Hamiltonian in a manifestly isospin-invariant form,

$$\hat{H}_2 = \frac{1}{4} \sum_{abcd} \sum_{JT} [(1 + \delta_{ab})(1 + \delta_{cd})]^{1/2} V_{JT}^N(ab, cd) \sum_{MT_z} \hat{A}_{JT;MT_z}^\dagger(ab) \hat{A}_{JT;MT_z}(cd) , \quad (4.18)$$

where, similar to the previous definition (4.6), the pair operator is

$$\hat{A}_{JT;MT_z}^\dagger(ab) = \sum_{m_a, m_b} (j_a m_a j_b m_b | JM) \left( \frac{1}{2} t_a \frac{1}{2} t_b | TT_z \right) a_{j_b m_b t_b}^\dagger a_{j_a m_a t_a}^\dagger . \quad (4.19)$$

Here  $(\frac{1}{2}, t_a)$ , etc. are the isospin indices with  $t_a = -\frac{1}{2}$  for proton states and  $t_a = \frac{1}{2}$  for neutron states, and  $(TT_z)$  are the coupled isospin quantum numbers. The two-body Hamiltonian can now be written solely in terms of density operators that conserve the proton and neutron numbers. Namely,

$$\hat{H}_2 = \hat{H}'_1 + \hat{H}'_2 , \quad (4.20)$$

where

$$\hat{H}'_1 = \sum_{ad} \sum_{t=p,n} \epsilon'_{ad} \rho_{00t}(a, d) , \quad (4.21)$$

with

$$\epsilon'_{ad} = -\frac{1}{4} \sum_b \sum_J (-1)^{J+j_a+j_b} (2J+1) \frac{1}{\sqrt{2j_a+1}} V_{JT=1}^N(ab, bd) \sqrt{(1+\delta_{ab})(1+\delta_{cd})} , \quad (4.22)$$

and

$$\hat{H}'_2 = \frac{1}{2} \sum_{abcd} \sum_{K,T=0,1} E_{KT}(ac, bd) [\hat{\rho}_{KT}(i) \times \hat{\rho}_{KT}(j)]^{J=0} . \quad (4.23)$$

Here, we define  $\hat{\rho}_{KMT}$  as

$$\hat{\rho}_{KMT} = \hat{\rho}_{KMp} + (-1)^T \hat{\rho}_{KMn} , \quad (4.24)$$

and the  $E_{KT}$  are given by

$$\begin{aligned} E_{KT=0}(ac, bd) &= (-1)^{j_b+j_c} \sum_J (-1)^J (2J+1) \left\{ \begin{matrix} j_a & j_b & J \\ j_d & j_c & K \end{matrix} \right\} \sqrt{(1+\delta_{ab})(1+\delta_{cd})} \\ &\times \frac{1}{2} \left[ V_{JT=1}^N(ab, cd) + \frac{1}{2} (V_{JT=0}^A(ab, cd) - V_{JT=1}^S(ab, cd)) \right] , \end{aligned} \quad (4.25)$$

$$\begin{aligned} E_{KT=1}(ac, bd) &= -(-1)^{j_b+j_c} \sum_J (-1)^J (2J+1) \left\{ \begin{matrix} j_a & j_b & J \\ j_d & j_c & K \end{matrix} \right\} \sqrt{(1+\delta_{ab})(1+\delta_{cd})} \\ &\times \frac{1}{4} \left( V_{JT=0}^A(ab, cd) - V_{JT=1}^S(ab, cd) \right) . \end{aligned} \quad (4.26)$$

In this isospin formalism, since  $\hat{A}_{JT;MT_z}(ab) = (-1)^{j_a+j_b-J+T} \hat{A}_{JT;MT_z}(ba)$ , the definitions of the symmetric and antisymmetric parts of  $V_{JT}^N(ab, cd)$ ,  $V_{JT}^S(ab, cd)$ , and  $V_{JT}^A(ab, cd)$  become

$$V_{JT}^{S/A}(ab, cd) \equiv \frac{1}{2} \left[ V_{JT}^N(ab, cd) \pm (-1)^{J+j_a+j_b+T-1} V_{JT}^N(ba, cd) \right] . \quad (4.27)$$

Note that these expressions allow less freedom in manipulating the decomposition since we have to couple proton with proton and neutron with neutron in forming the density operators. Also note that  $E_{KT=0}(ac, bd) - E_{KT=1}(ac, bd)$  is an invariant related only to the physical part of the interactions,  $(V_{JT=1}^A + V_{JT=0}^A)$ . We can choose all  $E_{KT=1}$  to be zero in the above (by setting  $V_{JT=1}^S = V_{JT=0}^A$ ) leaving  $E_{KT=0}$  completely determined by the physical matrix elements. In that case, we can halve the number of fields to be integrated.

If we now diagonalize the  $E_{KT}(i, j)$  as before and form the operators

$$\hat{Q}_{KMT}(\alpha) \equiv \frac{1}{\sqrt{2(1+\delta_{M0})}}(\hat{\rho}_{KMT}(\alpha) + (-1)^M \hat{\rho}_{K-MT}(\alpha)), \quad (4.28a)$$

$$\hat{P}_{KMT}(\alpha) \equiv -\frac{i}{\sqrt{2(1+\delta_{M0})}}(\hat{\rho}_{KMT}(\alpha) - (-1)^M \hat{\rho}_{K-MT}(\alpha)), \quad (4.28b)$$

the two-body part of the Hamiltonian can finally be written as

$$\hat{H}'_2 = \frac{1}{2} \sum_{KT} \sum_{\alpha} \lambda_{KT}(\alpha) \sum_{M \geq 0} (\hat{Q}_{KMT}^2(\alpha) + \hat{P}_{KMT}^2(\alpha)). \quad (4.29)$$

In this decomposition, the one-body hamiltonian  $\hat{h}$  of the HS transformation does not mix protons and neutrons. We can then represent the proton and neutron wavefunctions by separate determinants, and the number of neutrons and protons will be conserved rigorously during each Monte Carlo sample. For general interactions, even if we choose nonzero  $E_{KT=1}$  matrix elements, the number of fields involved is half that for a decomposition that mixes neutrons and protons, and the matrix dimension is also halved. These two factors combine to speed up the computation significantly. In this sense, an isospin formalism is more favorable, although at the cost of limiting the degrees of freedom embodied in the symmetric matrix elements  $V_J^S$ .

## 5 Monte Carlo quadrature

The manipulations of the previous sections have reduced the shell model to quadrature. That is, thermodynamic expectation values are given as the ratio of two multidimensional integrals over the auxiliary fields. The dimension  $D$  of these integrals is of order  $N_s^2 N_t$ , which can exceed  $10^5$  for the problems of interest. Monte Carlo methods are the only practical means of evaluating such integrals. In this section, we review those aspects of Monte Carlo quadrature relevant to the task at hand. Our discussion is adapted from that of Ref. [50], where a more general exposition can be found.

Monte Carlo quadrature can be a very efficient way of evaluating integrals of high dimension. The name ‘‘Monte Carlo’’ arises from the random or ‘‘chance’’ character of the method and the famous casino in Monaco. The essential idea is not to evaluate the integrand at every one of a large number of quadrature points, but rather at only a representative random sampling of fields. This is analogous to predicting the results of an election on the basis of a poll of a small number of voters.

To apply Monte Carlo quadrature to the shell model (i.e., expressions such as (3.19)), the weight function  $W_{\sigma}$  must be real and non-negative. While the properties of  $W$  clearly

depend upon the interaction and decomposition used, these conditions are not satisfied for the natural decompositions of most realistic hamiltonians. However, a broad class of schematic interactions and all realistic interactions satisfy these conditions closely enough (or, occasionally, exactly) so that Monte Carlo quadrature can be used. Thus, for the purposes of the present discussion, we assume  $W_\sigma \geq 0$  and postpone a discussion of the so-called “sign problem” to section 7 below.

To understand the Monte Carlo method, we recast the ratio of integrals in Eq. (3.19) as

$$\langle \hat{\Omega} \rangle = \int d^D \sigma P_\sigma \Omega_\sigma, \quad (5.1)$$

where

$$P_\sigma = \frac{W_\sigma}{\int d^D \sigma W_\sigma}. \quad (5.2)$$

Since  $\int d^D \sigma P_\sigma = 1$  and  $P_\sigma \geq 0$ , we can think of  $P_\sigma$  as a probability density and  $\langle \hat{\Omega} \rangle$  as the average of  $\Omega_\sigma$  weighted by  $P_\sigma$ . Thus, if  $\{\sigma_s, s = 1, \dots, S\}$  are a set of  $S$  field configurations randomly chosen with probability density  $P_\sigma$ , we can approximate  $\langle \hat{\Omega} \rangle$  as

$$\langle \hat{\Omega} \rangle \approx \frac{1}{S} \sum_{s=1}^S \Omega_s, \quad (5.3)$$

where  $\Omega_s$  is the value of  $\Omega_\sigma$  at the field configuration  $\sigma_s$ . Since this estimate of  $\langle \hat{\Omega} \rangle$  depends upon the randomly chosen field configurations, it too will be a random variable whose average value is the required integral. To quantify the uncertainty of this estimate, we consider each of the  $\Omega_s$  as a random variable and invoke the central limit theorem to obtain

$$\sigma_{\langle \hat{\Omega} \rangle}^2 = \frac{1}{S} \int d^D \sigma P_\sigma (\Omega_\sigma - \langle \hat{\Omega} \rangle)^2 \approx \frac{1}{S^2} \sum_{s=1}^S (\Omega_s - \langle \hat{\Omega} \rangle)^2. \quad (5.4)$$

Equation (5.4) reveals two very important aspects of Monte Carlo quadrature. First, the uncertainty in the estimate of the integral decreases as  $S^{-1/2}$ . Hence, if more samples are used, we will get a more precise answer, although the error decreases very slowly with the number of samples (a factor of four more numerical work is required to halve the uncertainty). The second important point to realize from (5.4) is that the precision of the result depends upon the extent to which  $\Omega_\sigma$  deviates from its average value over the region of integration; the best case is when  $\Omega_\sigma$  is as smooth as possible.

The discussion above shows that Monte Carlo quadrature involves two basic operations: generating field configurations randomly distributed according to the specified distribution  $P_\sigma$  (or, equivalently,  $W_\sigma$ , to which it is proportional) and then evaluating the observable  $\Omega_\sigma$  for these fields. The second operation is straightforward (details are discussed in the following section and the appendix), but it is less obvious how to generate the required field configurations.

When the probability distribution has a simple analytical form, there are a number of methods that can be invoked to generate independent random samples [57]. However, in the present case  $P_\sigma$  has a complicated dependence upon the auxiliary fields that is not amenable to these methods. Rather, we employ the Metropolis, Rosenbluth, Rosenbluth, Teller, and

Teller algorithm [58], which requires only the ability to calculate the weight function for a given value of the integration variables.

Although the algorithm of Metropolis *et al.* can be implemented in a variety of ways, we begin by describing one simple realization. Suppose that we want to generate a set of samples distributed according to a (not necessarily normalized) weight function  $W_\sigma$ . The Metropolis algorithm generates an arbitrarily long sequence of samples  $\{\sigma_k, k = 0, 1, 2, \dots\}$  as those field configurations visited successively by a random walker moving through  $\sigma$ -space; as the walk becomes longer and longer, the points it connects approximate more closely the desired distribution.

The rules by which the random walk proceeds through  $\sigma$ -space are as follows. Suppose that the walker is at a point  $\sigma_k$  in the sequence. To generate  $\sigma_{k+1}$ , it makes a trial step to a new point  $\sigma_t$ . This new point can be chosen in any convenient manner, for example uniformly at random within a multi-dimensional cube of small side  $\delta$  about  $\sigma_k$ . This trial step is then “accepted” or “rejected” according to the ratio

$$r = \frac{W_t}{W_k}, \quad (5.5)$$

where  $W_t$  is  $W$  evaluated at  $\sigma_t$  and  $W_k$  is  $W$  evaluated at  $\sigma_k$ . If  $r$  is larger than one, then the step is “accepted” (i.e., we put  $\sigma_{k+1} = \sigma_t$ ), while if  $r$  is less than one, the step is accepted with probability  $r$ . This latter is conveniently accomplished by comparing  $r$  with a random number  $\eta$  uniformly distributed in the interval  $[0, 1]$  and accepting the step if  $\eta < r$ . If the trial step is not accepted, then it is “rejected,” and we put  $\sigma_{k+1} = \sigma_k$ . These rules generate  $\sigma_{k+1}$ , and we can then go on to generate  $\sigma_{k+2}$  by the same process, making a trial step from  $\sigma_{k+1}$ . Any arbitrary point,  $\sigma_0$ , can be used as the starting point for the random walk.

To prove that the algorithm described above does indeed generate a sequence of points distributed according to  $W$ , let us consider a large number of walkers starting from different initial points and moving independently through  $\sigma$ -space. If  $N_k(\sigma)$  is the density of these walkers at step  $k$ , then the net number of walkers moving from field configuration  $\sigma$  to field configuration  $\rho$  in the next step is

$$\begin{aligned} \Delta N(\sigma) &= N_k(\sigma)P(\sigma \rightarrow \rho) - N_k(\rho)P(\rho \rightarrow \sigma) \\ &= N_k(\rho)P(\sigma \rightarrow \rho) \left[ \frac{N_k(\sigma)}{N_k(\rho)} - \frac{P(\rho \rightarrow \sigma)}{P(\sigma \rightarrow \rho)} \right]. \end{aligned} \quad (5.6)$$

Here,  $P(\sigma \rightarrow \rho)$  is the probability that a walker will make a transition to  $\rho$  if it is at  $\sigma$ . This equation shows that there is equilibrium (no net change in population) when

$$\frac{N_k(\sigma)}{N_k(\rho)} = \frac{P(\rho \rightarrow \sigma)}{P(\sigma \rightarrow \rho)} = \frac{N_e(\sigma)}{N_e(\rho)} \quad (5.7)$$

and that changes in  $N(\sigma)$  when the system is not in equilibrium tend to drive it toward equilibrium (i.e.,  $\Delta N(\sigma)$  is positive if there are “too many” walkers at  $\sigma$ , or if  $N_k(\sigma)/N_k(\rho)$  is greater than its equilibrium value). Hence it is plausible (and can be proved) that, after a large number of steps, the population of the walkers will settle down to its equilibrium distribution,  $N_e$ .

It remains to be shown that the transition probabilities of the Metropolis algorithm lead to an equilibrium distribution of walkers  $N_e(\sigma) \sim W_\sigma$ . For the random walk governed by the rules described above, the probability of making a step from  $\sigma$  to  $\rho$  is

$$P(\sigma \rightarrow \rho) = T(\sigma \rightarrow \rho)A(\sigma \rightarrow \rho), \quad (5.8)$$

where  $T$  is the probability of making a trial step from  $\sigma$  to  $\rho$  and  $A$  is the probability of accepting that step. If  $\rho$  can be reached from  $\sigma$  in a single step (i.e., if it is within a cube of side  $\delta$  centered about  $\sigma$ ), then  $T(\sigma \rightarrow \rho) = T(\rho \rightarrow \sigma)$ , so that the equilibrium distribution of the Metropolis random walkers satisfies

$$\frac{N_e(\sigma)}{N_e(\rho)} = \frac{A(\rho \rightarrow \sigma)}{A(\sigma \rightarrow \rho)}. \quad (5.9)$$

If  $W_\sigma > W_\rho$ , then  $A(\rho \rightarrow \sigma) = 1$  and  $A(\sigma \rightarrow \rho) = W_\rho/W_\sigma$ , while if  $W_\sigma < W_\rho$  then  $A(\rho \rightarrow \sigma) = W_\sigma/W_\rho$  and  $A(\sigma \rightarrow \rho) = 1$ . Hence, in either case, the equilibrium population of Metropolis walkers satisfies

$$\frac{N_e(\sigma)}{N_e(\rho)} = \frac{W_\sigma}{W_\rho} \quad (5.10)$$

so that the walkers are indeed distributed with the correct distribution.

Note that although we made the discussion concrete by choosing  $\sigma_t$  in the neighborhood of  $\sigma_k$ , we can use *any* transition and acceptance rules that satisfy

$$\frac{T(\rho \rightarrow \sigma)A(\rho \rightarrow \sigma)}{T(\sigma \rightarrow \rho)A(\sigma \rightarrow \rho)} = \frac{W_\sigma}{W_\rho}. \quad (5.11)$$

Indeed, one limiting choice is  $T(\sigma \rightarrow \rho) = W_\rho$ , independent of  $\sigma$ , and  $A = 1$ . This is the most efficient choice, as no trial steps are “wasted” through rejection. However, this choice is somewhat impractical, because if we knew how to sample  $W$  to take the trial step, we wouldn’t need to use the algorithm to begin with.

An obvious question is “If trial steps are to be taken within a neighborhood of  $\sigma_k$ , how do we choose the step size,  $\delta$ ?” To answer this, suppose that  $\sigma_k$  is at a maximum of  $W$ , the most likely place for it to be. If  $\delta$  is large, then  $W_t$  will likely be very much smaller than  $W_k$  and most trial steps will be rejected, leading to an inefficient sampling of  $W$ . If  $\delta$  is very small, most trial steps will be accepted, but the random walker will never move very far, and so also lead to a poor sampling of the distribution. A good rule of thumb is that the size of the trial step should be chosen so that about half of the trial steps are accepted.

One bane of applying the Metropolis algorithm is that the field configurations that make up the random walk,  $\sigma_0, \sigma_1, \dots$ , are not independent of one another, simply from the way in which they were generated; that is,  $\sigma_{k+1}$  is likely to be in the neighborhood of  $\sigma_k$ . Thus, while the samples might be distributed properly as the walk becomes very long, they are not statistically independent of one another, and some care must be taken in using them to evaluate observables. In particular, if we estimate  $\langle \hat{\Omega} \rangle$  from Eq. (5.3) using the successive field configurations in the random walk, the estimate of the variance given by Eq. (5.4) is invalid because the  $\Omega_k$  are not statistically independent. This error can be quantified by calculating the auto-correlation function

$$C_i = \frac{\langle \Omega_k \Omega_{k+i} \rangle - \langle \Omega_k \rangle^2}{\langle \Omega_k^2 \rangle - \langle \Omega_k \rangle^2}, \quad (5.12)$$

where  $\langle \dots \rangle$  indicates average over the random walk. Of course,  $C_0 = 1$ , but the non-vanishing of  $C_i$  for  $i > 0$  means that the  $\Omega_k$ 's are not independent. What can be done in practice is to compute the observable and its variance using samples along the random walk separated by a fixed interval, the interval being chosen so that there is effectively no correlation between the field configurations used. An appropriate sampling interval can be estimated from the value of  $i$  for which  $C_i$  becomes small (say  $< 0.1$ ).

Another issue in applying the Metropolis algorithm is where to start the random walk; i.e., what to take for  $\sigma_0$ . In principle, any location is suitable and the results will be independent of this choice, as the walker will “thermalize” after some number of steps. In practice, an appropriate starting point is a probable one, where  $W$  is large. Some number of thermalization steps then can be taken before actual sampling begins to remove any dependence on the starting point.

## 6 Numerical methods and computational issues

### 6.1 Number projection

For large quantum systems in which many valence fermions participate, the grand canonical ensemble (with a fixed chemical potential, but fluctuating particle number) is perfectly acceptable, and simple formulas exist for calculating the required one-body observables (e.g., Eqs. (A.15,16)). But in nuclei, where only a few valence fermions are important in determining the low lying states, and the properties of neighboring even- $A$  and odd- $A$  systems differ dramatically, the canonical (fixed-number) ensemble must be used. In this section, we discuss how to project the fixed-number trace from the grand-canonical ensemble. For simplicity, we will consider only a single species of fermions with number operator  $\hat{N}$ ; the required generalization to two species (protons and neutrons) is straightforward, as the HS transformation used does not involve density operators that mix the species, so that  $\hat{U}_\sigma$  factors into separate evolution operators for neutrons and protons.

The grand canonical partition function for a one-body evolution operator  $\hat{U}_\sigma$  is given by Eq. (A.12) as

$$Z = \text{Tr} e^{\beta\mu\hat{N}}\hat{U}_\sigma = \det(1 + e^{\beta\mu}\mathbf{U}_\sigma) , \quad (6.1)$$

where  $\mu$  is the chemical potential. Note that since the matrix corresponding to  $\hat{N}$  is simply the unit matrix, we may include the chemical potential term in each of the  $\hat{h}$  defining  $\hat{U}_\sigma$ , or write it as a common prefactor, as we have done in (6.1). If we write the  $N_s$  eigenvalues of  $\mathbf{U}_\sigma$  as  $e^{-\beta\varepsilon_\lambda}$ , where  $\varepsilon_\lambda$  may be complex, we can express (6.1) as

$$Z = \prod_\lambda (1 + e^{\beta(\mu - \varepsilon_\lambda)}) , \quad (6.2)$$

which is a form reminiscent of the usual fermi-gas expressions.

The corresponding canonical partition function for  $A$  particles in the valence space is

$$Z_A = \text{Tr}_A \hat{U}_\sigma = \text{Tr} \hat{P}_A \hat{U}_\sigma , \quad (6.3)$$

where  $\hat{P}_A = \delta(A - \hat{N})$  is the number projector. To effect the operation of  $\hat{P}_A$ , we can write it as the exponential of the one-body operator  $\hat{N}$  using the fact that  $\hat{N}$  has integer eigenvalues

$0, 1, \dots, N_s$ :

$$\hat{P}_A = e^{-\beta\mu A} \int_0^{2\pi} \frac{d\phi}{2\pi} e^{-i\phi A} e^{(\beta\mu+i\phi)\hat{N}} , \quad (6.4)$$

where  $\mu$  is an arbitrary  $c$ -number, which will be specified below.

The canonical trace thus becomes

$$Z_A = e^{-\beta\mu A} \int_0^{2\pi} \frac{d\phi}{2\pi} e^{-i\phi A} \text{Tr} e^{(\beta\mu+i\phi)\hat{N}} \hat{U}_\sigma \quad (6.5a)$$

$$= e^{-\beta\mu A} \int_0^{2\pi} \frac{d\phi}{2\pi} e^{-i\phi A} \prod_\lambda (1 + e^{i\phi} e^{\beta(\mu-\varepsilon_\lambda)}) . \quad (6.5b)$$

From (6.5b), we can see that the effect of the number projection is to sum all different products of  $A$  terms of the form  $e^{-\beta\varepsilon_\lambda}$ . Similar expressions can be written for expectation values of few-body operators following Eqs. (A.15, A.16). For example, for a one-body operator  $\hat{\Omega}$ ,

$$\text{Tr}_A \hat{U}_\sigma \hat{\Omega} = e^{-\beta\mu A} \int_0^{2\pi} \frac{d\phi}{2\pi} e^{-i\phi A} \det(1 + e^{\beta\mu+i\phi} \mathbf{U}_\sigma) \text{tr} \frac{1}{1 + e^{\beta\mu+i\phi} \mathbf{U}_\sigma} e^{\beta\mu+i\phi} \mathbf{U}_\sigma \Omega . \quad (6.6)$$

The parameter  $\mu$  is arbitrary and hence can be chosen for numerical convenience. Since the grand-canonical trace in the integrand of (6.5b) contains contributions from canonical ensembles with all  $0 \leq A \leq N_s$ , and these vary strongly with  $A$ ,  $\mu$  should be chosen to emphasize that contribution from the particular value of  $A$  desired; a poor choice can lead to numerical difficulties in the projection. This can be done in analogy with usual thermodynamic treatment. In particular, if the eigenvalues of  $\mathbf{U}_\sigma$  are ordered so that  $\text{Re} \varepsilon_1 \leq \text{Re} \varepsilon_2 \leq \dots \leq \text{Re} \varepsilon_{N_s}$ , then a good choice for  $\mu$  is  $(\text{Re} \varepsilon_A + \text{Re} \varepsilon_{A+1})/2$ .

The numerical effort implied by Eqs. (6.5) or (6.6) need not be intimidating. First, because the integer eigenvalues of  $\hat{N}$  range from 0 to  $N_s$ , the maximal Fourier component in the  $\phi$  integration is  $e^{iN_s\phi}$ , so that an  $N_s$ -point quadrature can be exact. That is, for  $f(\phi)$  one of the required integrands,

$$\int_0^{2\pi} \frac{d\phi}{2\pi} f(\phi) = \frac{1}{N_s} \sum_{m=1}^{N_s} f(\phi_m); \quad \phi_m \equiv \frac{m \cdot 2\pi}{N_s} . \quad (6.7)$$

Second, the matrix algebra associated with expressions like (6.6) is minimized by computing only once both the eigenvalues  $e^{-\beta\varepsilon_\lambda}$  and the diagonalizing transformation matrix  $\mathbf{T}_{\alpha\lambda}$  of  $\mathbf{U}_\sigma$  and then using these to evaluate the integrand at each quadrature point  $\phi_m$ . Thus, for example, (6.5b) is simply evaluated, and the matrix trace required in the integral of (6.6) is evaluated as

$$\sum_{\lambda=1}^{N_s} \frac{1}{1 + e^{\beta(\mu-\varepsilon_\lambda)+i\phi}} e^{\beta(\mu-\varepsilon_\lambda)+i\phi} \sum_{\alpha\beta=1}^{N_s} \mathbf{T}_{\lambda\alpha} \Omega_{\alpha\beta} \mathbf{T}_{\beta\lambda} . \quad (6.8)$$

## 6.2 Auxiliary field quadrature

When the number of auxiliary field variables becomes large, naive application of the sampling algorithm of Metropolis *et al.* as described in Section 5 becomes inefficient. For example, in

the  $^{170}\text{Dy}$  calculation described in Section 8.8 where there are some  $10^5$  fields, when the step size  $\delta$  (taken to be the same for each field variable) is adjusted so that the acceptance ratio is approximately 0.5, the auto correlation length for the energy (as computed from Eq. (5.12)) is more than 200 sweeps (i.e., more than 200 updates of the field variables at each time slice).

The Metropolis efficiency in generating uncorrelated field configurations can be improved significantly by approximating the continuous integral over each  $\sigma_{an}$  by a discrete sum derived from a Gaussian quadrature [59]. In particular, the relation

$$e^{\Delta\beta V \hat{O}^2/2} \approx \int_{-\infty}^{\infty} d\sigma f(\sigma) e^{\Delta\beta V \sigma \hat{O}} \quad (6.9)$$

is satisfied through terms in  $(\Delta\beta)^2$  if

$$f(\sigma) = \frac{1}{6} [\delta(\sigma - \sigma_0) + \delta(\sigma + \sigma_0) + 4\delta(\sigma)] , \quad (6.10)$$

where  $\sigma_0 = (3/V\Delta\beta)^{1/2}$ . (Note that the commutator terms render the HS transformation accurate only through order  $\Delta\beta$  anyway.)

In this way, each  $\sigma_{an}$  becomes a 3-state variable and the integrals in (3.19) become (very large) sums, which can be sampled using the algorithm of Metropolis *et al.* In particular, to update the fields at a given time slice, we select at random a fraction  $q$  of them and assign each of these to  $(-\sigma_0, 0, \text{ or } \sigma_0)$  with probability  $(1/6, 2/3, \text{ and } 1/6)$ . To satisfy the condition (5.11), the move is then accepted or rejected according to the ratio of the old and trial values of  $\text{Tr}_A \hat{U}_\sigma$ . The fraction  $q$  is adjusted to give an acceptance ratio of about 0.5. When used in the  $^{170}\text{Dy}$  calculation, this discretization reduces the energy autocorrelation length to only five sweeps, a factor of 40 improvement relative to the continuous case, with no loss of accuracy. Similar, albeit less substantial, savings accrue in smaller calculations.

### 6.3 Stabilization at low temperatures

The excitation energy of the first excited state in even-even nuclei with  $A \leq 80$  is 1-2 MeV. Thus, one may calculate at a temperature of  $T = 0.5$  MeV to get a reasonable description of the ground state. However, in odd- $A$  and odd-odd systems the excitation energy can be as low as tens of keV, so that cooling to the ground state requires calculations at  $\beta > 2.0$  MeV $^{-1}$ . Unfortunately, numerical instabilities arise for larger  $\beta$  due to the multiplication of many  $\mathbf{U}$  matrices together; the product becomes increasingly illconditioned, with exponentially divergent numerical scales, as illustrated below.

Physically, the one-body evolution operator  $\hat{U}_n$  amplifies low-energy states for any particular field configuration, and attenuates high-energy states. The most important states, those near some intermediate Fermi surface, are buried exponentially by the states at the bottom of the spectrum, and extraction of relevant information becomes increasingly difficult with lower temperatures. This technical problem, resulting from the limits of finite numerical precision achievable on any digital computer, can be circumvented using singular value decomposition (SVD) methods, which were first applied in Green's Function Monte Carlo simulations of interacting electron systems [53]. Here we adapt the SVD methods to the canonical calculations of the nuclear problem.

Let us suppose that a matrix  $\mathbf{A}$  can be decomposed into three matrices,  $\mathbf{A} = \mathbf{SDV}$ , where  $\mathbf{S}^\dagger\mathbf{S} = \mathbf{1}$ ,  $\mathbf{V}^\dagger\mathbf{V} = \mathbf{1}$ , and  $\mathbf{D}$  is a real, diagonal matrix. Schematically, this decomposition looks like

$$\begin{aligned} \mathbf{SDV} &= \begin{pmatrix} x & x & x \\ x & x & x \\ x & x & x \end{pmatrix} \begin{pmatrix} X & & \\ & x & \\ & & x \end{pmatrix} \begin{pmatrix} x & x & x \\ x & x & x \\ x & x & x \end{pmatrix} \\ &= \begin{pmatrix} X & X & X \\ X & X & X \\ X & X & X \end{pmatrix}, \end{aligned} \tag{6.11}$$

where the size of the symbols ( $X, x, x$ ) indicates the magnitude of the elements. Note that  $\mathbf{S}$  and  $\mathbf{V}$  are well controlled matrices shown schematically as having unit scale, and that all the scales of the original matrix  $\mathbf{A}$  are contained in  $\mathbf{D}$ . Note also that once the multiplication has been performed all elements of the resulting matrix are of the same (largest) scale, and the product is essentially an outer product of the first column of  $\mathbf{S}$  and the first row of  $\mathbf{V}$ . The smallest numerical scales exist only implicitly as differences of large matrix elements, and as such are difficult to recover on a computer with finite precision.

In contrast, a matrix that explicitly displays its small scales, such as a column stratified matrix  $\mathbf{M}$ , can be factored stably.

$$\begin{aligned} \mathbf{S}^{-1}\mathbf{M}\mathbf{V}^{-1} &= \begin{pmatrix} x & x & x \\ x & x & x \\ x & x & x \end{pmatrix} \begin{pmatrix} X & x & x \\ X & x & x \\ X & x & x \end{pmatrix} \begin{pmatrix} x & x & x \\ x & x & x \\ x & x & x \end{pmatrix} \\ &= \begin{pmatrix} X & & \\ & x & \\ & & x \end{pmatrix} = \mathbf{D}. \end{aligned} \tag{6.12}$$

Multiplication on the left of  $\mathbf{M}$  by a transformation matrix combines only elements in a given column which are all of the same scale. Thus there is no loss of information. Multiplication on the right by  $\mathbf{V}^{-1}$  combines columns of different scales, but does not overwrite any small scale as long as large scaled columns are scaled down appropriately before the addition.

These problems are quantified by the condition number, defined as the ratio of the largest element of  $\mathbf{D}$  to the smallest after the transformation has taken place. When this ratio is greater than the machine accuracy (usually about  $10^{12}$  for double precision), then the calculation will become unstable, and techniques of stable matrix multiplication must be employed. Numerical problems first occur in the multiplication of  $\mathbf{U}_n$  matrices to create  $\mathbf{U} = \prod_{n=1}^{N_t} \mathbf{U}_n$ . Although each  $\mathbf{U}_n$  has a good condition number, the final product can have an unacceptable condition number. The above examples can be combined to disentangle the scales inherent in the multiplication of the  $\mathbf{U}_n$  matrices.

SVD matrix multiplication works by isolating the scales of the problem at each multiplication step. Let the matrix  $\mathbf{W}_n = \prod_{m=1}^{n \leq N_t} \mathbf{U}_m$ , be the partial product of the matrix multiplications, with  $\mathbf{W}_0 = \mathbf{1}$ ,  $\mathbf{W}_1 = \mathbf{U}_1$ ,  $\mathbf{W}_2 = \mathbf{U}_2\mathbf{U}_1$ , etc. Suppose we have already decomposed the matrix  $\mathbf{W}_n$  in SVD format. We want to multiply the well-conditioned matrix  $\mathbf{U}_n$  with

$\mathbf{W}_{n-1}$ . The multiplication proceeds as follows:

$$\mathbf{U}_n \mathbf{W}_{n-1} = (\mathbf{U}_n \mathbf{S}_{n-1} \mathbf{D}_{n-1}) \mathbf{V}_{n-1} = \left[ \mathbf{U}_n \mathbf{S}_{n-1} \begin{pmatrix} X & & \\ & x & \\ & & x \end{pmatrix} \right] \mathbf{V}_{n-1}. \quad (6.13)$$

Multiplication of the matrices in brackets yields a column stratified matrix that can be put into SVD format (i.e.,  $\mathbf{S}'\mathbf{D}'\mathbf{V}'$ ) without loss of scale. Thus

$$\mathbf{U}_n \mathbf{W}_{n-1} = \begin{pmatrix} X & x & x \\ X & x & x \\ X & x & x \end{pmatrix} \mathbf{V}_{n-1} = (\mathbf{S}'\mathbf{D}'\mathbf{V}') \mathbf{V}_{n-1} = \mathbf{S}'\mathbf{D}'(\mathbf{V}'\mathbf{V}_{n-1}) = \mathbf{S}_n \mathbf{D}_n \mathbf{V}_n, \quad (6.14)$$

where in the last step we have defined  $\mathbf{S}_n = \mathbf{S}'$ ,  $\mathbf{D}_n = \mathbf{D}'$ , and  $\mathbf{V}_n = \mathbf{V}'\mathbf{V}_{n-1}$ . Provided that the  $\mathbf{V}$  matrices are sufficiently well-conditioned that we can multiply many of them together without scale problems, we are able to perform stable matrix multiplication of all the one-body evolution operators.

For evaluation of the quantum mechanical trace, we need to calculate  $\mathbf{1} + \mathbf{U}_\sigma$  consistent with SVD. We assume that SVD has previously been performed on  $\mathbf{U}_\sigma$  such that  $\mathbf{U}_\sigma = \mathbf{S}\mathbf{D}\mathbf{V}$ . The goal is to keep all of the large scales in the problem separated from the small ones. This is done by calculating

$$\det(\mathbf{1} + \mathbf{U}_\sigma) = \det[\mathbf{S}(\mathbf{S}^{-1}\mathbf{V}^{-1} + \mathbf{D})\mathbf{V}] = \det \mathbf{S} \tilde{\mathbf{S}} \tilde{\mathbf{D}} \tilde{\mathbf{V}} \mathbf{V} = \det \mathbf{S}' \det \mathbf{D}' \det \mathbf{V}'. \quad (6.15)$$

Here we have performed a new SVD on the matrix in parenthesis to get  $\tilde{\mathbf{S}}\tilde{\mathbf{D}}\tilde{\mathbf{V}}$  (after the addition of  $\mathbf{S}^{-1}\mathbf{V}^{-1}$  to  $\mathbf{D}$ ), and we define  $\mathbf{S}' = \mathbf{S}\tilde{\mathbf{S}}$  and  $\mathbf{V}' = \mathbf{V}\tilde{\mathbf{V}}$ . The other quantity we need is

$$(\mathbf{1} + \mathbf{U}_\sigma)^{-1} \mathbf{U}_\sigma = \mathbf{1} - \frac{\mathbf{1}}{\mathbf{1} + \mathbf{U}_\sigma} = \mathbf{1} - \mathbf{V}'^{-1} \mathbf{D}'^{-1} \mathbf{S}'^{-1}, \quad (6.16)$$

where we have used the inverses of the matrices calculated in Eq. (6.15). These steps can be carried over exactly into the number projection method described in section (6.1).

As an example we consider the matrix multiplications to obtain  $\mathbf{U}_\sigma$  for  $^{54}\text{Fe}$  in the course of the calculations described in section 8.1. Shown in Fig. 6.1 is an example of the condition number with and without SVD for various  $\beta$ , with  $\Delta\beta = 1/16 \text{ MeV}^{-1}$ . Numerical round-off causes the condition number to virtually saturate in the non-SVD case. Shown in Fig. 6.2 are the elements of the diagonal matrix  $\mathbf{D}$  using SVD for all multiplies, compared to using SVD only on the full  $\mathbf{U}_\sigma$ . Note that the symmetry of  $\mathbf{U}_\sigma$  (that eigenvalues come in complex conjugate pairs, see section 7.1) is evident when the matrix-multiplies are accomplished through SVD, where the *real* elements of  $\mathbf{D}$  come in pairs. This is not the case without SVD multiplication. The numerical eigenvalues of  $\mathbf{U}_\sigma$  violate the symmetry only after  $\beta \geq 2.0$  (and at larger  $\beta$  in larger systems).

We have made limited use of SVD in the calculations presented in this Report. In test calculations we find that we can increase  $\beta$  almost indefinitely (e.g. to  $\beta = 6$  in  $^{22}\text{Ne}$ ) with SVD, whereas without the stabilization, the maximum attainable  $\beta$  is  $2.0 \text{ MeV}^{-1}$ . In the  $^{170}\text{Dy}$  and  $\text{Xe}$  calculations described in section 8,  $\beta = 5 \text{ MeV}^{-1}$  is attainable without SVD.

## 6.4 Maximum entropy techniques

The response functions that can be evaluated in SMMC are given by Eq. (3.6). Calculation of the strength function  $S_\Omega(E)$  for a given operator can be difficult due to the ill-posed inversion of the Laplace transform required by Eq. (3.8a). In this section, we discuss one particular inversion technique, Maximum Entropy (MaxEnt), which we have used to find the Gamow-Teller strength functions presented in section 8.6.

We wish to find the function  $S(E)$  from the function  $R(\tau)$  using the kernel  $K(\tau, E)$ :

$$R(\tau) = \int dE K(\tau, E) S(E) . \quad (6.17)$$

The function  $R(\tau)$  is known at  $N$  grid points  $\tau_i$  ( $i = 1, \dots, N$ ), where the values of  $R$  are given at  $\tau_i$  by  $r_i$  with errors  $\sigma_i$ . Fluctuations in different data points may be correlated, in which case the covariance matrix  $C_{ij} = \langle (r_i - \bar{r}_i)(r_j - \bar{r}_j) \rangle$  is diagonalized to find the independent modes, and  $r_i$  and the kernel are then transformed to this new basis. The goal is to find the best  $S(E)$  by analysing the  $\chi^2$  figure of merit,

$$\chi^2 \{S\} = \sum_i \left( \frac{r_i - R_i \{S\}}{\sigma_i} \right)^2 , \quad (6.18)$$

of the data  $r_i$  from the fit values  $R_i$  produced by the trial inverse in the points  $\tau_i$ ,

$$R_i \{S\} = \int dE K(\tau_i, E) S(E) . \quad (6.19)$$

Direct minimization of  $\chi^2$  is numerically stable in only the simplest of circumstances. Most of the modern ways to regularize the problem are based on combining  $\chi^2$  with some other auxiliary well-conditioned functional,  $P \{S\}$ . This functional should have a minimum at a smooth function  $S(E)$  and assign a high cost to strongly oscillating functions. Thus we minimize the joint functional

$$\frac{1}{2} \chi^2 \{S\} + P \{S\} . \quad (6.20)$$

We use the information-theoretic entropy to define  $P \{S\}$  such that

$$P \{S\} = \alpha \int dE \left[ m(E) - S(E) + S(E) \ln \left( \frac{S(E)}{m(E)} \right) \right] , \quad (6.21)$$

where  $m(E)$ , the default model, and  $\alpha$  are chosen to describe the *a priori* knowledge about the shape of the original  $S(E)$ . The choice of  $m(E)$  and  $\alpha$  is more doubtful than the MaxEnt technique itself. In our application to the Gamow-Teller strength functions we make the simplifying assumption that  $m(E)$  is a Gaussian function with appropriately chosen center (see section 8.6), and  $\alpha = [\int dE m(E)]^{-1}$ .

In order to minimize the functional (6.20) we employ the technique of Ref. [54], which involves an iterative sequence of linear programming problems. To do this we first expand Eq. (6.21) to second order in  $S(E)$  about some positive function  $f(E)$ , to obtain

$$P \{f | S\} = \alpha \int dE \left\{ \left( m - \frac{f}{2} \right) + \left[ \ln \left( \frac{f}{m} \right) - 1 \right] S + \frac{S^2}{2f} \right\} . \quad (6.22)$$

If the true minimum  $S(E)$  of the non-quadratic functional in Eq. (6.21) is taken as a point of expansion  $f(E)$  in (6.22), then it also gives the minimum of the corresponding quadratic functional

$$S(E) = \min_a \left[ \frac{1}{2} \chi^2 \{a\} + P \{S | a\} \right] . \quad (6.23)$$

We transform this identity to a recursive equation that, upon iteration, leads to the desired solution. To ensure positivity we keep a fraction of the result of the previous iteration in the next one, and minimize the functional with the restriction that  $S \geq 0$ . Defining  $n$  as the iteration step, we obtain,

$$S^{(n+1)} = \min_{S \geq 0} \left[ \frac{1}{2} \chi^2 \{S\} + P \{f^{(n)} | S\} \right] , \quad (6.24)$$

with

$$f^{(n)}(E) = \xi S^{(n-1)}(E) + (1 - \xi) S^{(n)}(E) , \quad (6.25)$$

and the default model is taken as the starting approximation to  $S$ ,

$$S^{(0)}(E) = S^{(-1)}(E) = m(E) . \quad (6.26)$$

The rate of convergence and stability are controlled by the mixing parameter  $\xi$ ; a value of  $\xi = 0.3$  is a reasonable choice to guarantee stability.

Each iteration is a linear regularization task with a quadratic regularization functional reinforced by an additional stabilizing effect of the constraints  $S(E) \geq 0$ . Thus, each iteration gives a nonnegative function  $S^{(n)}(E)$  and a positive definite function  $f^{(n)}(E)$ . Test cases of simulated data for which the answer is known give convergence within twenty iterations.

We have used the technique described above to obtain the strength functions from the Gamow-Teller response functions, as presented in section 8.6. A different approach to MaxEnt was outlined in [27], but has proven less useful due to difficulties in obtaining a converged value of  $\alpha$ . The advantage of the present method is that knowledge of  $\alpha$  is not necessary, and that the scheme provides an iterative method of converging to the most likely solution.

## 6.5 Computational considerations

The present SMMC code is roughly the fourth major revision of a program whose development began in late 1990 with a single-species, single- $j$ -shell version. It is now a modular package of some 10,000 commented lines of FORTRAN. All floating point computations are double precision (64-bit).

The package performs all of the functions necessary for shell model Monte Carlo calculations: initialization, thermalization of the Metropolis walk, generation of the Monte Carlo samples, evaluation of static observables and response functions (canonical or grand-canonical), MaxEnt extraction of strength functions, and the extrapolation in  $g$  required to solve the sign problem, as discussed in section 7. Samples may be analyzed “on-line” and/or stored for post-processing in subsequent runs. The data input and results output use standard shell model conventions, so that it is easy to change the two-body matrix elements of the interaction, to incorporate additional one- or two-body observables in the analysis, or

to add or change the orbitals in the calculation. The code has been de-bugged and tested extensively against direct diagonalization results in the *sd*- and lower *pf*-shells. Its operation by an experienced user can be described as “routine,” although it takes several weeks to acquire that experience.

The SMMC package is highly portable. Initial development was largely under VAX/VMS. Subsequently, we have ported the code to DEC ALPHA’s and HP 730’s operating under Unix, the Intel i860 CPU used in the DELTA and PARAGON parallel machines, the IBM RS-6000 processor used in both workstations and the SP-1 and SP-2 parallel machines, and the Fujitsu VPP500 shared memory machine (at RIKEN). Very few problems are encountered in porting to a new machine, and the operation generally takes less than a day.

Shell model Monte Carlo calculations are extraordinarily well-suited to Multiple Instruction/Multiple Data (MIMD) architectures. Indeed, our code is “embarrassingly parallel”: separate Metropolis random walks are started on each computational node, which then produces a specified number of Monte Carlo samples at regular intervals during the walk. Data from all of the nodes are sent to a central node for evaluation of the Monte Carlo averages and their uncertainties, and perhaps for storage of the sampled field configurations in a file for post-analysis. The post-processing of the stored samples is also divided among the nodes.

To date, we have implemented the parallel version of our code on the Intel DELTA, and PARAGON machines at Caltech (each with 512 i860 processors), on the 128-processor IBM SP-1 at ANL, the 512-processor IBM SP-2 at Maui, and on a Fujitsu VPP500 shared memory vector processor (24 CPU’s). In all cases, the ratio of communications to computation is very low, with efficiencies always greater than 95%.

To circumvent the limited memory on the DELTA (12.5 MBytes) nodes, we have also produced a version of the code in which the chains of  $U_\sigma$  matrices effecting the time evolution are split over two or more nodes, information being passed between them only at the time slice where they “join.” However, such an implementation is a significant sacrifice in speed, as while one processor updates a chain, the other processors working on the same chain must sit idle.

Table 1 shows benchmarks of our code on various single processors. The test calculation involved a canonical ensemble in the full *pf*-shell ( $N_s = 20$  for each type of nucleon, implying  $20 \times 20$  matrices) using a realistic interaction.  $N_t = 32$  time slices were used at  $\beta = 2 \text{ MeV}^{-1}$  ( $\Delta\beta = 0.0625 \text{ MeV}^{-1}$ ). Thirty static observables and seven dynamical response functions were calculated at a single  $g$ -value (see section 7). Note that the computational speed is independent of the interaction and of the number of nucleons occupying the shell. Beyond using library subroutines (BLAS and LAPACK routines), no attempt was made to optimize the assembly level code in any of these cases. Approximately 40% of the computational effort is in matrix-multiplies. A significant remainder of the effort goes into building the one-body Hamiltonian (13%), setting up the one-body evolution operators (15%), and calculating two-body observables (15%), none of which is easily vectorizable.

In general, the computation time scales as  $N_s^3 N_t$ , and is spent roughly equally on the dynamical response functions and the static observable sampling. Of course, the stabilization discussed above increases these times significantly (by at least a factor of 5).

The memory required for our calculations scales as  $\bar{N}_s^2 N_t$ .  $\bar{N}_s^2$  is the average of the squares of the numbers of neutron and proton single-particle states. Sample values of  $N_s$  for one isospin type are shown for various model spaces in Table 2.

Processor	Peak MF	Average MF	Samples/hr.
i860	35	9	44
IBM-SP2 Thin66	56	36	179
ALPHA-400	56	28	141

Table 1: Benchmarks of the SMMC code in various processors.

Model Space	$N_s$
$0p$	6
$1s-0d$	12
$1p-0f$	20
$1p-0f-g_{9/2}$	30
$2s-1d-0g$	30
$2p-1f-0g_{9/2}-0i_{13/2}$	44

Table 2: Matrix dimension for various model spaces.

The code is currently structured so that a calculation with  $\bar{N}_s = 32$ , six  $j$ -orbitals, and  $N_t = 64$  time slices will fit in 12 MB of memory (note that all field variables are stored as 1-byte integers because of the 3-point Gauss-Hermite quadrature described in section 6.2). A calculation in the  $(1p-0f)$ - $(2s-1d-0g)$  basis has  $\bar{N}_s = 50$  and would require about 64 MB of memory for  $N_t = 64$  time slices and about 128 MB for  $N_t = 128$ . For calculations with a “good” Hamiltonian, as defined in the next section, these storage estimates can be reduced by a factor of two by exploiting the time reversal symmetry of the  $U_\sigma$ , albeit at some loss in speed.

## 6.6 Contrast with interacting electron systems

It is interesting to contrast the SMMC simulations of nuclear systems with similar work on the Hubbard model in the context of high-temperature superconductivity. The latter involve electrons hopping locally on a two-dimensional spatial lattice interacting with each other through an on-site repulsion. For a review of this field see [24].

One significant difference is that physically interesting SMMC calculations can be performed in smaller model spaces. The  $N_s$  values quoted in the previous section are significantly smaller than the number of sites needed to approximate the translational invariance of the CuO planes. However, the matrices representing the fluctuating one-body hamiltonians  $\hat{h}$  in SMMC calculations are dense, as the nuclear hamiltonian does not have the local spatial structure of the Hubbard model that gives rise to sparse  $\mathbf{h}$  matrices.

Another difference is that relatively higher temperatures are of interest in the nuclear case, allowing smaller  $N_t$ . For a nominal temperature of  $T = 300$  keV and strength of the two-body interaction  $V = 3$  MeV, we have  $T/V = 0.1$ . In the high- $T_c$  case,  $T \approx 10^2$  K  $\approx 10^{-2}$  eV, while  $V \approx 1$  eV, so  $T/V \approx 10^{-2}$ , an order of magnitude smaller.

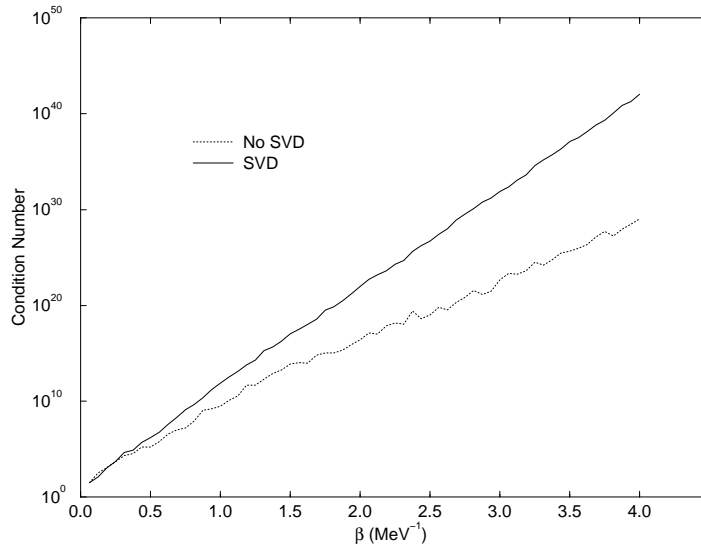


FIG 6.1 The condition number of  $\mathbf{U}_\sigma$  with and without SVD for various  $\beta$  is plotted for  $^{54}\text{Fe}$ .

The SMMC calculations must be performed in the canonical ensemble, as the effects of finite particle number are an important aspect of nuclear structure. This necessitates the rather cumbersome number projection described in section 6.1. In contrast, the Hubbard simulations can be done in the grand-canonical ensemble.

A final and most crucial difference between the SMMC and Hubbard hamiltonians is that the nuclear interaction is predominantly attractive. This significantly diminishes (and in some cases eliminates) the sign problems that plague the condensed matter work. These problems, and their resolution in SMMC calculations, are the subject of the following section.

## 7 Sign problems

Although we have briefly alluded to “sign problems” in some of the previous chapters, virtually all of our discussion has been based on the premise that the weight function  $W_\sigma$  of Eq. (3.19) is non-negative for all field configurations  $\sigma$ . Were this not the case, the function  $P_\sigma$  of Eq. (5.2) could not be interpreted as a probability density, and the MC quadrature described in section 5 could not be effected.

Unfortunately, many of the hamiltonians of physical interest suffer from a sign problem, in that  $W_\sigma$  is negative over significant fractions of the integration volume. To understand the implications of this, let us rewrite Eq. (5.1) as

$$\langle \hat{\Omega} \rangle = \int d^D \sigma P_\sigma \Phi_\sigma \Omega_\sigma, \quad (7.1)$$

where

$$P_\sigma = \frac{|W_\sigma|}{\int d^D \sigma |W_\sigma| \Phi_\sigma},$$

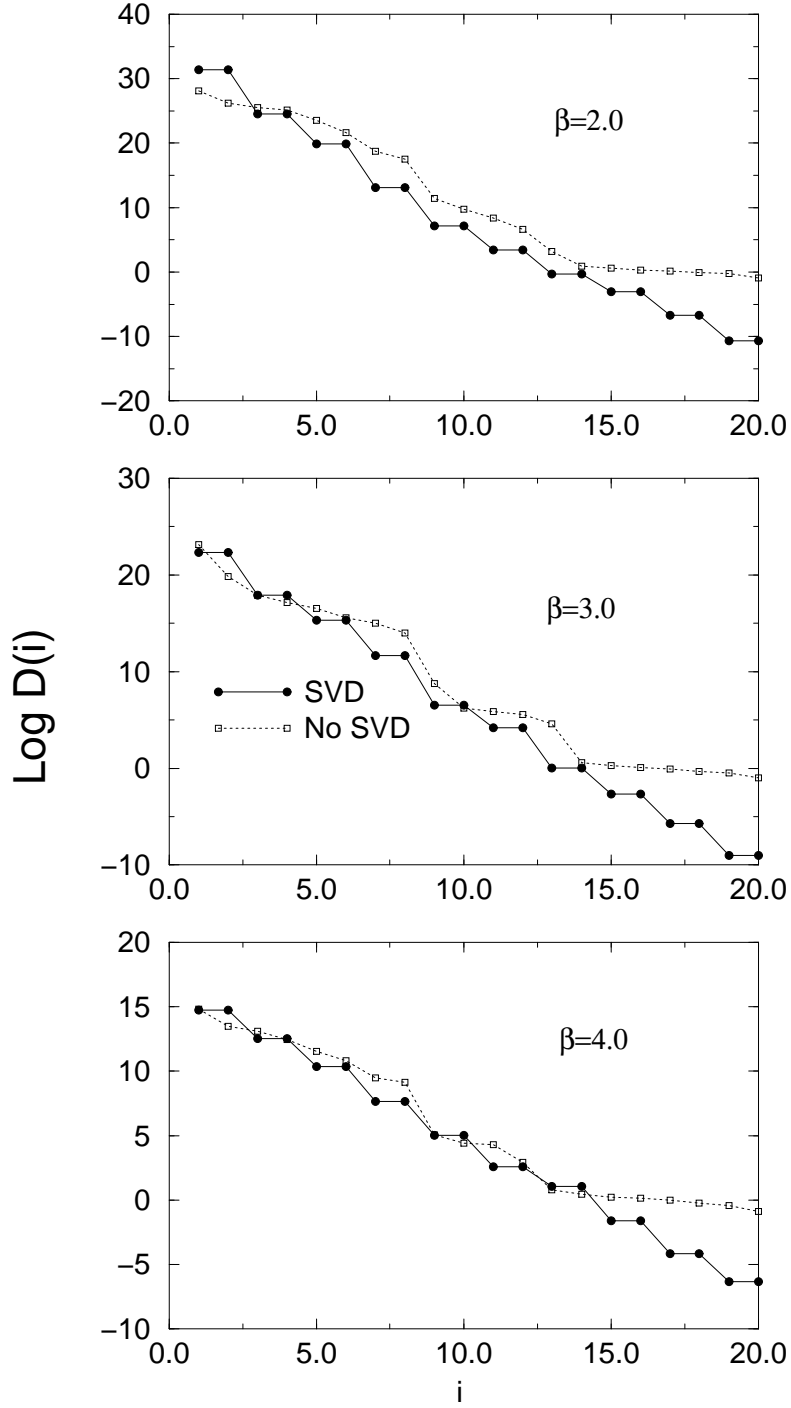


FIG 6.2. Elements of the diagonal matrix  $\mathbf{D}$  are shown when SVD is used for all multiplies of the  $\mathbf{U}_n$ , compared with those obtained when SVD is performed only on the final matrix  $\mathbf{U}_\sigma$ .

and  $\Phi_\sigma = W_\sigma / |W_\sigma|$  is the sign of the real part of  $W_\sigma$ . (Note that since the partition function is real, we can neglect the imaginary part.) Since  $|W_\sigma|$  is non-negative by definition, we can interpret it, suitably normalized, as a probability density, so that upon rewriting (7.1) as

$$\langle \hat{\Omega} \rangle = \frac{\int d\sigma |W_\sigma| \Phi_\sigma \Omega_\sigma}{\int d\sigma |W_\sigma| \Phi_\sigma} = \frac{\langle \Phi \hat{\Omega} \rangle}{\langle \Phi \rangle}, \quad (7.2)$$

we can think of the observable as a ratio in which the numerator and denominator can be separately evaluated by MC quadrature. Leaving aside the issue of correlations between estimates of these two quantities (they can always be evaluated using separate Metropolis walks), the fractional variance of  $\langle \hat{\Omega} \rangle$  will be

$$\frac{\sigma_\Omega}{\langle \hat{\Omega} \rangle} = \sqrt{\frac{\langle \hat{\Omega}^2 \rangle}{\langle \Phi \hat{\Omega} \rangle^2} + \frac{1}{\langle \Phi \rangle^2} - 2}, \quad (7.3)$$

which becomes unacceptably large as the average sign  $\langle \Phi \rangle$  approaches zero. The average sign of the weight thus determines the feasibility of naive MC quadrature. Only a handful of interacting electron systems are known to give rise to a positive-definite path integral [24]: the one-dimensional Hubbard model, the half-filled Hubbard model, and the attractive Hubbard model at any dimension and filling.

When  $\langle \Phi \rangle$  is near unity, we can attempt MC evaluation of the numerator and denominator separately, as will be illustrated in the example of section 8.8 below. However, for the most general case, we must have a deeper understanding of the sign problem. We rewrite the canonical expectation value of an observable  $\hat{\Omega}$  as

$$\langle \hat{\Omega} \rangle \equiv \frac{\text{Tr}(\hat{\Omega} e^{-\beta \hat{H}})}{\text{Tr}(e^{-\beta \hat{H}})} \approx \frac{\int D\sigma W_\sigma \Phi_\sigma \Omega_\sigma}{\int D\sigma W_\sigma \Phi_\sigma}, \quad (7.4)$$

where in the spirit of Eq. (7.1,7.2) we have introduced a positive definite weight

$$W_\sigma = G_\sigma | \text{Tr}_A \hat{U}_\sigma |, \quad (7.5)$$

and the Monte Carlo sign

$$\Phi_\sigma = \frac{\text{Tr}_A \hat{U}_\sigma}{| \text{Tr}_A \hat{U}_\sigma |}. \quad (7.6)$$

The sign problem arises because the one-body partition function  $\text{Tr}_A \hat{U}_\sigma$  is not necessarily positive, so that the Monte Carlo uncertainty in the denominator of Eq. (7.4) (the  $W$ -weighted average sign,  $\langle \Phi \rangle$ ) can become comparable to or larger than  $\langle \Phi \rangle$  itself. In most cases  $\langle \Phi \rangle$  decreases exponentially with  $\beta$  or with the number of time slices [53].

## 7.1 Hamiltonians without sign problems

An important class of interactions (pairing+quadrupole) free from the sign problem (i.e.,  $\Phi_\sigma \equiv 1$ ) was found in Ref. [27]. These are realized when  $V_\alpha \leq 0$  for all  $\alpha$  in Eq. (3.16). In that case,  $s_\alpha = 1$  for all  $\alpha$ , and, in the linearized hamiltonian given by Eq. (3.19c),  $\hat{O}$  and  $\hat{O}$

couple to complex conjugate fields. In order to understand the implications of this situation, we represent the single-particle wave function by an  $N_S$ -component vector of the form

$$\begin{pmatrix} jm \\ j\bar{m} \end{pmatrix}, \quad (7.7)$$

with  $N_S/2$  states  $m > 0$  in the first half of the vector, and their time reversed orbitals in the second half. Due to Eq. (3.16) and the fact that time-reversed operators are coupled to complex-conjugate fields, the matrix  $\mathbf{h}_n$  has the structure

$$\begin{pmatrix} \mathbf{A}_n & \mathbf{B}_n \\ -\mathbf{B}_n^* & \mathbf{A}_n^* \end{pmatrix}, \quad (7.8)$$

and one can easily verify that the total evolution matrix

$$\mathbf{U}_\sigma = \prod_n \exp(-\mathbf{h}_n \Delta\beta) = \begin{pmatrix} \mathbf{P} & \mathbf{Q} \\ -\mathbf{Q}^* & \mathbf{P}^* \end{pmatrix}, \quad (7.9)$$

is of the same form. Here  $\mathbf{A}$ ,  $\mathbf{B}$ ,  $\mathbf{P}$ , and  $\mathbf{Q}$  are matrices of dimension  $N_S/2$ . One can show that this matrix has pairs of complex-conjugate eigenvalues  $(\varepsilon, \varepsilon^*)$ , with respective eigenvectors  $\begin{pmatrix} u \\ v \end{pmatrix}$  and  $\begin{pmatrix} -v^* \\ u^* \end{pmatrix}$ . When  $\varepsilon$  is real, it is two-fold degenerate, since the two eigenvectors are distinct.

For the grand-canonical ensemble, the grand-canonical trace is given by

$$\text{Tr}\hat{U} = \det \left[ \mathbf{1} + \begin{pmatrix} \mathbf{P} & \mathbf{Q} \\ -\mathbf{Q}^* & \mathbf{P}^* \end{pmatrix} \right] = \prod_\lambda^{N_S/2} (1 + \varepsilon_\lambda)(1 + \varepsilon_\lambda^*) > 0. \quad (7.10)$$

If only particle-type conserving (neutron-proton) density operators are present in Eq. (3.16), each type of nucleon is represented by a separate Slater determinant having the structure (7.9) and therefore  $\text{Tr}\hat{U}_p \cdot \text{Tr}\hat{U}_n > 0$  since  $\text{Tr}\hat{U}_p > 0$  and  $\text{Tr}\hat{U}_n > 0$ .

In the zero-temperature formalism, if the trial wave function for an even number of particles is chosen to consist of time-reversed pairs of single particle states,

$$\Phi = \begin{pmatrix} \mathbf{a} & \mathbf{b} \\ -\mathbf{b}^* & \mathbf{a}^* \end{pmatrix}, \quad (7.11)$$

where  $\mathbf{a}$  and  $\mathbf{b}$  are matrices with dimension  $\left(\frac{N_s}{2} \times \frac{N_v}{2}\right)$ , then  $\Phi^\dagger \mathbf{U} \Phi$  is a  $N_v \times N_v$  matrix with the structure (7.9), and the trace satisfies

$$\text{Tr}\hat{U} = \det [\Phi^\dagger \mathbf{U} \Phi]. \quad (7.12)$$

If only particle-type conserving operators are present, then time-reversed pairs of trial wave functions can be chosen for both protons and neutrons in an even-even nucleus, giving rise to  $\text{Tr}\hat{U} = \text{Tr}\hat{U}_p \cdot \text{Tr}\hat{U}_n > 0$ . For  $N = Z$  odd-odd nuclei we can choose the final neutron to be in the time reversed orbit of the final proton, and the trace is once again positive.

Eq. (6.5b) embodies a proof that for even-even nuclei (and  $N = Z$  odd-odd systems) the partition function is real and positive definite under the condition that all  $V_\alpha < 0$ . This is

most easily seen for the case where  $N_s = 2$ , and  $A = 1$  or  $A = 2$ . From Eq. (6.5b), and using the  $N_s$ -point quadrature of Eq. (6.7),

$$\begin{aligned} Z_A &= \frac{1}{2} \sum_{m=1}^2 e^{(-i\phi_m A)} \prod_{\lambda=1}^2 \left[ 1 + e^{(i\phi_m)} e^{(-\beta\varepsilon_\lambda)} \right] \\ &= \frac{1}{2} \sum_{m=1}^2 \left\{ e^{(-i\phi_m A)} + e^{[-i\phi_m(A-2)]} e^{(-\beta 2\text{Re}\varepsilon_1)} + e^{[i\phi_m(A-1)]} \text{Re} e^{(-\beta\varepsilon_1)} \right\}, \end{aligned} \quad (7.13)$$

where we have ignored the  $e^{(-\beta\mu)}$  term for simplicity, and  $\phi_m = m\pi$ . It is easy to show that for  $A = 2$  the first and second terms survive the sum and that these terms are positive definite. It is also easy to show that for  $A = 1$  only the third term,  $\text{Re} e^{(-\beta\varepsilon_1)}$  remains after the sum is taken. While this term is real, it is not positive definite. Hence there appear two distinct sign problems. For even-even nuclei and all  $V_\alpha \leq 0$ , the sign problem can be overcome; however, for odd- $A$  nuclei, even with all  $V_\alpha \leq 0$ , the sign problem remains since the contributions to  $\langle \Phi \rangle$  are either positive (+1) or negative (-1), but not complex. This demonstration can be extended to all  $A$  in a given space. As in the zero-temperature formalism,  $N = Z$  odd-odd nuclei pose no sign problem, since the evolution is the same for both the protons and the neutrons, and the product of the traces is thus positive definite.

## 7.2 Practical solution to the sign problem

For an arbitrary hamiltonian, we are not guaranteed that all  $V_\alpha \leq 0$ . However, we may expect that a *realistic* hamiltonian will be dominated by terms like those of the schematic force (this is, after all, why the schematic forces were developed) so that it is, in some sense close to a hamiltonian for which the MC is directly applicable. Thus, the “practical solution” to the sign problem presented in Ref. [29] is based on an extrapolation of observables calculated for a “nearby” family of Hamiltonians whose integrands have a positive sign. Success depends crucially upon the degree of extrapolation required. Empirically, one finds that, for all of the many realistic interactions tested in the *sd*- and *pf*-shells, the extrapolation required is modest, amounting to a factor-of-two variation in the isovector monopole pairing strength.

Based on the above observation, it is possible to decompose  $\hat{H}$  in (3.16) into its “good” and “bad” parts,  $\hat{H} = \hat{H}_G + \hat{H}_B$ , with

$$\begin{aligned} \hat{H}_G &= \sum_{\alpha} (\epsilon_{\alpha}^* \hat{\mathcal{O}}_{\alpha} + \epsilon_{\alpha} \hat{\mathcal{O}}_{\alpha}) + \frac{1}{2} \sum_{V_{\alpha} < 0} V_{\alpha} \{ \hat{\mathcal{O}}_{\alpha}, \hat{\mathcal{O}}_{\alpha} \} \\ \hat{H}_B &= \frac{1}{2} \sum_{V_{\alpha} > 0} V_{\alpha} \{ \hat{\mathcal{O}}_{\alpha}, \hat{\mathcal{O}}_{\alpha} \}. \end{aligned} \quad (7.14)$$

The “good” Hamiltonian  $\hat{H}_G$  includes, in addition to the one-body terms, all the two-body interactions with  $V_{\alpha} \leq 0$ , while the “bad” Hamiltonian  $\hat{H}_B$  contains all interactions with  $V_{\alpha} > 0$ . By construction, calculations with  $\hat{H}_G$  alone have  $\Phi_{\sigma} \equiv 1$  and are thus free of the sign problem.

We define a family of Hamiltonians  $\hat{H}_g$  that depend on a continuous real parameter  $g$  as  $\hat{H}_g = f(g)\hat{H}_G + g\hat{H}_B$ , so that  $\hat{H}_{g=1} = \hat{H}$ , and  $f(g)$  is a function with  $f(1) = 1$  and  $f(g < 0) > 0$  that can be chosen to make the extrapolations less severe. (In practical

applications  $f(g) = 1 - (1 - g)/\chi$  with  $\chi \approx 4$  has been found to be a good choice.) If the  $V_\alpha$  that are large in magnitude are “good,” we expect that  $\hat{H}_{g=0} = \hat{H}_G$  is a reasonable starting point for the calculation of an observable  $\langle \hat{\Omega} \rangle$ . One might then hope to calculate  $\langle \hat{\Omega} \rangle_g = \text{Tr}(\hat{\Omega}e^{-\beta\hat{H}_g})/\text{Tr}(e^{-\beta\hat{H}_g})$  for small  $g > 0$  and then to extrapolate to  $g = 1$ , but typically  $\langle \Phi \rangle$  collapses even for small positive  $g$ . However, it is evident from our construction that  $\hat{H}_g$  is characterized by  $\Phi_\sigma \equiv 1$  for any  $g \leq 0$ , since all the “bad”  $V_\alpha (> 0)$  are replaced by “good”  $gV_\alpha < 0$ . We can therefore calculate  $\langle \hat{\Omega} \rangle_g$  for any  $g \leq 0$  by a Monte Carlo sampling that is free of the sign problem. If  $\langle \hat{\Omega} \rangle_g$  is a smooth function of  $g$ , it should then be possible to extrapolate to  $g = 1$  (i.e., to the original Hamiltonian) from  $g \leq 0$ . We emphasize that  $g = 0$  is not expected to be a singular point of  $\langle \hat{\Omega} \rangle_g$ ; it is special only in the Monte Carlo evaluation.

As described in Section 4, the matrices  $E_{KT}^\pi$  are constructed from the two-body matrix elements  $V_{JT}^\pi(ab, cd)$  of good angular momentum  $J$ , isospin  $T$ , and parity  $\pi = (-1)^{l_a+l_b}$  through a Pandya transformation. For interactions that are time-reversal invariant and conserve parity, the  $E_{KT}^\pi(i, j)$  (here  $\pi = (-1)^{l_a+l_c}$ ) are real symmetric matrices that can be diagonalized by a real orthogonal transformation. The eigenvectors  $\hat{\rho}_{KM}(\alpha)$  play the role of  $\hat{O}_\alpha$  in Eq. (3.16), and the eigenvalues  $\lambda_{K\pi}(\alpha)$  are proportional to  $V_\alpha$ . In the Condon-Shortley [60] convention  $\hat{\rho}_{KM} = \pi(-)^{K+M}\hat{\rho}_{K-M}$  so that the “good” eigenvalues satisfy  $\text{sign}[\lambda_{K\pi}(\alpha)] = \pi(-)^{K+1}$  [61].

As an example, we consider the mid- $pf$  shell nucleus  $^{54}\text{Fe}$  using the realistic Kuo-Brown KB3 interaction [19]. Figure 7.1 (upper) shows the eigenvalues  $V_{K\pi\alpha} = \pi(-)^K\lambda_{K\pi}(\alpha)$  of the KB3 interaction; only about half of the eigenvalues are negative. However, those with the largest magnitude are all “good.” It is possible to use an inverse Pandya transformation to calculate the two-body matrix elements  $V_{JT}^\pi(ab, cd)$  for the “good” and “bad” interactions, allowing the matrix elements of  $\hat{H}_G$  to be compared in Fig. 7.1 (lower) with those of the full interaction. The greatest deviation is for  $J = 0, T = 1$  (the monopole pairing interaction), where  $\hat{H}_G$  is about twice as attractive as the physical  $\hat{H}$ . In all other channels,  $\hat{H}_G$  and  $\hat{H}$  are quite similar.

In Fig. 7.2 we exemplify the  $g$ -extrapolation procedure for several observables, calculated again for  $^{54}\text{Fe}$ . In all cases we use polynomial extrapolations from negative  $g$ -values to the physical case,  $g = 1$ . The degree of the polynomial is usually chosen to be the smallest that yields a  $\chi^2$  per degree of freedom less than 1. However, in several studies, like the one of the  $pf$ -shell nuclei reported in section 8.1, we have conservatively chosen second-order polynomials for all extrapolations, although in many cases a first-order polynomial already resulted in  $\chi^2$ -values less than 1. At  $T = 0$  the variational principle requires that the expectation value of  $\hat{H}$  has a minimum at  $g = 1$ . We have incorporated this fact in our extrapolations of ground state energies by using a second-order polynomial with zero-derivative at  $g = 1$ .

### 7.3 Validation

Confidence in SMMC results requires numerical validation of the methods used. Separate issues are the validation of the SMMC formalism and algorithms, as developed in sections 3–6, and of the  $g$ -extrapolation required in calculations with realistic residual interactions

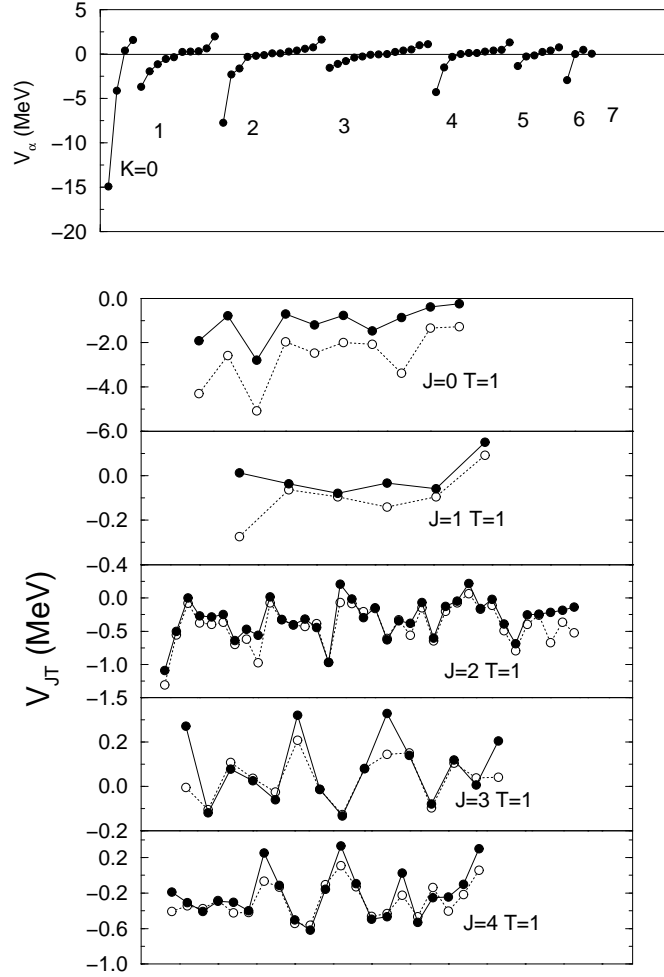


FIG 7.1. Decomposition of the Kuo-Brown KB3 interaction. The upper panel shows the eigenvalues  $V_\alpha$  for the various particle-hole angular momenta  $K$ . The lower panels show the particle-particle two-body matrix elements in selected  $JT$  channels. Solid symbols are the full hamiltonian, while open symbols correspond to  $\hat{H}_G$ .

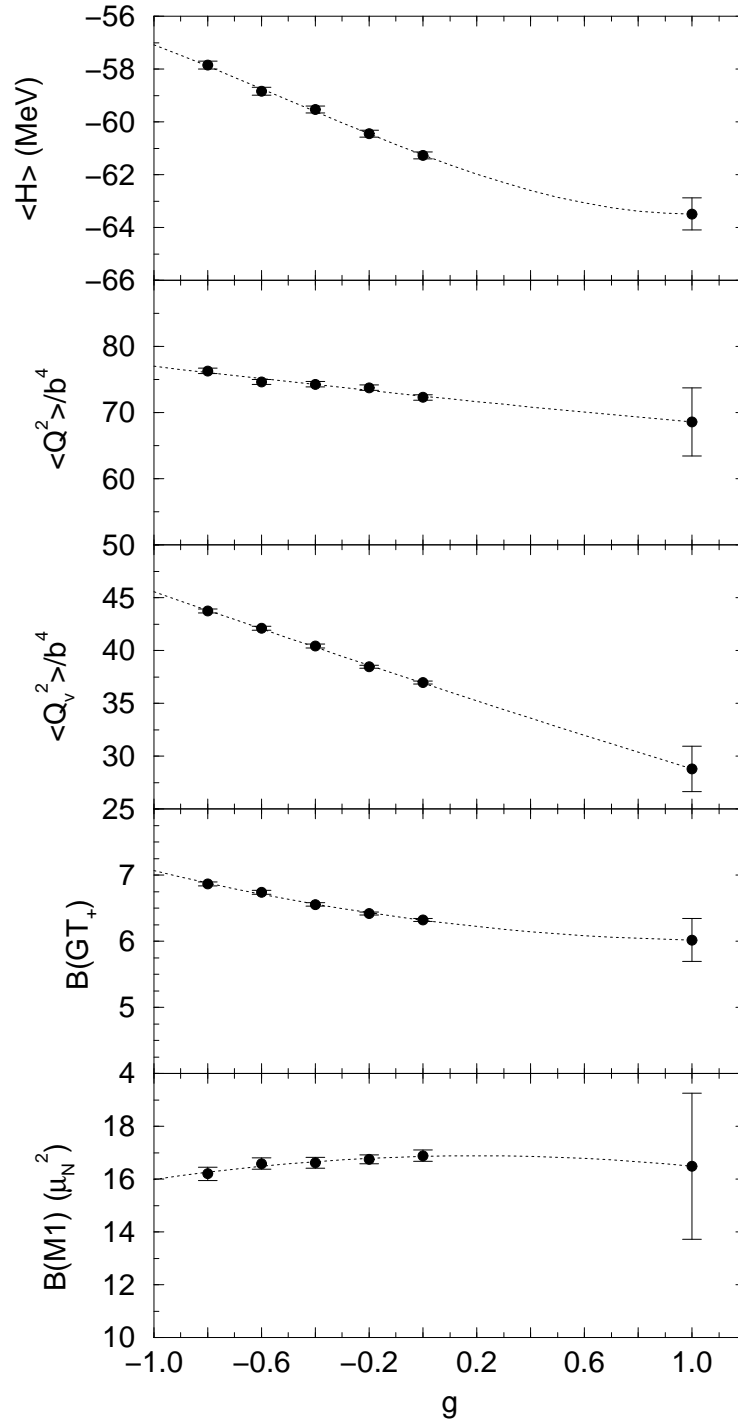


FIG 7.2.  $g$ -extrapolation of several observables for  $^{54}\text{Fe}$  calculated with the Kuo-Brown interaction KB3.

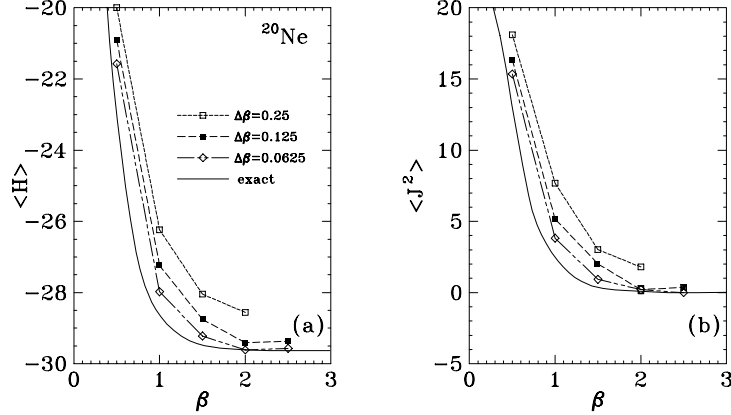


FIG 7.3. Comparison of SMMC results for selected observables with those obtained by conventional diagonalization [27]. The calculations have been performed for  $^{20}\text{Ne}$  within the  $sd$  model space. A pairing+quadrupole interaction, which is free from the sign problem discussed in section 7.2, has been used.

(see subsection 7.2).

Apart from demonstrating convergence in the various calculational parameters ( $\Delta\beta$ , number of samples, etc.), SMMC algorithms have been validated by comparison with direct diagonalization. Several examples of both the zero temperature and thermal SMMC formalisms are given in Refs. [26, 27]. These calculations have been performed for Hamiltonians possessing good sign properties (i.e. all  $V_\alpha \leq 0$ ). For ground state and thermal properties, as well as for strength distributions, excellent agreement between direct diagonalization and the SMMC methods has been demonstrated [27]. Some examples are summarized in Fig. 7.3.

The  $g$ -extrapolation has been tested for several nuclei in the  $sd$ -shell [29] and in the low  $pf$ -shell [55]. For example, using the parameter  $\chi = 4$  SMMC can reproduce [55] all observables (ground state energy, total  $B(E2)$ ,  $B(M1)$ , GT strength etc.) for those nuclei in the mass range  $A = 48 - 56$  for which direct diagonalization studies [51] or estimates on the basis of a series of truncation calculations [52] exist. An example for the nuclei  $^{54,56}\text{Fe}$  is given in Fig. 2.2.

The extrapolation procedure in thermal SMMC studies has been validated for  $^{44}\text{Ti}$  by comparison to a direct diagonalization calculation. The code CRUNCHER and the residual FPVH interaction were used to calculate the lowest 750 eigenstates up to an excitation energy of 43 MeV, which is sufficient to calculate the energy expectation value as a function of temperature up to  $T = 2$  MeV. We note that exact reproduction of the CRUNCHER results was obtained only after a  $\Delta\beta \rightarrow 0$  extrapolation which lowers the energies slightly compared to the calculation with finite  $\Delta\beta = 1/32 \text{ MeV}^{-1}$ . Fig. 7.4 compares the ( $\Delta\beta$ - and  $g$ -extrapolated) SMMC results with those obtained by direct diagonalization. Note that we cannot validate thermal properties requiring the calculation of transition matrix elements, as the latter are not numerically practical in direct diagonalization for thermal ensembles.

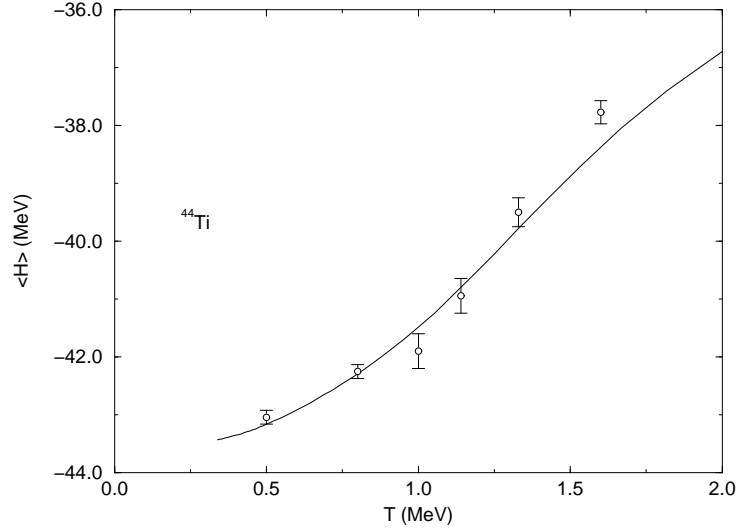


FIG 7.4. Comparison of SMMC results for the temperature dependence of the internal energy in  $^{44}\text{Ti}$  with those obtained by conventional diagonalization code CRUNCHER.

## 8 Selected results

The previous sections have outlined the motivation, formalism, implementation, and validation of Monte Carlo methods for treating the nuclear shell model. Of course, the ultimate goal of this work is to gain insight into the properties of real nuclei under a variety of conditions. In this section, we present a sampling of such results and their interpretation. The calculations presented should be viewed only as an indication of the power and potential of the method; undoubtedly, more work of this sort, abetted by ever-increasing computer power, will follow in the future.

### 8.1 Ground state properties of $pf$ -shell nuclei

While complete  $0\hbar\omega$  calculations can be carried out by direct diagonalization in the  $p$ - and  $sd$ -shells, the exponentially increasing number of configurations limits such studies in the next ( $pf$ ) shell to only the very lightest nuclei [38, 51]. SMMC techniques allow calculation of groundstate observables in the full  $0\hbar\omega$  model space for nuclei throughout the  $pf$ -shell. Here, we discuss a set of such calculations that use the modified KB3 interaction [19]; the single-particle basis is such that  $N_s = 20$  for both protons and neutrons. A more detailed description of the calculations and their results are found in Ref. [55].

These studies were performed for 28 even-even Ti, Cr, Fe, Ni, and Zn isotopes; extension to heavier nuclei is dubious because of the neglect of the  $g_{9/2}$  orbital. We have used  $\beta = 2 \text{ MeV}^{-1}$  with fixed  $\Delta\beta = 1/32 \text{ MeV}^{-1}$ ; test calculations at varying  $\beta$  show that the results accurately reflect the ground state properties. Some 4000-5000 independent Monte Carlo samples were taken for six equally-spaced values of  $g$  between  $-1$  and  $0$ , and observables were extrapolated to  $g = 1$  using linear or quadratic functions, as required. We chose the

parameter  $\chi = 4$ , as described in Section 7.2.

Figure 8.1 shows systematic results for the mass-defects, obtained directly from  $\langle \hat{H} \rangle$ . The SMMC results have been corrected for the Coulomb energy, which is not included in the KB3 interaction, using [51]

$$H_{\text{Coul}} = \frac{\pi(\pi - 1)}{2} \cdot 0.35 - \pi\nu 0.05 + \pi \cdot 7.289. \quad (8.1)$$

where  $\pi$  and  $\nu$  are the numbers of valence protons and neutrons, respectively, and the energy is in MeV. As in Ref. [51], we have increased the calculated energy expectation values by  $0.014 \cdot n(n-1)$  MeV (where  $n = \pi + \nu$  is the number of valence nucleons) to correct for a “tiny” residual monopole defect in the KB3 interaction. In general, there is excellent agreement; the average error for the nuclei shown is +0.45 MeV, which agrees roughly with the internal excitation energy of a few hundred keV expected in our finite-temperature calculation.

Figure 8.2 shows the calculated total  $E2$  strengths for selected  $pf$ -shell nuclei. This quantity is defined as

$$B(E2) = \langle (e_p \hat{Q}_p + e_n \hat{Q}_n)^2 \rangle, \quad (8.2)$$

with

$$\hat{Q}_{p(n)} = \sum_i r_i^2 Y_2(\theta_i, \phi_i), \quad (8.3)$$

where the sum runs over all valence protons (neutrons). The effective charges were chosen to be  $e_p = 1.35$  and  $e_n = 0.35$ , while we used  $b = 1.01A^{1/6}$  fm for the oscillator length. Shown for comparison are the  $B(E2)$  values for the  $0_1^+ \rightarrow 2_1^+$  transition in each nucleus; in even-even nuclei some 20-30% of the strength comes from higher transitions. The overall trend is well reproduced, For the nickel isotopes  $^{58,60,64}\text{Ni}$ , the total  $B(E2)$  strength is known from  $(e, e')$  data and agrees very nicely with our SMMC results.

The Gamow-Teller (GT) properties of nuclei in this region of the periodic table are crucial for supernova physics [11]. These strengths are defined as

$$B(GT_{\pm}) = \langle (\vec{\sigma}\tau_{\pm})^2 \rangle. \quad (8.4)$$

Note that the Ikeda sum rule,  $B(GT_-) - B(GT_+) = 3(N - Z)$  is satisfied exactly by our calculations. In Figure 8.3, we show the calculated  $B(GT_+)$  for all  $pf$ -shell nuclei for which this quantity has been measured by  $(n, p)$  reactions. (For the odd nuclei  $^{51}\text{V}$ ,  $^{55}\text{Mn}$  and  $^{59}\text{Co}$  the SMMC calculations have been performed at  $\beta = 1$  MeV $^{-1}$  to avoid the odd- $A$  sign problem. For even-even nuclei the GT strength calculated at this temperature is still a good approximation for the ground state value, as is shown below). Since the experimental values are normalized to measured  $\beta$ -decay  $ft$  values, and it is believed that the axial coupling constant is renormalized from its free value ( $g_A = 1.26$ ) to  $g_A = 1$  in nuclei [21, 51], we have multiplied all calculated results by  $(1/1.26)^2$ . Note that this results in generally excellent agreement between the calculations and the data. Thus, we support both the statement that  $g_A$  is quenched to 1 in nuclei and the statement that complete shell-model calculations can account for the GT strength observed experimentally. Note that the quenching of  $g_A$  in the nuclear medium is not quite understood yet. It is believed to be related either to a second-order core polarization caused by the tensor force [68] or to the screening of the Gamow-Teller operator by  $\Delta$ -hole pairs [69]

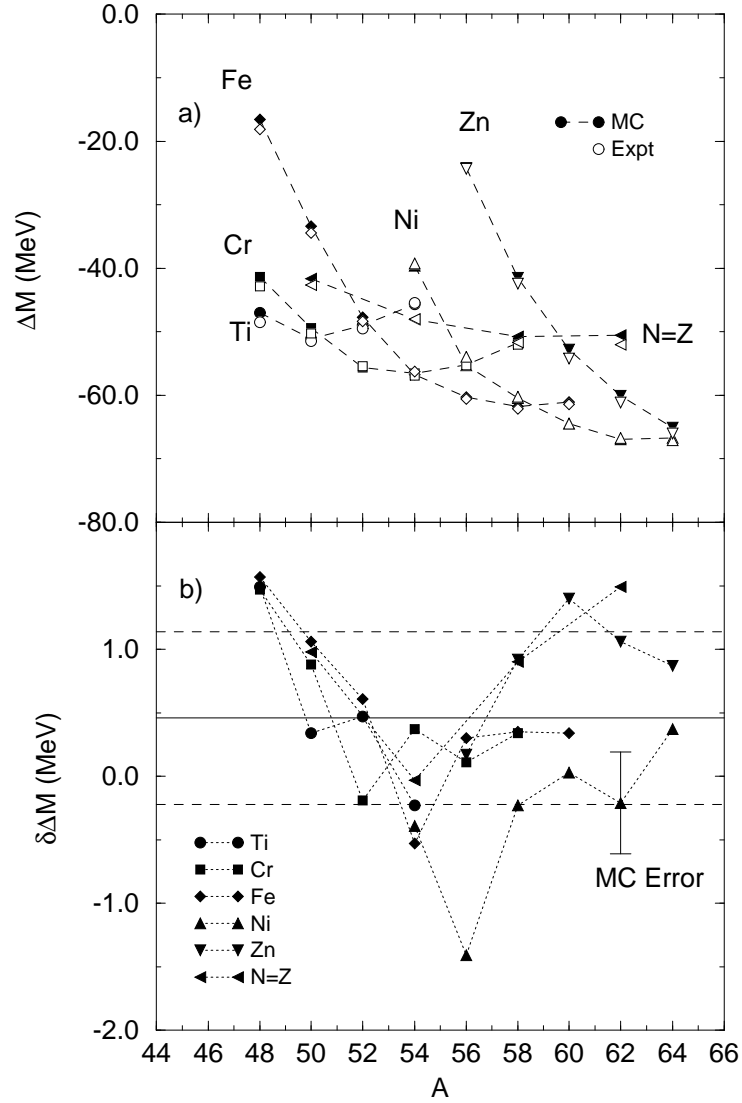


FIG 8.1. Upper panel (a): Comparison of the mass excesses  $\Delta M$  as calculated within the SMMC approach with data. Lower panel (b): Discrepancy between the SMMC results for the mass excesses and the data,  $\delta\Delta M$ . The solid line shows the average discrepancy, 450 keV, while the dashed lines show the rms variation about this value (from [55]).

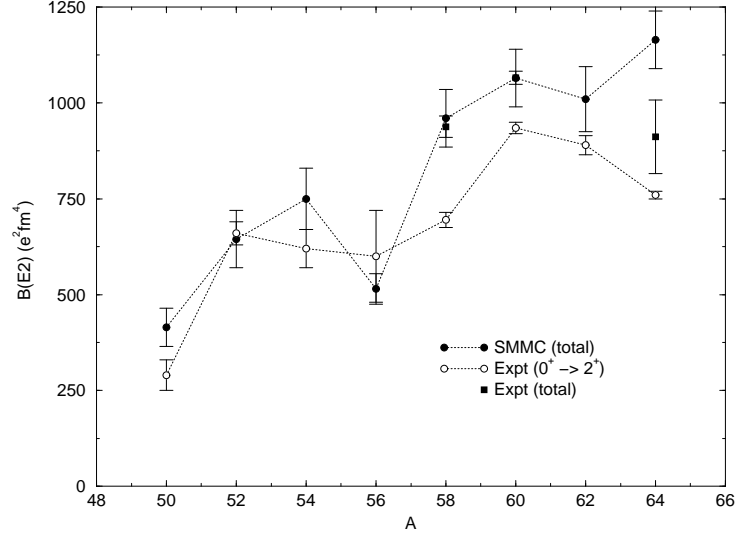


FIG 8.2. Comparison of the experimental  $B(E2, 0_1^+ \rightarrow 2_1^+)$  strengths with the total  $B(E2)$  strength calculated in the SMMC approach for various  $pf$ -shell nuclei having either proton or neutron number of 28. For the nickel isotopes  $^{58,60,64}\text{Ni}$  the total  $B(E2)$  strength (full squares) is known from inelastic electron scattering data (from [55]).

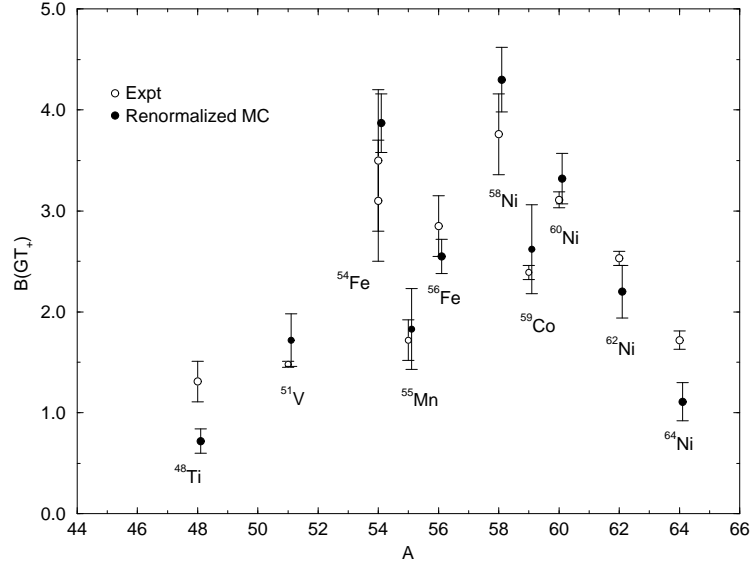


FIG 8.3. Comparison of the renormalized total Gamow-Teller strength, as calculated within the present SMMC approach, and the experimental  $B(GT_+)$  values deduced from  $(n, p)$  data [62]-[66].

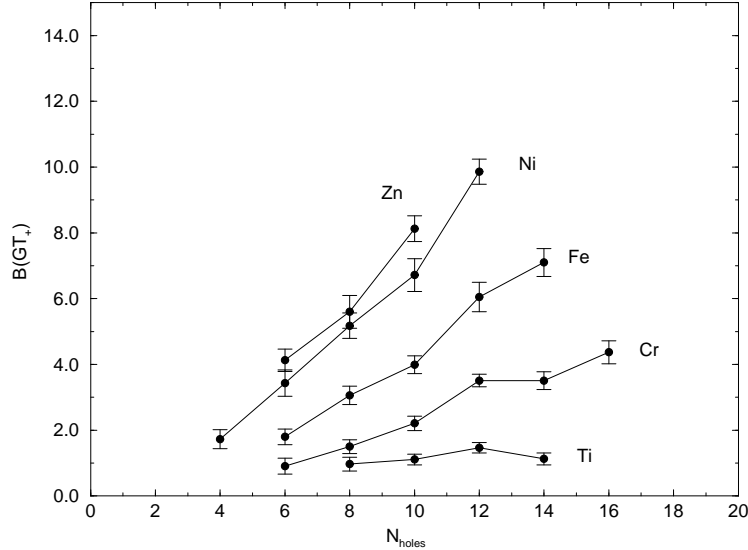


FIG 8.4. Unrenormalized total Gamow-Teller strengths for various isotope chains as a function of neutron holes ( $N_{\text{val}} - 20$ ) in the  $pf$ -shell (from [55]).

The calculated systematics of the  $B(GT_+)$  strength for isotope chains throughout this region are shown in Figure 8.4, where it can be seen that  $GT_+$  increases as the number of valence neutron holes increases (unblocking), and as the number of valence protons increases. These systematics were summarized phenomenologically from the experimental data in Ref. [67] as

$$B(GT_+) = 0.045 \cdot Z_{\text{val}} \cdot (20 - N_{\text{val}}), \quad (8.5)$$

which is derived by assuming that the residual interaction is strong enough to destroy all sub-shell structure, so that the entire  $pf$ -shell behaves as one large orbital. Figure 8.5 shows the linearity of  $B(GT_+)/Z$  with  $(N_{\text{val}} - 20)$  for the experimental data.

The magnetic dipole strengths are defined as

$$B(M1) = \langle (\sum_i \mu_N \{g_l \vec{l} + g_s \vec{s}\})^2 \rangle. \quad (8.6)$$

where  $\mu_N$  is the nuclear magneton and  $g_l, g_s$  are the free gyromagnetic ratios for angular momentum and spin, respectively ( $g_l = 1, g_s = 5.586$  for protons, and  $g_l = 0, g_s = -3.826$  for neutrons). A complete list of the total  $B(M1)$  strengths as calculated in SMMC studies of  $pf$ -shell nuclei is given in Ref. [55].

Brown and Wildenthal [21] suggested that, as a general rule, the strength of spin operators is renormalized in nuclei. To account for this renormalization, it is customary to use effective gyromagnetic ratios for the spin,  $\tilde{g}_s = g_s/1.26$  in shell model calculations [21, 51]. If we follow this prescription, we calculate total  $B(M1)$  strengths for the  $N = 28$  isotones (in units of  $\mu_N^2$ ) of  $7.9 \pm 0.7$  ( $^{50}\text{Ti}$ ),  $11.7 \pm 1.5$  ( $^{52}\text{Cr}$ ), and  $10.2 \pm 2$  ( $^{54}\text{Fe}$ ). For these nuclei, Richter and collaborators [70] have used high-resolution electron scattering to study the  $B(M1)$  strength in an energy window large enough to contain most of the strength. They find  $B(M1) = 4.5 \pm 0.5$  ( $^{50}\text{Ti}$ ),  $8.1 \pm 0.8$  ( $^{52}\text{Cr}$ ) and  $6.6 \pm 0.4$  ( $^{54}\text{Fe}$ ) for excitation energies

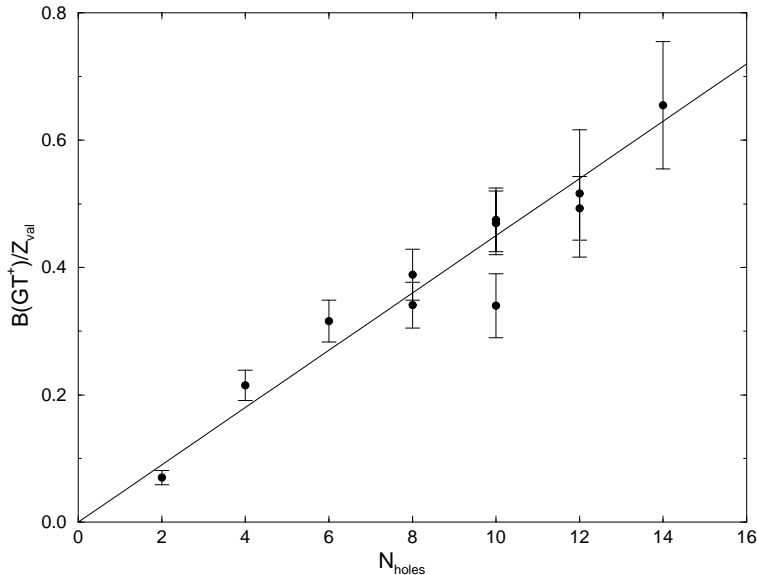


FIG 8.5. Experimental total Gamow-Teller strengths [62]-[66], divided by the number of valence protons, as a function of neutron holes in the  $pf$ -shell.

between 7 and 12 MeV [70]. If one considers that this energy window should contain about 75% of the total strength [70], our SMMC results appear to be consistent with the data.

## 8.2 Pair structure of the nuclear ground state

Numerous phenomenological descriptions of nuclear collective motion describe the nuclear ground state and its low-lying excitations in terms of bosons. In one such model, the Interacting Boson Model (IBM),  $L = 0$  (S) and  $L = 2$  (D) bosons are identified with nucleon pairs having the same quantum numbers [13], and the ground state can be viewed as a condensate of such pairs. Shell model studies of the pair structure of the ground state and its variation with the number of valence nucleons can therefore shed light on the validity and microscopic foundations of these boson approaches.

For many purposes, it appears sufficient to study the BCS pair structure in the ground state. The BCS pair operator for protons can be defined as

$$\hat{\Delta}_p^\dagger = \sum_{jm>0} p_{jm}^\dagger p_{j\bar{m}}^\dagger, \quad (8.7)$$

where the sum is over all orbitals with  $m > 0$  and  $p_{j\bar{m}}^\dagger = (-)^{j-m} p_{jm}^\dagger$  is the time-reversed operator. Thus, the observable  $\hat{\Delta}^\dagger \hat{\Delta}$  and its analog for neutrons are measures of the numbers of  $J = 0, T = 1$  pairs in the groundstate. For an uncorrelated Fermi gas, we have simply

$$\langle \hat{\Delta}^\dagger \hat{\Delta} \rangle = \sum_j \frac{n_j^2}{2(2j+1)}, \quad (8.8)$$

where the  $n_j = \langle p_{jm}^\dagger p_{jm} \rangle$  are the occupation numbers, so that any excess of  $\langle \hat{\Delta}^\dagger \hat{\Delta} \rangle$  in our SMMC calculations over the Fermi-gas value indicates pairing correlations in the ground-state.

Fig. 8.6 shows the SMMC expectation values of the proton and neutron BCS-like pairs, obtained after subtraction of the Fermi gas value (8.8), for three chains of isotopes. As expected, these excess pair correlations are quite strong and reflect the well-known coherence in the ground states of even-even nuclei. Note that the proton BCS-like pairing fields are not constant within an isotope chain, showing that there are important proton-neutron correlations present in the ground state. The shell closure at  $N = 28$  is manifest in the neutron BCS-like pairing. As is demonstrated in Fig. 8.7, the proton and neutron occupation numbers show a much smoother behavior with increasing  $A$ .

It should be noted that the BCS form (8.7) in which all time-reversed pairs have equal amplitude is not necessarily the optimal one and allows only the study of S-pair structure. To explore the pair content of the ground state in a more general way, we define proton pair creation operators

$$\hat{A}_{J\mu}^\dagger(j_a j_b) = \frac{1}{\sqrt{1 + \delta_{ab}}} [a_{j_a}^\dagger \times a_{j_b}^\dagger]_{J\mu} . \quad (8.9)$$

These operators are boson-like in the sense that

$$[\hat{A}_{J\mu}^\dagger(j_a j_b), \hat{A}_{J\mu}(j_a j_b)] = 1 + \mathcal{O}(\hat{n}/2j + 1) ; \quad (8.10)$$

i.e., they satisfy the expected commutation relations in the limit of an empty shell.

We construct bosons  $\hat{B}_{\alpha J\mu}^\dagger$  as

$$\hat{B}_{\alpha J\mu}^\dagger = \sum_{j_a j_b} \psi_{\alpha\lambda}(j_a j_b) \hat{A}_{\lambda\mu}^\dagger(j_a j_b) , \quad (8.11)$$

where  $\alpha = 1, 2, \dots$  labels the particular boson and the “wave function”  $\psi$  satisfies

$$\sum_{j_a j_b} \psi_{\alpha J}^*(j_a j_b) \psi_{\beta J}(j_a j_b) = \delta_{\alpha\beta} . \quad (8.12)$$

(Note that  $\psi$  is independent of  $\mu$  by rotational invariance.)

To find  $\psi$  and  $n_{\alpha J} \equiv \sum_\mu \langle \hat{B}_{\alpha J\mu}^\dagger \hat{B}_{\alpha J\mu} \rangle$ , the number of bosons of type  $\alpha$  and multipolarity  $J$ , we compute the quantity  $\sum_\mu \langle \hat{A}_{J\mu}^\dagger(j_a j_b) \hat{A}_{J\mu}(j_c j_d) \rangle$ , which can be thought of as an hermitian matrix  $M_{\alpha\alpha'}^J$  in the space of orbital pairs  $(j_a j_b)$ ; its non-negative eigenvalues define the  $n_{\alpha J}$  (we order them so that  $n_{1J} > n_{2J} > \dots$ ), while the normalized eigenvectors are the  $\psi_{\alpha J}(j_a j_b)$ . The index  $\alpha$  distinguishes the various possible bosons. For example, in the complete  $pf$ -shell the square matrix  $M$  has dimension  $N_J = 4$  for  $J = 0$ ,  $N_J = 10$  for  $J = 1$ ,  $N_J = 13$  for  $J = 2, 3$ .

The presence of a pair condensate in a correlated ground state will be signaled by the largest eigenvalue for a given  $J$ ,  $n_{1J}$ , being much greater than any of the others;  $\psi_{1J}$  will then be the condensate wavefunction. In Fig. 8.8 we show the pair matrix eigenvalues  $n_{\alpha J}$  for the three isovector  $J = 0^+$  pairing channels as calculated for the iron isotopes  $^{54-58}\text{Fe}$ . We compare the SMMC results with those of an uncorrelated Fermi gas, where we can compute  $\langle \hat{A}^\dagger \hat{A} \rangle$  using the factorization

$$\langle a_\alpha^\dagger a_\beta^\dagger a_\gamma a_\delta \rangle = n_\beta n_\alpha (\delta_{\beta\gamma} \delta_{\alpha\delta} - \delta_{\beta\delta} \delta_{\alpha\gamma}) , \quad (8.13)$$

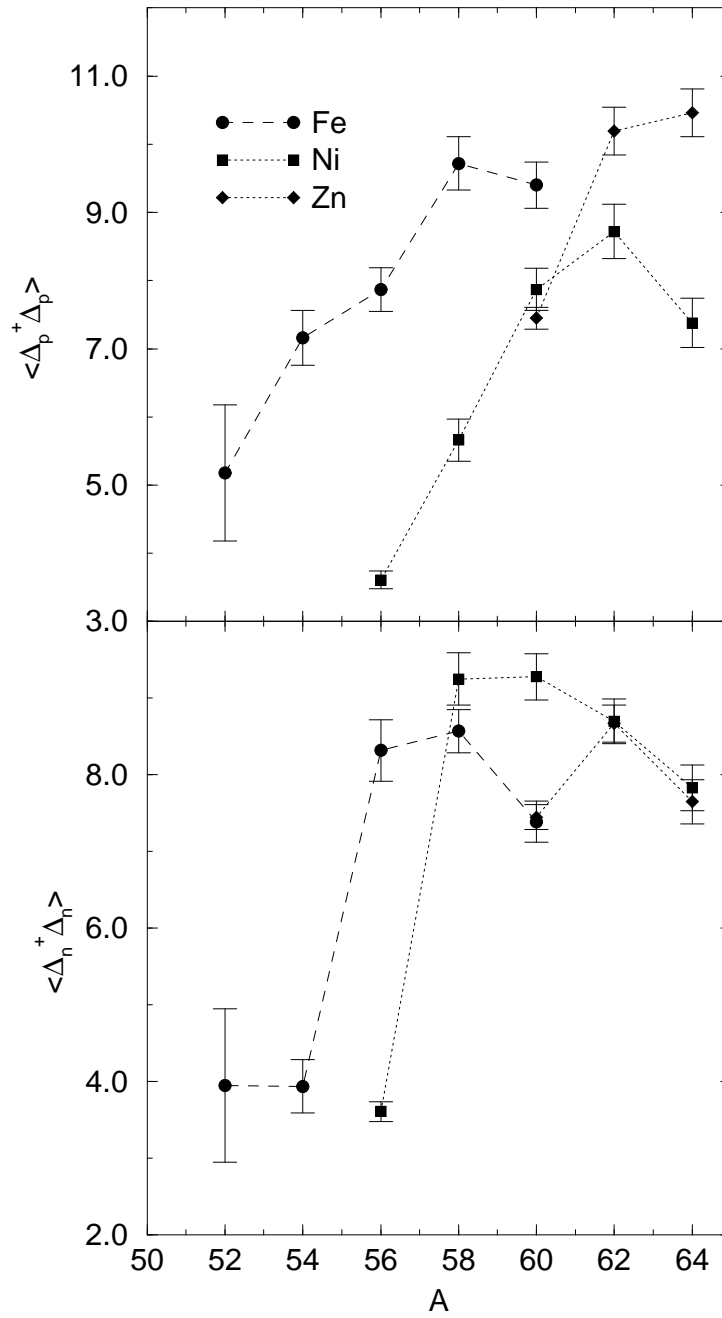


FIG 8.6. SMMC expectation values of proton and neutron BCS-like pairs after subtraction of the Fermi gas value (from [55]).

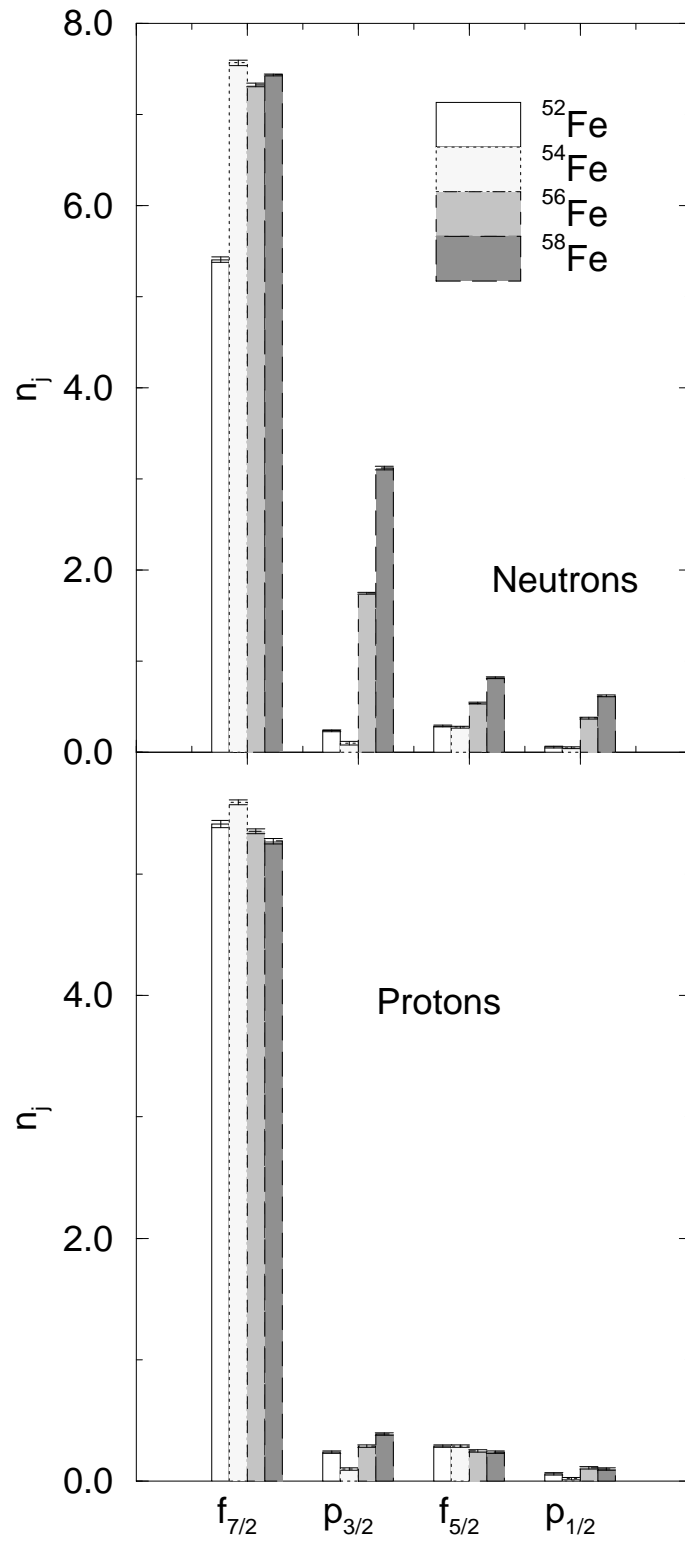


FIG 8.7. Proton and neutron occupation numbers for various chains of isotopes (from [55]).

where the  $n_\beta = \langle a_\beta^\dagger a_\beta \rangle$  are the occupation numbers. Additionally, Fig. 8.8 shows the diagonal matrix elements of the pair matrix  $M_{\alpha\alpha}$ . As expected, the protons occupy mainly  $f_{7/2}$  orbitals in these nuclei. Correspondingly, the  $\langle \hat{A}^\dagger \hat{A} \rangle$  expectation value is large for this orbital and small otherwise. For neutrons, the pair matrix is also largest for the  $f_{7/2}$  orbital. The excess neutrons in  $^{56,58}\text{Fe}$  occupy the  $p_{3/2}$  orbital, signalled by a strong increase of the corresponding pair matrix element  $M_{22}$  in comparison to its value for  $^{54}\text{Fe}$ . Upon closer inspection we find that the proton pair matrix elements are not constant within the isotope chain. This behavior is mainly caused by the isoscalar proton-neutron pairing. The dominant role is played by the isoscalar  $1^+$  channel, which couples protons and neutrons in the same orbitals and in spin-orbit partners. As a consequence we find that, for  $^{54,56}\text{Fe}$ , the proton pair matrix in the  $f_{5/2}$  orbital,  $M_{33}$ , is larger than in the  $p_{3/2}$  orbital, although the latter is favored in energy. For  $^{58}\text{Fe}$ , this ordering is inverted, as the increasing number of neutrons in the  $p_{3/2}$  orbital increases the proton pairing in that orbital.

After diagonalization of  $M$ , the  $J = 0$  proton pairing strength is essentially found in one large eigenvalue. Furthermore we observe that this eigenvalue is significantly larger than the largest eigenvalue on the mean-field level (Fermi gas), supporting the existence of a proton pair condensate in the ground state of these nuclei. The situation is somewhat different for neutrons. For  $^{54}\text{Fe}$  only little additional coherence is found beyond the mean-field value, reflecting the closed-subshell neutron structure. For the two other isotopes, the neutron pairing exhibits two large eigenvalues. Although the larger one exceeds the mean-field value and signals noticeable additional coherence across the subshells, the existence of a second coherent eigenvalue shows the shortcomings of the BCS-like pairing picture.

It has long been anticipated that  $J = 0^+$  proton-neutron correlations play an important role in the ground states of  $N = Z$  nuclei. To explore these correlations we have performed SMMC calculations of the  $N = Z$  nuclei in the mass region  $A = 48 - 56$ . Note that for these nuclei the pair matrix in all three isovector  $0^+$  channels essentially exhibits only one large eigenvalue, related to the  $f_{7/2}$  orbital. We will use this eigenvalue as a convenient measure of the pairing strength. As the even-even  $N = Z$  nuclei have isospin  $T = 0$ , the expectation values of  $\hat{A}^\dagger \hat{A}$  are identical in all three isovector  $0^+$  pairing channels. This symmetry does not hold for the odd-odd  $N = Z$  nuclei in this mass range, which have  $T = 1$  ground states, and  $\langle \hat{A}^\dagger \hat{A} \rangle$  can be different for proton-neutron pairs than for like-nucleons pair (the expectation values for proton pairs and neutron pairs are identical). We find the proton-neutron pairing strength significantly larger for odd-odd  $N = Z$  nuclei than in even-even nuclei, while the  $0^+$  proton and neutron pairing shows the opposite behavior, in both cases leading to an odd-even staggering, as displayed in Fig. 8.9. This staggering is caused by a constructive interference of the isotensor and isoscalar parts of  $\hat{A}^\dagger \hat{A}$  in the odd-odd  $N = Z$  nuclei, while they interfere destructively in the even-even nuclei. The isoscalar part is related to the pairing energy, and is found to be about constant for the nuclei studied here.

### 8.3 Thermal properties of $pf$ -shell nuclei

The properties of nuclei at finite temperatures are of considerable experimental [71, 72] and theoretical interest [73, 74]. They are clearly quite important in various astrophysical scenarios. For example, electron capture on nuclei plays an essential role in the early presupernova collapse [11]. In that context, it is important to know the temperature dependence of the

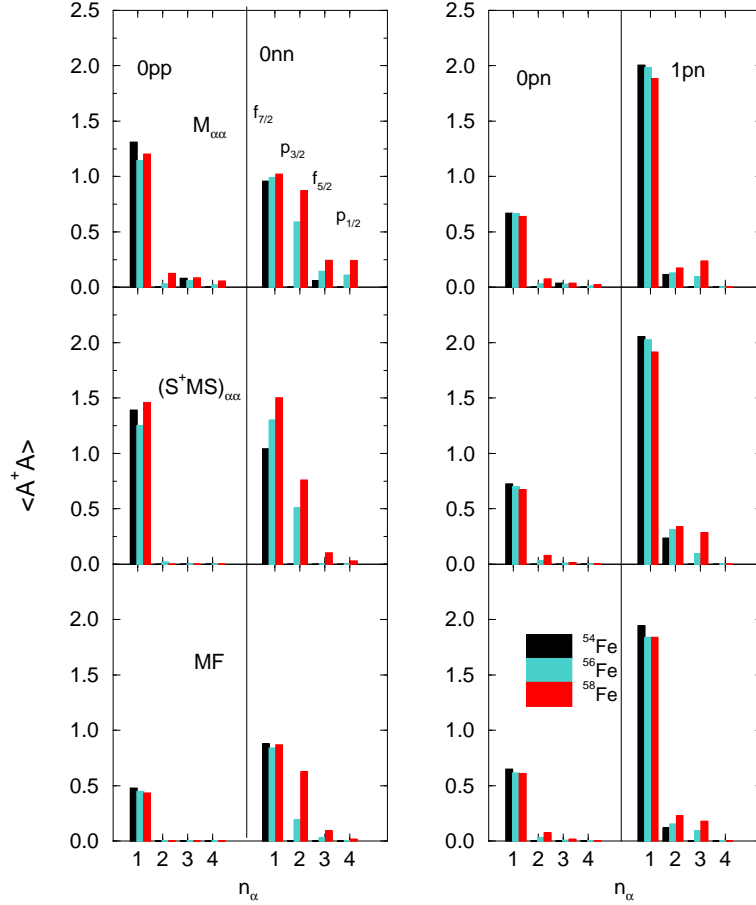


FIG 8.8. Content of isovector  $0^+$  pairs and isoscalar  $1^+$  pairs in the ground states of the isotopes  $^{54-58}\text{Fe}$ . The upper panel shows the diagonal matrix elements of the pair matrix  $M_{\alpha\alpha}$ . The index  $\alpha = 1, \dots, 4$  refers to  $0^+$  pairs in the  $f_{7/2}$ ,  $p_{3/2}$ ,  $f_{5/2}$ , and  $p_{1/2}$  orbitals, respectively. For the isoscalar pairs  $\alpha = 1, 2, 3$  refers to  $(f_{7/2})^2$ ,  $(f_{7/2}f_{5/2})$  and  $(f_{5/2})^2$  pairs, respectively. The middle panel gives the eigenvalues of the pair matrix; for the isoscalar pairs only the 3 largest are shown. The lower panel gives the eigenvalues of the pair matrix for the uncorrelated Fermi gas case using Eq. (8.13) (from [77]).

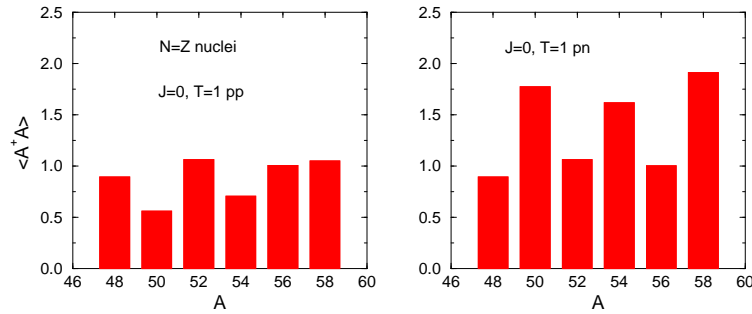


FIG 8.9. Largest eigenvalue for the various isovector  $0^+$  pairs in the  $N = Z$  nuclei in the mass region  $A = 48 - 56$ .

Gamow-Teller strength.

Theoretical studies of nuclei at finite temperature have been based mainly on mean-field approaches, and thus only consider the temperature dependence of the most probable configuration in a given system. These approaches have been criticized due to their neglect of quantum and statistical fluctuations [75]. The SMMC method does not suffer this defect and allows the consideration of model spaces large enough to account for the relevant nucleon-nucleon correlations at low and moderate temperatures.

We have performed SMMC calculations of the thermal properties of several even-even nuclei in the mass region  $A = 50 - 60$  [76, 77]. As a typical example, we discuss in the following our SMMC results for the nucleus  $^{54}\text{Fe}$ , which is very abundant in the presupernova core of a massive star.

Our calculations include the complete set of  $1p_{3/2,1/2}0f_{7/2,5/2}$  states interacting through the realistic Brown-Richter Hamiltonian [38]. (SMMC calculations using the modified KB3 interaction give essentially the same results.) Some  $5 \times 10^9$  configurations of the 8 valence neutrons and 6 valence protons moving in these 20 orbitals are involved in the canonical ensemble. The results presented below have been obtained with a time step of  $\Delta\beta = 1/32 \text{ MeV}^{-1}$  using 5000–9000 independent Monte Carlo samples at seven values of the coupling constant  $g$  spaced between  $-1$  and  $0$  and the value  $\chi = 4$ .

The calculated temperature dependence of various observables is shown in Fig. 8.10. In accord with general thermodynamic principles, the internal energy  $U$  steadily increases with increasing temperature [76]. It shows an inflection point around  $T \approx 1.1 \text{ MeV}$ , leading to a peak in the heat capacity,  $C \equiv dU/dT$ , whose physical origin we will discuss below. The decrease in  $C$  for  $T \gtrsim 1.4 \text{ MeV}$  is due to our finite model space (the Schottky effect [78]); we estimate that limitation of the model space to only the  $pf$ -shell renders our calculations of  $^{54}\text{Fe}$  quantitatively unreliable for temperatures above this value (internal energies  $U \gtrsim 15 \text{ MeV}$ ). The same behavior is apparent in the level density parameter,  $a \equiv C/2T$ . The empirical value for  $a$  is  $A/8 \text{ MeV} = 6.8 \text{ MeV}^{-1}$  which is in good agreement with our results for  $T \approx 1.1\text{--}1.5 \text{ MeV}$ .

We also show in Fig. 8.10 the expectation values of the BCS-like proton-proton and neutron-neutron pairing fields,  $\langle \hat{\Delta}^\dagger \hat{\Delta} \rangle$ . At low temperatures, the pairing fields are significantly larger than those calculated for a non-interacting Fermi gas, indicating a strong coherence in the ground state. With increasing temperature, the pairing fields decrease, and both approach the Fermi gas values for  $T \approx 1.5 \text{ MeV}$  and follow it closely for even higher temperatures. Associated with the breaking of pairs is a dramatic increase in the moment of inertia,  $I \equiv \langle J^2 \rangle / 3T$ , for  $T = 1.0\text{--}1.5 \text{ MeV}$ ; this is analogous to the rapid increase in magnetic susceptibility in a superconductor. At temperatures above  $1.5 \text{ MeV}$ ,  $I$  is in agreement with the rigid rotor value,  $10.7\hbar^2/\text{MeV}$ ; at even higher temperatures it decreases linearly due to our finite model space.

In Fig. 8.11, we show various static observables. The  $M1$  strength unquenches rapidly with heating near the transition temperature. However, for  $T = 1.3\text{--}2 \text{ MeV}$   $B(M1)$  remains significantly lower than the single-particle estimate ( $41 \mu_N^2$ ), suggesting a persistent quenching at temperatures above the like-nucleon depairing. This finding is supported by the near-constancy of the Gamow-Teller  $\beta^+$  strength,  $B(\text{GT}_+)$ , for temperatures up to  $2 \text{ MeV}$ . As the results of Ref. [77] demonstrate that neutron-proton correlations are responsible for much of the GT quenching in iron nuclei at zero temperature, we interpret the present re-

sults as evidence that isovector proton-neutron correlations persist to higher temperatures (see below). We have verified that, in our restricted model space, both the  $GT_+$  and  $M1$  strengths unquench at temperatures above 2 MeV and that, in the high-temperature limit, they both approach the appropriate Fermi gas values. We note that it is often assumed in astrophysical calculations that the  $GT$  strength is independent of temperature [79]; our calculations demonstrate that this is true for the relevant temperature regime ( $T < 2$  MeV). We also note that a detailed examination of the occupation numbers of the various orbitals show no unusual variation as the pairing vanishes.

Although the results discussed above are typical for even-even nuclei in this mass region (including the  $N = Z$  nucleus  $^{52}\text{Fe}$ ), they are not for odd-odd  $N = Z$  nuclei. This is illustrated in Fig. 8.12 which shows the thermal behavior of several observables for  $^{50}\text{Mn}$  ( $N = Z = 25$ ), calculated in a SMMC study within the complete  $pf$ -shell using the KB3 interaction. In contrast to even-even nuclei, the total Gamow-Teller strength is not constant at low temperatures, but increases by about 50% between  $T = 0.4$  MeV and 1 MeV. The  $B(M1)$  strength decreases significantly in the same temperature interval, while for even-even nuclei, it increases steadily. A closer inspection of the isovector  $J = 0$  and isoscalar  $J = 1$  pairing correlations holds the key to the understanding of these differences. The  $J = 0$  isovector correlations are studied using the BCS pair operators (8.6), with a similar definition for proton-neutron pairing. For the isoscalar  $J = 1$  correlations we have interpreted the trace of the pair matrix  $M^{J=1}$  as an overall measure for the pairing strength,

$$P_{sm}^J = \sum_{\beta} \lambda_{\beta}^J = \sum_{\alpha} M_{\alpha\alpha}^J. \quad (8.14)$$

Note that at the level of the non-interacting Fermi gas, proton-proton, neutron-neutron and proton-neutron  $J = 0$  correlations are identical for  $N = Z$  nuclei. However, the residual interaction breaks the symmetry between like-pair correlations and proton-neutron correlations in odd-odd  $N = Z$  nuclei. As is obvious from Fig. 8.12, at low temperatures proton-neutron pairing dominates in  $^{50}\text{Mn}$ , while pairing among like nucleons shows only a small excess over the Fermi gas values, in strong contrast to even-even nuclei.

A striking feature of Fig. 8.12 is that the isovector proton-neutron correlations decrease strongly with temperature and have essentially vanished at  $T = 1$  MeV, while the isoscalar pairing strength remains about constant in this temperature region (as it does in even-even nuclei) and greatly exceeds the Fermi gas values. We also note that the pairing between like nucleons is roughly constant at  $T < 1$  MeV. The change of importance between isovector and isoscalar proton-neutron correlations with temperature is nicely reflected in the isospin expectation value, which decreases from  $\langle \hat{T}^2 \rangle = 2$  at temperatures around 0.5 MeV, corresponding to the dominance of isovector correlations, to  $\langle \hat{T}^2 \rangle = 0$  at temperature  $T = 1$  MeV, when isoscalar proton-neutron correlations are most important. The low-temperature behavior of the Gamow-Teller and  $B(M1)$  strength is related to the fading of the isoscalar proton-neutron correlations. For example, the Gamow-Teller strength increases as transitions between the same orbital (mainly  $f_{7/2}$ ) are less quenched by weaker isovector proton-neutron correlations.

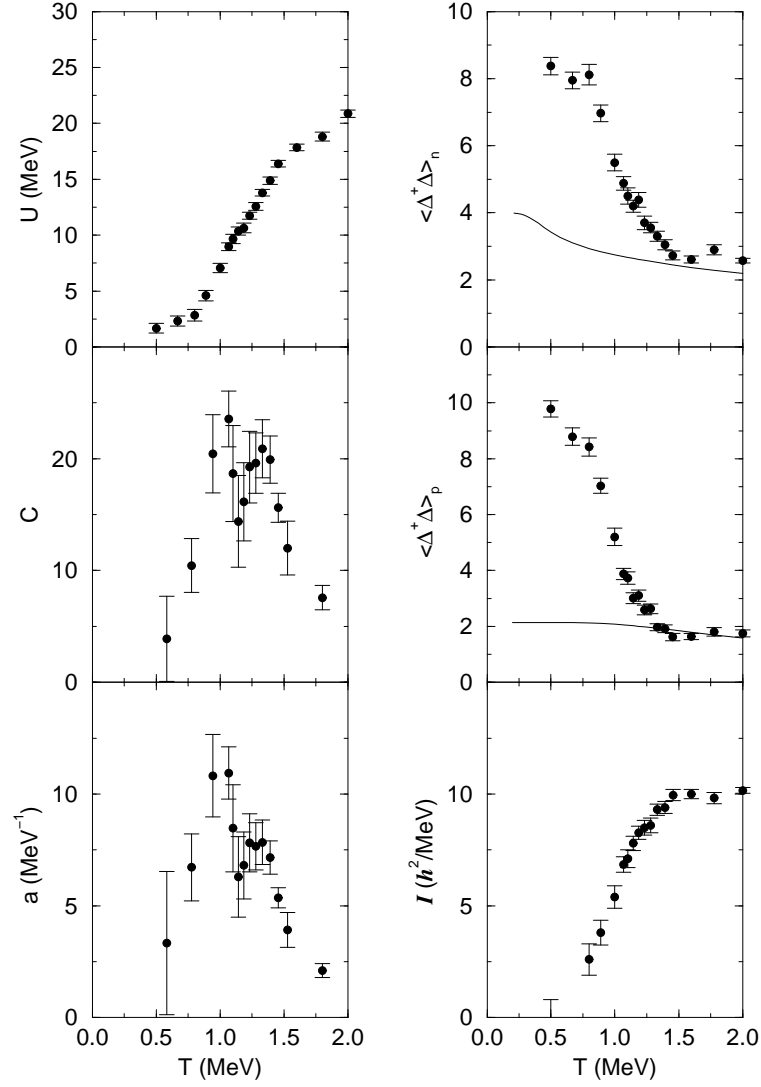


FIG 8.10. Temperature dependence of various observables in  $^{54}\text{Fe}$ . Monte Carlo points with statistical errors are shown at each temperature  $T$ . In the left-hand column, the internal energy,  $U$ , is calculated as  $\langle \hat{H} \rangle - E_0$ , where  $\hat{H}$  is the many-body Hamiltonian and  $E_0$  the ground state energy. The heat capacity  $C$  is calculated by a finite-difference approximation to  $dU/dT$ , after  $U(T)$  has been subjected to a three-point smoothing, and the level density parameter is  $a \equiv C/2T$ . In the right-hand column, we show the expectation values of the squares of the proton and neutron BCS pairing fields. For comparison, the pairing fields calculated in an uncorrelated Fermi gas are shown by the solid curve. The moment of inertia is obtained from the expectation values of the square of the total angular momentum by  $I = \beta \langle \hat{J}^2 \rangle / 3$  (from [76]).

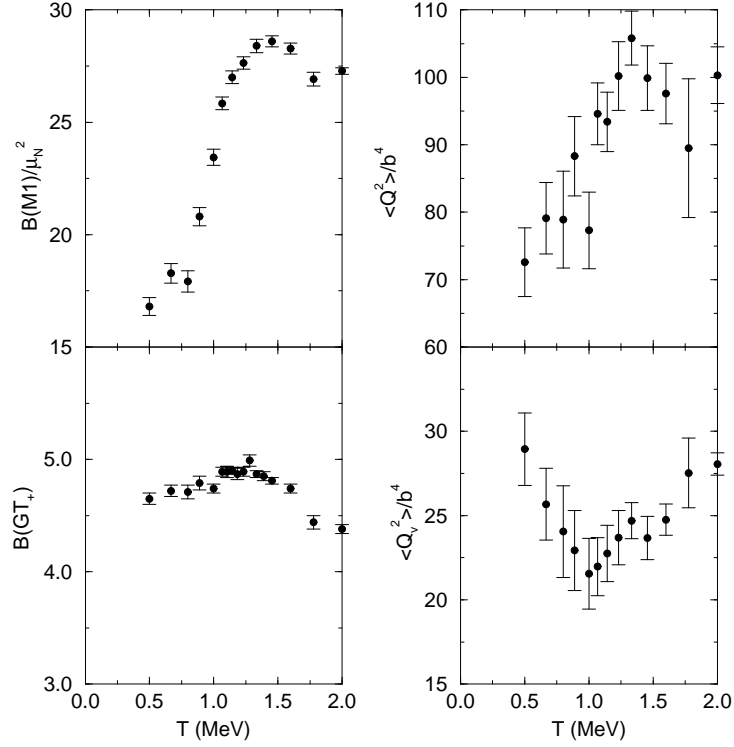


FIG 8.11. The upper left panel shows, for  $^{54}\text{Fe}$ , the total magnetic dipole strength,  $B(M1)$  in units of nuclear magnetons; it is calculated using free-nucleon  $g$ -factors. The lower left panel shows the GT  $\beta_+$  strength, while the upper and lower right panels show the isoscalar ( $\hat{Q} = \hat{Q}_p + \hat{Q}_n$ ) and isovector ( $\hat{Q}_v = \hat{Q}_p - \hat{Q}_n$ ) quadrupole strengths. In these latter observables, the quadrupole operators are  $r^2 Y_2$ , and results are given in terms of the oscillator length,  $b = 1.96$  fm (from [76]).

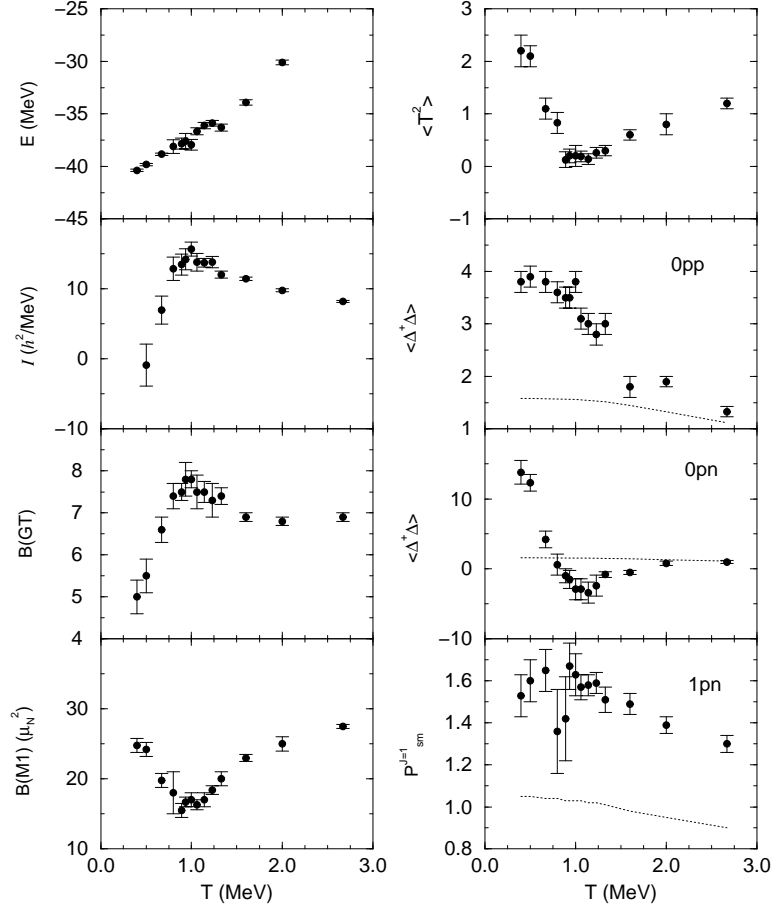


FIG 8.12 Temperature dependence of various observables in  $^{50}\text{Mn}$ . The left panels show (from top to bottom) the total energy, the moment of inertia, the  $B(M1)$  strength, and the Gamow-Teller strength, while the right panels exhibit the expectation values of the isospin operator  $\langle \hat{T}^2 \rangle$ , the isovector  $J = 0$  proton-proton and proton-neutron BCS pairing fields, and the isoscalar  $J = 1$  pairing strength, as defined in the text. For comparison, the solid lines indicate the Fermi gas values of the BCS pairing fields and  $J = 1$  pairing strength.

## 8.4 Pair correlations and thermal response

All SMMC calculations of even-even nuclei in the mass region  $A = 50 - 60$  show that the BCS-like pairs break at temperatures around 1 MeV. Three observables exhibit a particularly interesting behavior at this phase transition: a) the moment of inertia rises sharply; b) the M1 strength shows a sharp rise, but unquenches only partially; and c) the Gamow-Teller strength remains roughly constant (and strongly quenched). Note that the  $B(M1)$  and  $B(GT_+)$  strengths unquench at temperatures larger than  $\approx 2.6$  MeV and in the high-temperature limit approach the appropriate values for our adopted model space.

Ref. [77] has studied the pair correlations in the four nuclei  $^{54-58}\text{Fe}$  and  $^{56}\text{Cr}$  for the various isovector and isoscalar pairs up to  $J = 4$ , tentatively interpreting the sum of the eigenvalues of the matrix  $M^J$  (8.14) as an overall measure for the pairing strength. Note that the pairing strength, as defined in (8.12), is non-zero at the mean-field level. The physically relevant pair correlations  $P_{\text{corr}}^J$  are then defined as the difference of the SMMC and mean-field pairing strengths.

Detailed calculations of the pair correlations have been performed for selected temperatures in the region between  $T = 0.5$  MeV and 8 MeV. Fig. 8.13 shows the temperature dependence of those pair correlations that play an important role in understanding the thermal behavior of the moment of inertia and the total M1 and Gamow-Teller strengths.

The most interesting behavior is found in the  $J = 0$  proton and neutron pairs. There is a large excess of this pairing at low temperatures, reflecting the ground state coherence of even-even nuclei. With increasing temperature, this excess diminishes and vanishes at around  $T = 1.2$  MeV. We observe further from Fig. 8.13 that the temperature dependence of the  $J = 0$  proton-pair correlations are remarkably independent of the nucleus, while the neutron pair correlations show interesting differences. At first, the correlation excess is smaller in the semimagic nucleus  $^{54}\text{Fe}$  than in the others. When comparing the iron isotopes, the vanishing of the neutron  $J = 0$  correlations occurs at higher temperatures with increasing neutron number.

The vanishing of the  $J = 0$  proton and neutron pair correlations is accompanied by an increase in the correlations of the other pairs. For example, the isovector  $J = 0$  proton-neutron correlations increase by about a factor 3 after the  $J = 0$  proton and neutron pairs have vanished. The correlation peak is reached at higher temperatures with increasing neutron number, while the peak height decreases with neutron excess.

The isoscalar proton-neutron  $J = 1$  pairs show an interesting temperature dependence. At low temperatures, when the nucleus is still dominated by the  $J = 0$  proton and neutron pairs, the isoscalar proton-neutron correlations show a noticeable excess but, more interestingly, they are roughly constant and do not directly reflect the vanishing of the  $J = 0$  proton and neutron pairs. However, at  $T > 1$  MeV, where the  $J = 0$  proton- and neutron-pairs have broken, the isoscalar  $J = 1$  pair correlations significantly increase and have their maximum at around 2 MeV, with peak values of about twice the correlation excess in the ground state. In contrast to the isovector  $J = 0$  proton-neutron pairs, the correlation peaks occur at lower temperatures with increasing neutron excess. We also observe that these correlations fade rather slowly with increasing temperature.

We note that the SMMC results for the moment of inertia and the  $B(M1)$  and  $B(GT_+)$  strengths are significantly smaller than the mean-field values. The quenching of these ob-

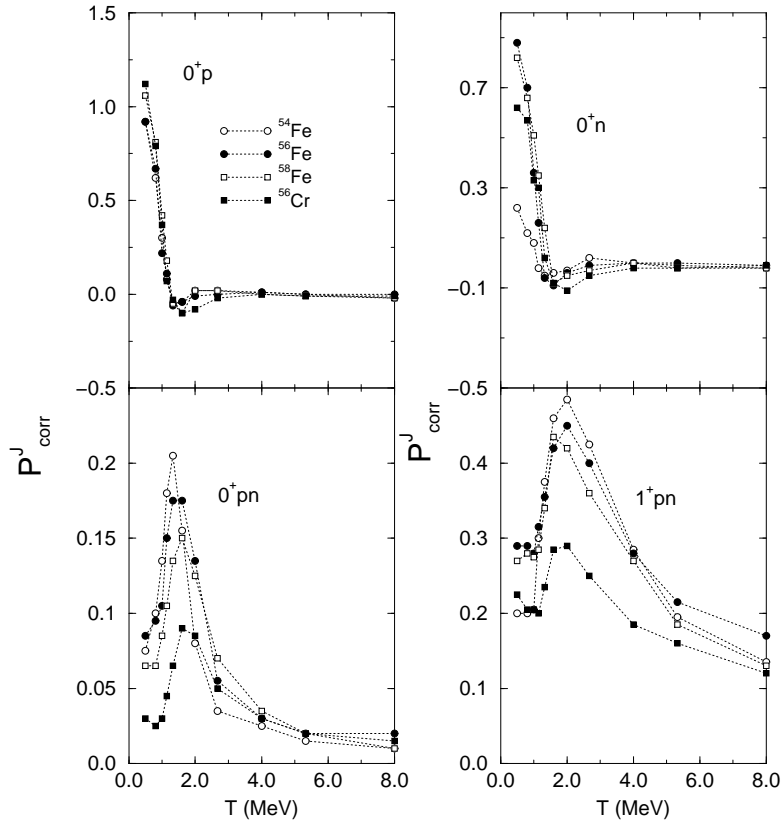


FIG 8.13 Pair correlations, as defined in Eq. (8.13), for isovector  $0^+$  and isoscalar  $1^+$  pairs for  $^{54-58}\text{Fe}$  and  $^{56}\text{Cr}$ , as functions of temperature (from [77]).

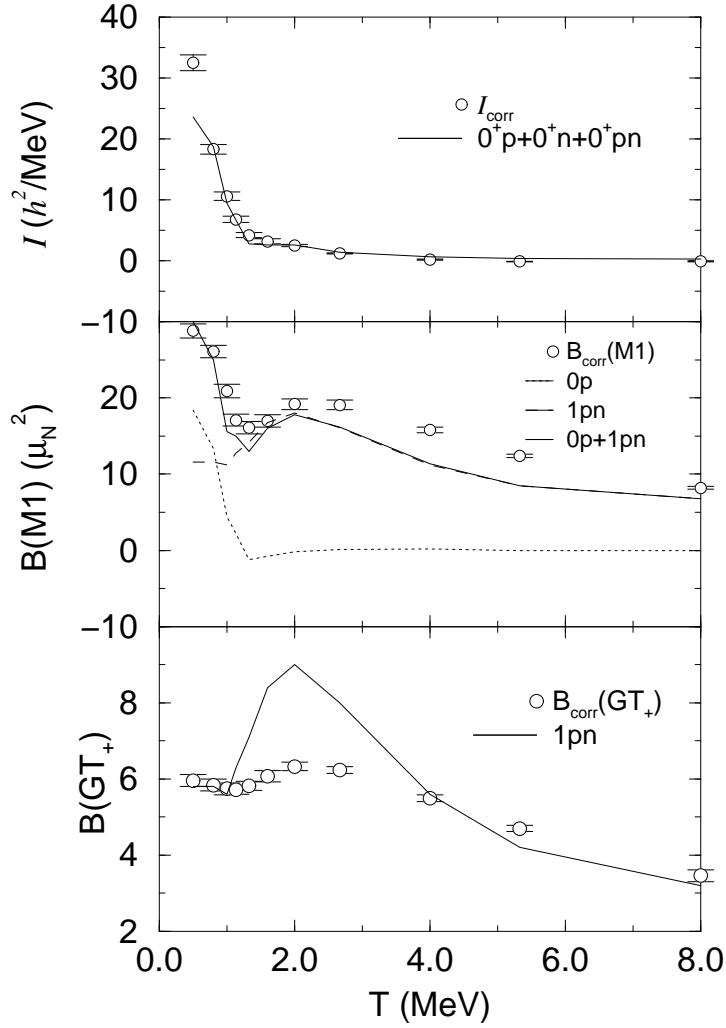


FIG 8.14. The temperature dependence of the quenching of the moment of inertia and of the total  $B(M1)$  and  $B(GT_+)$  strengths (see text) is compared to the one of selected pairing correlations (in arbitrary units). The results are shown for  $^{56}\text{Fe}$  (from [77]).

servables, defined as the difference of the mean-field and SMMC results, can be traced back to nucleon correlations beyond the mean-field. This is demonstrated in Fig. 8.14, exemplified for  $^{56}\text{Fe}$ . From its definition ( $I \sim \langle \hat{J}^2 \rangle = \langle (\hat{J}_n + \hat{J}_p)^2 \rangle$ , where  $\hat{J}_p, \hat{J}_n$  are the proton and neutron angular momenta, respectively), one expects that the moment of inertia is sensitive to the proton, neutron and proton-neutron correlations. In fact, the sum of the isovector  $J = 0$  pairing correlations shows nearly the same temperature behavior as the moment of inertia quenching. The drop in the quenching at  $T \approx 1$  MeV clearly signals the pairing phase transition observed in the  $J = 0$  proton and neutron correlations (see Fig. 8.13). The temperature dependence of the  $M1$  quenching is well described by that of the sum of the  $J = 0$  proton and isoscalar  $J = 1$  proton-neutron correlations. These two correlations reflect the two components in the  $M1$  strength. The orbital part is sensitive to the  $J = 0$  proton pairing correlations (the gyromagnetic moment  $g_l$  is zero for neutrons), while the quenching of the spin component is dominated by isoscalar proton-neutron correlations.

The quenching of the  $B(GT_+)$  strength is roughly constant for  $T < 1$  MeV. It then increases slightly, before it slowly dies out following a maximum at  $T \approx 2.5$  MeV. While the temperature dependence of the Gamow-Teller strength is driven by the isoscalar proton-neutron correlations, the overall measure of the pairing correlations, as applied here, is too simple for a quantitative reproduction.

## 8.5 Gamow-Teller quenching in the $^{100}\text{Sn}$ region

The double-magic nucleus  $^{100}\text{Sn}$  has recently been observed for the first time at GSI and Ganil [80, 81]. Detailed studies of this nucleus promise further insight into the shell structure in proton-rich nuclei and in particular into nature of Gamow-Teller (GT) quenching. The reasoning is as follows: the shell gap between the  $g_{9/2}$ -orbital and the other orbitals in the  $0g-1d-2s$  shell is expected to support a closed-shell structure for both neutrons and protons and suppress correlations involving the higher orbitals. The valence protons, occupying  $g_{9/2}$ -orbitals, will then be transformed with relatively less hindrance into  $g_{7/2}$ -neutrons by the  $\sigma\tau_+$  operator. Thus the quenching of the  $GT_+$ -strength due to configuration mixing is expected to be small.

Despite this reasoning, the observed quenching of the GT strength in the  $N = 50$  isotones close to  $^{100}\text{Sn}$  like  $^{94}\text{Ru}$ ,  $^{96}\text{Pd}$  and  $^{98}\text{Cd}$  is surprisingly large [82]. Strongly truncated shell model calculations are unable to reproduce the strong quenching, as the configuration mixing in these restricted model spaces was found to be insufficient [83, 84]. The agreement between theory and experiment has been improved by renormalization of the GT operator to consider (first-order) corrections to the wave functions [85, 86, 83, 84]. As shell model studies of lighter nuclei clearly stressed the need of a complete  $0\hbar\omega$  shell model basis, it appears unlikely that first-order corrections are sufficient to recover the full quenching of the GT strength due to configuration mixing.

Shell model Monte Carlo calculations have been performed for  $^{94}\text{Ru}$ ,  $^{96}\text{Pd}$ ,  $^{96,98}\text{Cd}$ , and  $^{100}\text{Sn}$  in the complete  $0g-1d-2s$  major oscillator shell using a G-matrix two-body interaction built from the Paris nucleon-nucleon interaction [87]. The Coulomb-corrected SMMC mass excesses agree well with the latest mass compilation of Myers and Swiatecki [88]. Table 3 gives the SMMC results for the Gamow-Teller strength, renormalizing the GT operator by  $1/1.26$ . The SMMC calculation predicts a noticeable quenching of the GT strength in the

Table 3: Comparison of the  $B(GT)$  strengths and quenching factors  $q$ , as calculated in our SMMC approach, with the data. The single particle estimates (SPE) for the  $B(GT)$  strength are also given (from [87]).

Nucleus	B(GT <sub>+</sub> ) (SPE)	B(GT <sub>+</sub> ) (SMMC)	$q$ (SMMC)	$q$ (expt) [82]
<sup>94</sup> Ru	7.11	1.48±0.1	4.96±0.3	7.2±0.6
<sup>96</sup> Pd	10.67	2.68±0.1	3.98±0.2	4.6 <sup>+1.7</sup> <sub>-0.8</sub>
<sup>96</sup> Cd	16.18	5.40±0.1	2.98±0.1	?
<sup>98</sup> Cd	14.22	4.42±0.1	3.22±0.1	4.1 <sup>+1</sup> <sub>-0.8</sub>
<sup>100</sup> Sn	17.78	6.50±0.1	2.74±0.1	?

$N = 50$  isotones, in accord with experiment. A detailed comparison with experiment is hampered by the fact that the measurement of the  $\beta^+$ -decay can only determine the GT strength below a certain energy threshold, so that the experiment actually provides only upper bounds for the quenching. In the case of <sup>96</sup>Pd and <sup>98</sup>Cd it is expected that the measurements miss less than about 10% of the total GT strength [83, 84], while for <sup>94</sup>Ru a significant amount of GT strength is predicted at energies that are not accessible in  $\beta^+$  experiments [83, 84]. It thus seems that SMMC calculations are in excellent agreement with the observed GT quenching for the nuclei <sup>96</sup>Pd and <sup>98</sup>Cd. For <sup>94</sup>Ru the SMMC result appears to be in qualitative agreement with observation. However, a quantitative comparison requires a detailed knowledge of the GT strength distribution in the daughter nucleus <sup>94</sup>Tc, which is outside the scope of the calculation of Ref. [87].

The SMMC calculations [87] also predict a noticeable quenching of the GT strength in the double-magic nucleus <sup>100</sup>Sn. Here, the total B(GT<sub>+</sub>)=6.5±0.1 should be compared to the single particle estimate of 17.78, corresponding to a quenching factor  $q = 2.74 \pm 0.1$ . This quenching factor is larger than predicted by recent truncated shell model calculations [84]. However, the ratio of quenching factors for <sup>98</sup>Cd and <sup>100</sup>Sn is found to be less interaction dependent than the actual values [84]. The SMMC calculation yields  $q(^{98}\text{Cd})/q(^{100}\text{Sn})=1.18 \pm 0.07$ , within the range 1.23 – 1.3 given in [84].

## 8.6 Electron capture and presupernova collapse

The core of a massive star at the end of hydrostatic burning is stabilized by electron degeneracy pressure as long as its mass does not exceed the appropriate Chandrasekhar mass  $M_{CH}$ . If the core mass exceeds  $M_{CH}$ , electrons are captured by nuclei [11] to avoid a violation of the Pauli principle:

$$e^- + (Z, A) \rightarrow (Z - 1, A) + \nu_e \quad (8.15)$$

The neutrinos can still escape from the core, carrying away energy. This is accompanied by a loss of pressure and the collapse is accelerated.

For many of the nuclei that determine the electron capture rate in the early stage of the presupernova [79], Gamow-Teller (GT) transitions contribute significantly to the electron capture rate. Due to insufficient experimental information, the GT<sub>+</sub> transition rates have so

far been treated only qualitatively in presupernova collapse simulations, assuming the  $GT_+$  strength to reside in a single resonance, whose energy relative to the daughter ground state has been parametrized phenomenologically [89]; the total  $GT_+$  strength has been taken from the single particle model. Recent  $(n, p)$  experiments [62]-[66], however, show that the  $GT_+$  strength is fragmented over many states, while the total strength is significantly quenched compared to the single particle model (see section 8.1). (A recent update of the  $GT_+$  rates for use in supernova simulations assumed a constant quenching factor of 2 [79]).

In a series of truncated shell model calculations, Aufderheide and collaborators have demonstrated that a strong phase space dependence makes the Gamow-Teller contributions to the presupernova electron capture rates more sensitive to the strength *distribution* in the daughter nucleus than to the total strength [90]. In this work it also became apparent that complete  $0\hbar\omega$  studies of the  $GT_+$  strength distribution are desirable. Such studies are now possible using the SMMC approach.

To determine the  $GT_+$  strength distribution we have calculated the response function of the  $\sigma\tau_+$  operator,  $R_{GT}(\tau)$ , as defined in Eq. (3.6). As the strength function  $S_{GT}(E)$  is the inverse Laplace transform of  $R_{GT}(\tau)$ , we have used the Maximum Entropy technique, described in section 6.4, to extract  $S_{GT}(E)$ . For the default model  $m(E)$  in (6.21) we adopted a Gaussian whose centroid is given by the slope of  $\ln R_{GT}(\tau)$  at small  $\tau$  and whose width is 2 MeV.

As first examples we have studied several nuclei ( $^{51}\text{V}$ ,  $^{54,56}\text{Fe}$ ,  $^{58,60,62}\text{Ni}$ , and  $^{59}\text{Co}$ ), for which the Gamow-Teller strength distribution in the daughter nucleus is known from  $(n, p)$  experiments [62]-[66]. Note that the electron capture by these nuclei, however, plays only a minor role in the presupernova collapse. As SMMC calculates the strength function within the parent nucleus, the results have been shifted using the experimental  $Q$ -value. The Coulomb correction has been performed using Eq. (8.1). For all nuclei, the SMMC approach calculates the centroid and width of the strength distribution in good agreement with data. (Following [52] the calculated strength distributions have been folded with Gaussians of width 1.77 MeV to account for the experimental resolution.) Fig. 8.15 shows the response function  $R_{GT}(\tau)$  for  $^{54}\text{Fe}$  and  $^{59}\text{Co}$  and compares the extracted  $GT_+$  strength distribution with data. (As discussed in sections 8.1 and 8.5, the Gamow-Teller operator has been renormalized by the factor 0.77). The centroid of the  $GT_+$  strength distributions is found to be nearly independent of temperature (calculations for odd nuclei could be performed only in the temperature range  $T = 0.8 - 1.2$  MeV), while its width increases with temperature.

Following the formalism described in Refs. [89, 79], the Gamow-Teller contributions to the electron capture rates under typical presupernova conditions have been calculated assuming that the electrons obey a Fermi-Dirac distribution with a chemical potential adopted from the stellar trajectory at the electron-to-nucleon ratio corresponding to the respective nucleus [79]. The calculation have been performed for both the SMMC and experimental  $GT_+$  strength distributions [62]-[66]. The electron capture rates so obtained agree within a factor of two for temperatures  $T = (3 - 5) \times 10^9$  Kelvin, which is the relevant temperature regime in the presupernova collapse [79] (Fig. 8.16). Note that this level of agreement is as good as that obtained by Aufderheide *et al.* [90]. These authors calculate the  $GT_+$  strength distribution within strongly truncated shell model studies by adjusting the single particle energies to fit the observed strength distribution and then normalize the total calculated strength to the measured  $B(GT_+)$  value [90]. As this approach obviously requires a knowledge of the

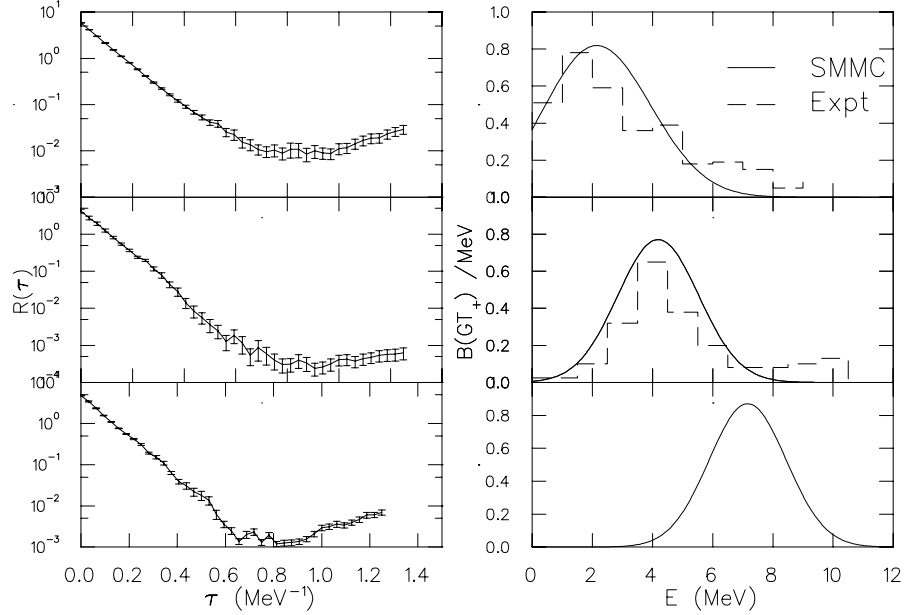


FIG 8.15. SMMC  $GT_+$  response functions (left side) and  $GT_+$  strength distributions (right side) for  $^{54}\text{Fe}$  (upper panel),  $^{59}\text{Co}$  (middle panel), and  $^{55}\text{Co}$  (lower panel). The energies refer to the daughter nuclei. The dashed histograms show the experimental strength distribution as extracted from  $(n, p)$  data [63].

experimental strength distribution, the SMMC calculations in the complete  $pf$  shell are capable of *predicting* the desired strength distribution with a similar accuracy. Thus, it is for the first time possible to calculate with a reasonable accuracy the electron capture rate for those nuclei like  $^{55}\text{Co}$  or  $^{56}\text{Ni}$  which dominate the electron capture process in the early presupernova collapse [79]. The SMMC calculation places the  $GT_+$  strength for  $^{55}\text{Co}$  at a higher energy in the daughter nucleus than the phenomenological parametrization of Fuller *et al.* [89]. Correspondingly, the electron capture rate on this nucleus, which is estimated to be dominated by the  $GT_+$  contribution, is smaller than previously assumed. Studies of the effect of this smaller rate on the dynamics of the early presupernova collapse must await the completion of SMMC calculations for other important  $pf$ -shell nuclei now in progress.

## 8.7 Temperature dependence of the nuclear symmetry energy

The size of the core mantle (the difference between the iron and homologous cores) is a major determinant of the supernova mechanism [11]. It has been argued recently that the mantle size might be significantly smaller than generally calculated in supernova models because of an overlooked temperature dependence of the electron capture process [91]. The detailed reasoning is as follows [92]: When the nucleus is described by a static mean field model, dynamical effects associated with collective surface vibrations are conventionally embodied in an effective nucleon mass,  $m^*$  (as are spatial non-localities in the mean field). Donati *et al.* [92] studied the coupling of the mean field single-particle levels to the collective

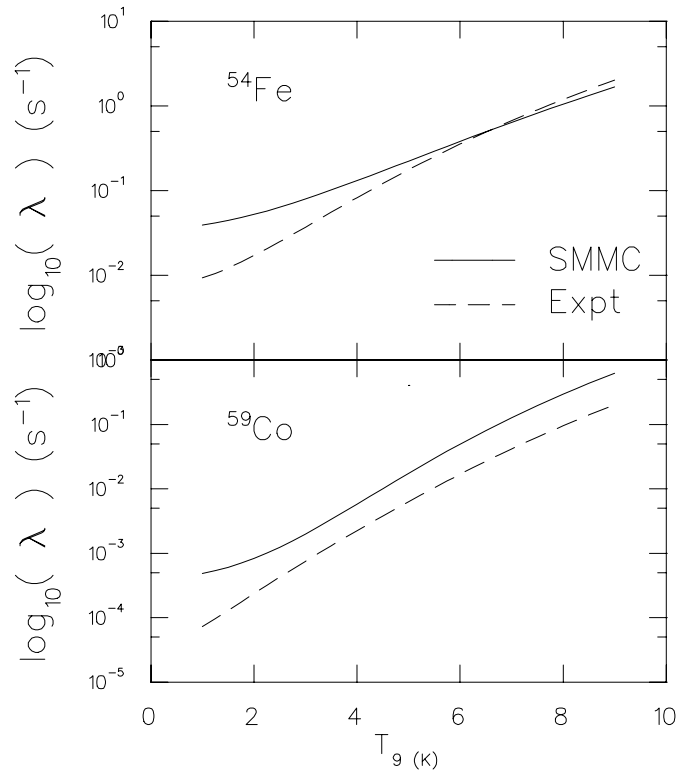


FIG 8.16. Gamow-Teller contributions to the electron capture rates on  $^{54}\text{Fe}$  and  $^{59}\text{Co}$  as a function of temperature ( $T_9$  measures the temperature in  $10^9$  Kelvin.) The calculations have been performed for the experimental strength distribution [63] and the SMMC result.

surface vibrations within the quasiparticle random phase approximation and found that  $m^*$  decreases with increasing temperature for  $T \leq 2$  MeV, the temperatures relevant for the presupernova collapse. They attributed this behavior to a reduction of collectivity at low excitation energies. In the Fermi gas model, this decrease of  $m^*$  induces an increase in the symmetry energy contribution to the nuclear binding energy

$$E_{\text{sym}}(T) = b_{\text{sym}}(T) \frac{(N - Z)^2}{A}, \quad (8.16)$$

where  $N$ ,  $Z$ , and  $A$  are the neutron, proton, and mass numbers of the nucleus, respectively. Quantitatively, Donati *et al.* estimate that  $b_{\text{sym}}(T)$  increases by about 2.5 MeV as  $T$  increases from 0 to 1 MeV ( $b_{\text{sym}}(0) \approx 28$  MeV [2]). Importantly, a larger value of  $E_{\text{sym}}(T)$  would hinder electron capture in the presupernova environment, and thus reduce the size of the core mantle, so that the shock wave would need significantly less energy to stop the collapse and explode the star.

To explore the temperature dependence of the symmetry energy, SMMC calculations were used [93] to study the thermal properties of various pairs of isobars in the mass region  $A = 54 - 64$  which is important for the presupernova collapse; this includes two of the three nuclei studied in Ref. [92] ( $^{64}\text{Zn}$  and  $^{64}\text{Ni}$ ).

The discussion focuses on the temperature dependence of the internal energy of a nucleus (with proton and neutron numbers  $Z$  and  $N$ ), which is defined as

$$U(N, Z, T) = \langle \hat{H} \rangle(T) - \langle \hat{H} \rangle(T = 0), \quad (8.17)$$

where  $\langle \hat{H} \rangle(T)$  is the expectation value of the Hamiltonian in the canonical ensemble at temperature  $T$ . Guided by the semi-empirical parametrization of the binding energies (e.g., the Bethe-Weizsäcker formula), the difference of  $U(T)$  for two isobars

$$\Delta U(T) = U(N_1, Z_1, T) - U(N_2, Z_2, T) \quad ; \quad N_1 + Z_1 = N_2 + Z_2 = A \quad (8.18)$$

should reflect the proposed temperature dependence of the symmetry energy contribution to the binding energies. This proportionality is valid only if the other contributions to the binding energy, particularly nuclear structure effects, are negligible in  $\Delta U(T)$ . To investigate this point, Dean *et al.* [93] performed calculations for several pairs of isobars for mass numbers  $A = 54$  ( $^{54}\text{Fe}$ ,  $^{54}\text{Cr}$ ),  $A = 56$  ( $^{56}\text{Fe}$ ,  $^{56}\text{Cr}$ ),  $A = 58$  ( $^{58}\text{Ni}$ ,  $^{58}\text{Fe}$ ),  $A = 60$  ( $^{60}\text{Ni}$ ,  $^{60}\text{Fe}$ ),  $A = 62$  ( $^{62}\text{Zn}$ ,  $^{62}\text{Ni}$ ) and  $A = 64$  ( $^{64}\text{Zn}$ ,  $^{64}\text{Ni}$ ).

The experimental knowledge of the excitation spectra for the nuclei studied appeared to be sufficient to derive  $U(T)$  for  $T \leq 0.5$  MeV solely from data. For higher temperatures these values were supplemented with the appropriate SMMC results for  $U(T) - U(T = 0.5 \text{ MeV})$ . Fig. 8.17 compares  $\Delta U(T)$  for  $T = 1$  MeV as calculated by the combination of data and SMMC results [93] with the predictions of Ref. [92]. For all isobaric pairs with the exception of ( $^{64}\text{Ni}$ ,  $^{64}\text{Zn}$ ), the values for  $\Delta U(T)$  are compatible with zero (no increase of  $b_{\text{symm}}$  with temperature). However, we note that, in agreement with Ref. [92], the SMMC calculation shows an increase in  $b_{\text{symm}}$  for the  $A = 64$  pair ( $^{64}\text{Ni}$ ,  $^{64}\text{Zn}$ ). However, it does not confirm that this increase is generic.

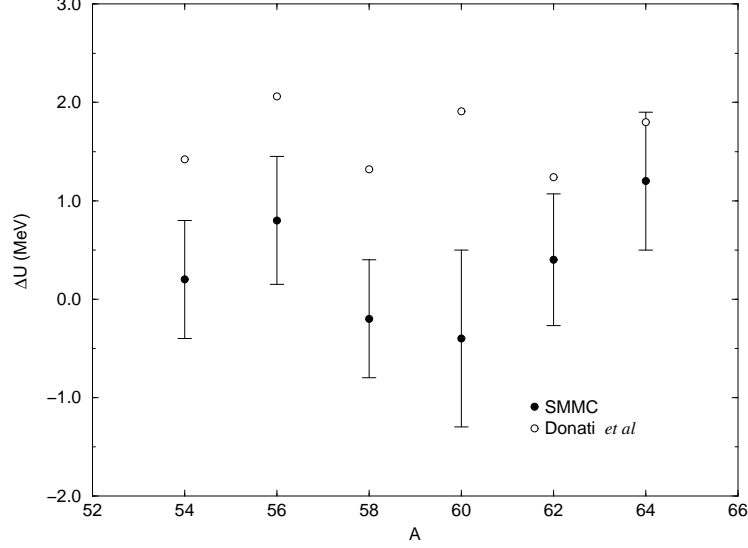


FIG 8.17. Comparison of the values for  $\Delta U(T)$  predicted by Donati *et al.* (open circles, [92]) with the results calculated from experimental data and SMMC calculations for selected pairs of isobars, as described in the text (full circles).

## 8.8 $^{170}\text{Dy}$ at finite rotation and temperature

A first SMMC calculation [59] to describe rare-earth nuclei used the  $Z = 50\text{--}82$  shell for protons ( $2s1d0g_{7/2}0h_{11/2}$ ) and the  $N = 82\text{--}126$  shell for neutrons ( $2p1f0g_{9/2}0i_{13/2}$ ). The Hamiltonian chosen was of the pairing plus quadrupole form given by

$$\hat{H} = \sum_{\alpha} \varepsilon_{\alpha} a_{\alpha}^{\dagger} a_{\alpha} - g_p \hat{P}_p^{\dagger} \hat{P}_p - g_n \hat{P}_n^{\dagger} \hat{P}_n - \frac{\chi}{2} \hat{Q} \cdot \hat{Q}, \quad (8.19)$$

where  $\varepsilon_{\alpha}$  are the single particle energies,  $\hat{P}_{p(n)}^{\dagger}, \hat{P}_{p(n)}$  are the monopole pair creation and annihilation operators for protons and neutrons, and  $\hat{Q} = \hat{Q}_p + \hat{Q}_n$  is the quadrupole operator. The pairing strengths  $g_{p(n)}$ , the quadrupole interaction strength  $\chi$ , and the single particle energies used were taken from [40].

The nucleus considered was  $^{170}\text{Dy}$ . It involved 16 valence protons and 22 valence neutrons moving among the  $N_s = 32$  and 44 single-particle states, respectively, giving a total of  $10^{21}$   $m$ -scheme determinants. The calculations used  $\Delta\beta = 0.0625 \text{ MeV}^{-1}$  and  $N_t = 8$  to 64 time slices. Due to limited computer memory and cycles at that time, it was necessary to perform canonical analyses of the fields generated through grand-canonical sampling; all other work in this Report uses canonical sampling. In particular, for the  $^{170}\text{Dy}$  calculation, canonical observables (subscript “ $c$ ”) are given in terms of the grand-canonical sampling (subscript “ $G$ ”) as

$$\langle \hat{\Omega} \rangle_c = \frac{\int D\sigma W_{G\sigma} \Phi_{c\sigma} [\zeta_{c\sigma} / \zeta_{G\sigma}] \langle \Omega \rangle_{c\sigma}}{\int D\sigma W_{G\sigma} \Phi_{c\sigma} [\zeta_{c\sigma} / \zeta_{G\sigma}]}, \quad (8.20)$$

where  $\zeta_{\sigma} = \text{Tr} \hat{U}_{\sigma}$ . Although this is an exact expression, the fluctuations in  $[\zeta_{c\sigma} / \zeta_{G\sigma}]$  determine how precise the Monte Carlo evaluation can be. We found that the fluctuations are

less than 10% (as the number dispersion in the grand-canonical ensemble is small), so that canonical observables can be calculated with good precision.

In Fig. 8.18 we show the static observables (for the uncranked system) in both the grand-canonical and canonical formalisms. We calculated observables canonically, using grand canonical fields, up to  $\beta = 2.0$  in order to demonstrate that, for these nuclear systems, either method may be used in this kind of calculation. As the temperature decreases, the nucleus becomes more deformed. Relaxation of the expectation values of  $\hat{H}$  and  $\hat{J}^2$  is also clearly seen. The sign in these cases is identically one for all temperatures.

Cranking calculations in which  $\hat{H} \rightarrow \hat{H} - \omega \hat{J}_z$  were also performed. The systematics are shown in Fig. 8.19, where we display the Monte Carlo sign  $\langle \Phi \rangle$ ,  $\langle \hat{H} \rangle$ ,  $\langle \hat{Q}^2 \rangle$ ,  $\langle \hat{J}^2 \rangle$ , the pairing energy  $-g \langle \hat{P}^\dagger \hat{P} \rangle = -g_p \langle \hat{P}^\dagger \hat{P} \rangle_p - g_n \langle \hat{P}^\dagger \hat{P} \rangle_n$ , and the moment of inertia,  $\langle \mathcal{I}_2 \rangle$ . Note that the sign degrades quite rapidly with increasing  $\omega$ , making cranking calculations at lower temperatures difficult. Moments of inertia were calculated from  $\mathcal{I}_2 = d \langle \hat{J}_z \rangle / d\omega = \beta [\langle \hat{J}_z^2 \rangle - \langle \hat{J}_z \rangle^2]$ . At high temperatures, the nucleus is unpaired and the moment of inertia decreases as the system is cranked. However, for lower temperatures when the nucleons are paired, the moment of inertia initially increases as we begin to crank, but then decreases at larger cranking frequencies as pairs break; Figure 8.19 shows that the pairing gap also decreases as a function of  $\omega$ . It is well known that the moment of inertia depends on the pairing gap [94], and that initially  $\mathcal{I}_2$  should increase with increasing  $\omega$ . Once the pairs have been broken, the moment of inertia decreases. These features are evident in the figure.

It is of particular interest to determine the quadrupole shape of a nucleus as function of temperature and angular momentum. It is generally expected that some nuclei may exhibit a sudden phase transition from a prolate to spherical shape as the temperature increases [95]. In addition, as the cranking frequency is increased a transition to oblate ellipsoids is also expected.

In order to obtain a more detailed picture of the deformation, we examine the components of the quadrupole operator  $\hat{Q}_\mu = r^2 Y_{2\mu}^*$ . Note, however, that due to rotational invariance of the uncranked Hamiltonian, the expectation value of any component  $\hat{Q}_\mu$  is expected to vanish. On the other hand, there is an intrinsic frame for each Monte Carlo sample, in which it is possible to compute the three non-zero components  $Q'_0$ ,  $Q'_2$ , and  $Q'_{-2}$  (the prime is used to denote the intrinsic frame). The intrinsic quadrupole moments can then be related to the standard deformation coordinates  $\beta$  and  $\gamma$  [2, 28]. The task remains to compute the quadrupole moments in the intrinsic frame for each Monte Carlo sample. This is accomplished by computing and diagonalizing the expectation value of the cartesian quadrupole tensor  $Q_{ij} = 3x_i x_j - \delta_{ij} r^2$  for each Monte Carlo sample. From the three eigenvalues, it is straightforward to determine the deformation parameters as in [96].

Figure 8.20 shows the evolution of the shape distribution for  $^{170}\text{Dy}$  at inverse temperatures  $T^{-1} = 0.5, 1.0, 2.0,$  and  $3.0 \text{ MeV}^{-1}$ . These contour plots show the free energy  $F(\beta, \gamma)$ , obtained from the shape probability distribution,  $P(\beta, \gamma)$ , by

$$F(\beta, \gamma) = -T \ln \frac{\mathcal{P}(\beta, \gamma)}{\beta^3 \sin 3\gamma} \quad (8.21)$$

where the  $\beta^3 \sin 3\gamma$  is the metric in the usual deformation coordinates;  $\mathcal{P}$  was obtained simply by binning the Monte Carlo samples in the  $\beta - \gamma$  plane. As is seen from the plots,

deformation clearly sets in with decreasing temperature. At high temperatures, the system is nearly spherical, whereas at lower temperatures, especially at  $T^{-1} = 3.0 \text{ MeV}^{-1}$ , there is a prolate minimum on the  $\gamma = 0$  axis.

## 8.9 $\gamma$ -soft nuclei

Nuclei with mass number  $100 \leq A \leq 140$  are believed to have large shape fluctuations in their ground states. Associated with this softness are spectra with an approximate  $O(5)$  symmetry and bands with energy spacings intermediate between rotational and vibrational. In the geometrical model these nuclei are described by potential energy surfaces with a minimum at  $\beta \neq 0$  but independent of  $\gamma$  [97]. Some of these nuclei have been described in terms of a quartic five-dimensional oscillator [98]. In the Interacting Boson Model (IBM) they are described by an  $O(6)$  dynamical symmetry [13, 99, 100]. In the following we review the first fully microscopic calculations for soft nuclei with  $100 \leq A \leq 140$  [101].

For the two-body interaction we used a monopole ( $J = 0$ ) plus quadrupole ( $J = 2$ ) force [102] supplemented by a collective quadrupole interaction:

$$\hat{H}_2 = - \sum_{\lambda\mu} \frac{\pi g_\lambda}{2\lambda + 1} \hat{P}_{\lambda\mu}^\dagger \hat{P}_{\lambda\mu} - \frac{1}{2} \chi : \sum_{\mu} (-)^{\mu} \hat{Q}_{\mu} \hat{Q}_{-\mu} : , \quad (8.22)$$

where  $::$  denotes normal ordering. The single particle energies and the other parameters were determined as described in Ref. [101].

We begin discussion of our results with the probability distribution of the quadrupole moment. The calculation of the shape distributions included the quantum-mechanical fluctuations through the variance of the  $\hat{Q}$  operator for each sample,  $\Delta_{\sigma}^2 = \text{Tr}(\hat{Q}^2 \hat{U}_{\sigma}) / \text{Tr}(\hat{U}_{\sigma}) - \langle \hat{Q} \rangle_{\sigma}^2$ . The shape distribution  $P(\beta, \gamma)$  can be converted to a free energy surface as described by Eq. (8.19).

The shape distributions of  $^{128}\text{Te}$  and  $^{124}\text{Xe}$  are shown in Fig. 8.21 at different temperatures. These nuclei are clearly  $\gamma$ -soft, with energy minima at  $\beta \sim 0.06$  and  $\beta \sim 0.15$ , respectively. Energy surfaces calculated with Strutinsky-BCS using a deformed Woods-Saxon potential [103] also indicate  $\gamma$ -softness with values of  $\beta$  comparable to the SMMC values. These calculations predict for  $^{124}\text{Xe}$  a prolate minimum with  $\beta \approx 0.20$  which is lower than the spherical configuration by 1.7 MeV but is only 0.3 MeV below the oblate saddle point, and for  $^{128}\text{Te}$  a shallow oblate minimum with  $\beta \approx 0.03$ . These  $\gamma$ -soft surfaces are similar to those obtained in the  $O(6)$  symmetry of the IBM, or more generally when the Hamiltonian has mixed  $U(5)$  and  $O(6)$  symmetries but a common  $O(5)$  symmetry. In the Bohr Hamiltonian, an  $O(5)$  symmetry occurs when the collective potential energy depends only on  $\beta$  [97]. The same results are consistent with a potential energy  $V(\beta)$  that has a quartic anharmonicity [98], but with a negative quadratic term that leads to a minimum at finite  $\beta$ .

The total E2 strengths were estimated from  $\langle \hat{Q}^2 \rangle$  where  $\hat{Q} = e_p \hat{Q}_p + e_n \hat{Q}_n$  is the electric quadrupole operator with effective charges of  $e_p = 1.5e$  and  $e_n = 0.5e$ , and  $B(E2; 0_1^+ \rightarrow 2_1^+)$  determined by assuming that most of the strength is in the  $2_1^+$  state. Values for  $B(E2; 0_1^+ \rightarrow 2_1^+)$  of  $663 \pm 10$ ,  $2106 \pm 15$ , and  $5491 \pm 36 \text{ e}^2\text{fm}^4$  were found, to be compared with the experimental values [104] of 1164, 3910, and 9103  $\text{e}^2\text{fm}^4$  for  $^{124}\text{Sn}$ ,  $^{128}\text{Te}$  and  $^{124}\text{Xe}$ , respectively. Thus, the SMMC calculations reproduce the correct qualitative trend. The  $2_1^+$  excitation

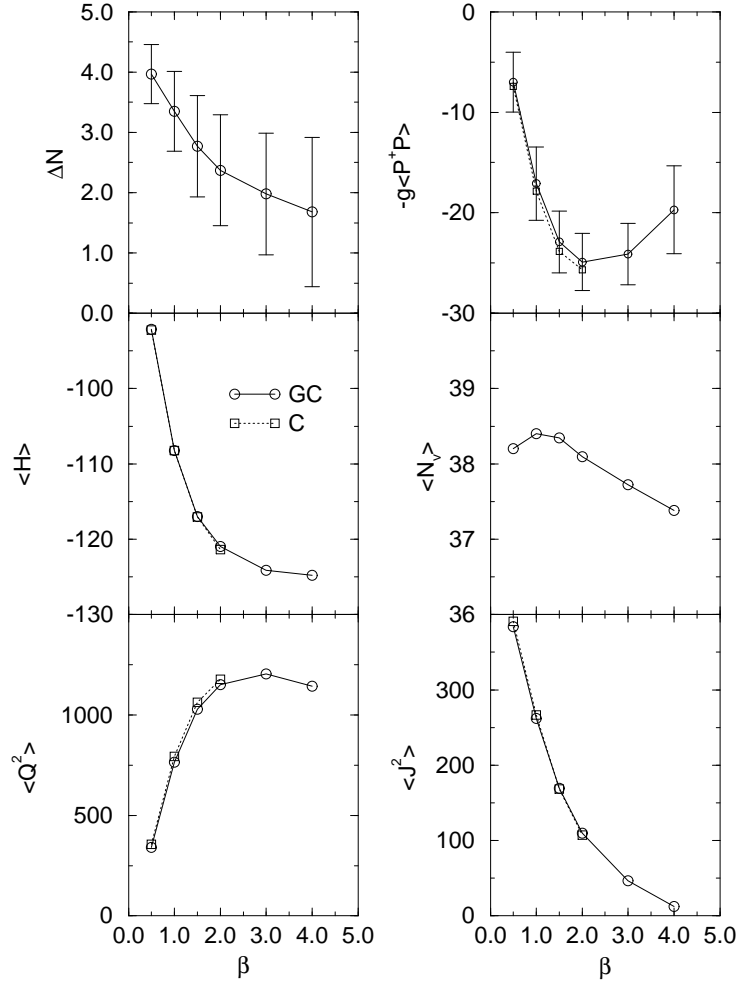


FIG 8.18 Canonical and grand-canonical static observables are shown for the uncranked  $^{170}\text{Dy}$  system as a function of  $\beta$ . Circles represent results of canonical projection of the grand-canonical fields, and squares show the grand-canonical results. Lines are drawn to guide the eye. We show expectation values of the energy  $\langle \hat{H} \rangle$ , the isoscalar quadrupole  $\langle \hat{Q}^2 \rangle$ , the valence nucleon number  $\langle \hat{N} \rangle$ , and the number variance  $\langle \Delta N \rangle = \sqrt{\langle \hat{N}^2 \rangle - \langle \hat{N} \rangle^2}$  (grand-canonical only), the squared angular momentum  $\langle \hat{J}^2 \rangle$  and the pairing energy  $-g \langle \hat{P}^\dagger \hat{P} \rangle$ , which is the expectation value of the pairing terms in the Hamiltonian (from [59]).

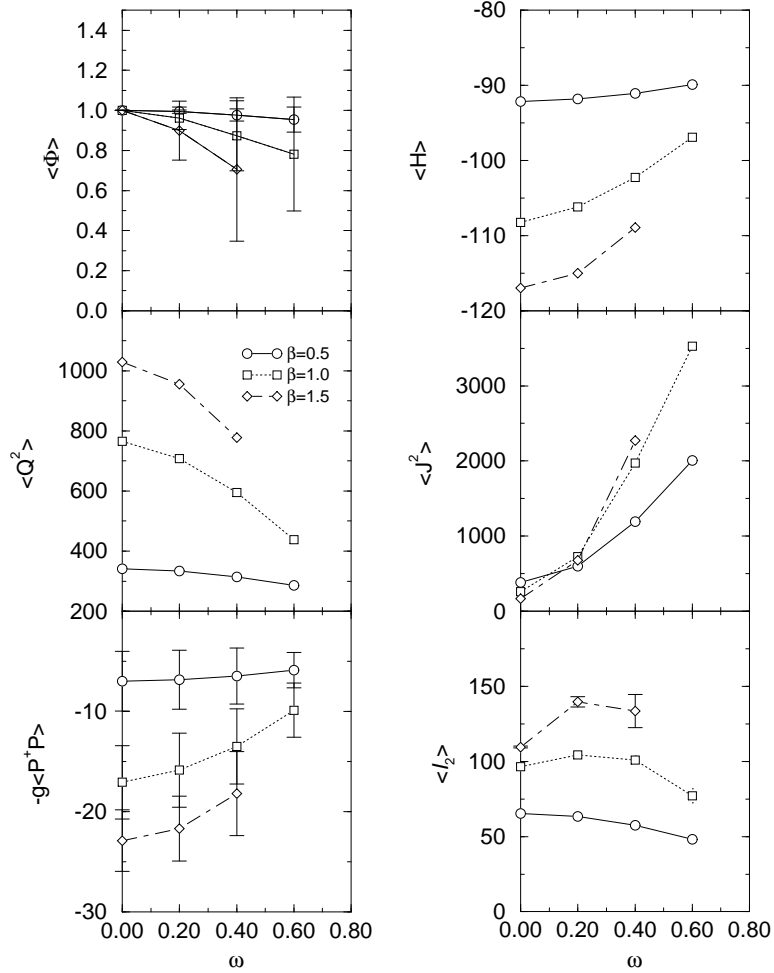


FIG 8.19. Grand-canonical observables for  $^{170}\text{Dy}$  at various cranking frequencies and temperatures. We show the average sign  $\langle \Phi \rangle$ , the isoscalar quadrupole moment  $\langle \hat{Q}^2 \rangle$ , the energy  $\langle \hat{H} \rangle$ , the square of the angular momentum  $\langle \hat{J}^2 \rangle$ , the moment of inertia  $\langle \mathcal{I}_2 \rangle$ , and the expectation value of the pairing terms in the Hamiltonian,  $-g \langle \hat{P}^\dagger \hat{P} \rangle$  (from [59]).

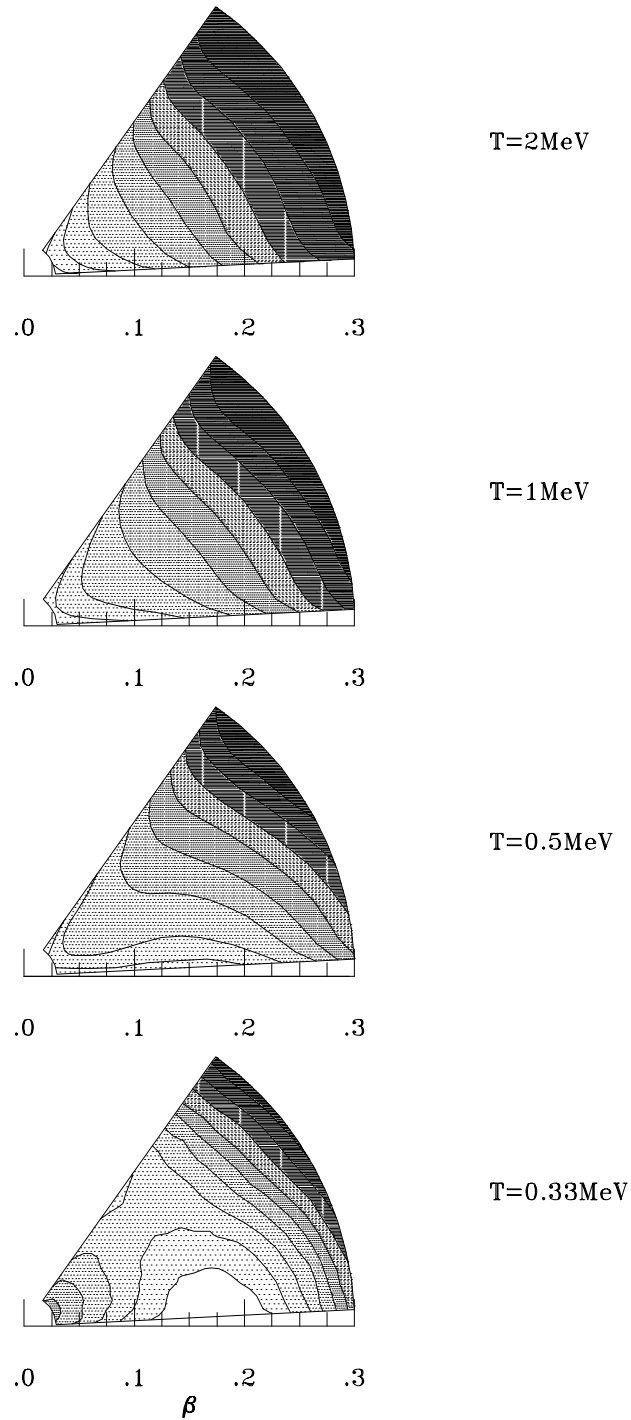


FIG 8.20. Contour plots of the free energy (as described in the text) in polar coordinates in the  $\beta$ - $\gamma$  plane are shown for the  $^{170}\text{Dy}$  system. Inverse temperatures are from 0.5 (top) 1.0, 2.0, and 3.0  $\text{MeV}^{-1}$  (bottom). Contours are shown at 0.3  $\text{MeV}$  intervals. Lighter shades indicate the more probable nuclear shapes (from [59]).

energies were also calculated from the E2 response function. The values of  $1.12 \pm 0.02$ ,  $0.96 \pm 0.02$  and  $0.52 \pm 0.01$  MeV are in close agreement with the experimental values of 1.2, 0.8 and 0.6 MeV for  $^{124}\text{Sn}$ ,  $^{128}\text{Te}$  and  $^{124}\text{Xe}$ , respectively.

Another indication of softness is the response of the nucleus to rotations, probed by adding a cranking field  $\omega J_z$  to the Hamiltonian and examining the moment of inertia as a function of the cranking frequency  $\omega$ . For a soft nucleus one expects a behavior intermediate between a deformed nucleus, where the inertia is independent of the cranking frequency, and the harmonic oscillator, where the inertia becomes singular. This is confirmed in Fig. 8.22 which shows the moment of inertia  $\mathcal{I}_2$  for  $^{124}\text{Xe}$  and  $^{128}\text{Te}$  as a function of  $\omega$ , and indicates that  $^{128}\text{Te}$  has a more harmonic character. The moment of inertia for  $\omega = 0$  in both nuclei is significantly lower than the rigid body value ( $\approx 43\hbar^2/\text{MeV}$  for  $A = 124$ ) due to pairing correlations.

Also shown in Fig. 8.22 are  $\langle \hat{Q}^2 \rangle$  where  $\hat{Q}$  is the mass quadrupole, the BCS-like pairing correlation  $\langle \hat{\Delta}^\dagger \hat{\Delta} \rangle$  for the protons and  $\langle \hat{J}_z \rangle$  (neutron pairing is less affected, and therefore not shown). Notice that the increase in  $I_2$  as a function of  $\omega$  is strongly correlated with the rapid decrease of pairing correlations and that the peaks in  $I_2$  are associated with the onset of a decrease in collectivity (as measured by  $\langle \hat{Q}^2 \rangle$ ). This suggests band crossing along the yrast line associated with pair breaking and alignment of the quasi-particle spins at  $\omega \approx 0.2$  MeV ( $\langle \hat{J}_z \rangle \approx 7\hbar$ ) for  $^{128}\text{Te}$  and  $\omega \approx 0.3$  MeV ( $\langle \hat{J}_z \rangle \approx 11\hbar$ ) for  $^{124}\text{Xe}$ . The results are consistent with an experimental evidence of band crossing in the yrast sequence of  $^{124}\text{Xe}$  around spin of  $10 \hbar$  [105]. The alignment effect is clearly seen in the behavior of  $\langle \hat{J}_z \rangle$  at the lower temperature, which shows a rapid increase after an initial moderate change. Deformation and pairing decrease also as a function of temperature.

The total number of  $J$ -pairs ( $n_J = \sum_\alpha n_{\alpha J}$ ) in the various pairing channels was also calculated; the results for the number of correlated pairs (after subtracting the mean-field values) are shown in Fig. 8.23. Since the number of neutrons in  $^{124}\text{Xe}$  is larger than the mid-shell value, they are treated as holes. For  $J = 0$  and  $J = 2$  one can compare the largest  $n_{\alpha J}$  with the number of  $s$  and  $d$  bosons obtained from the  $O(6)$  limit of the IBM. For  $^{124}\text{Xe}$  the SMMC (IBM) results in the proton-proton pairing channel are 0.85 (1.22)  $s$  ( $J = 0$ ) pairs, and 0.76 (0.78)  $d$  ( $J = 2$ ) pairs, while in the neutron-neutron channel we find 1.76 (3.67)  $s$  pairs and 2.14 (2.33)  $d$  pairs. For the protons the SMMC  $d$  to  $s$  pair ratio 0.89 is close to its  $O(6)$  value of 0.64. However, the same ratio for the neutrons, 1.21, is intermediate between  $O(6)$  and  $SU(3)$  (where its value is 1.64) and is consistent with the neutrons filling the middle of the shell. The total numbers of  $s$  and  $d$  pairs – 1.61 proton pairs and 3.8 neutron (hole) pairs – are below the IBM values of 2 and 6, respectively.

## 8.10 Double-beta decay

The second-order weak process  $(Z, A) \rightarrow (Z+2, A) + 2e^- + 2\bar{\nu}_e$  is an important “background” to searches for the lepton-number violating neutrinoless mode,  $(Z, A) \rightarrow (Z+2, A)$ . The calculation of the nuclear matrix element for these two processes is a challenging problem in nuclear structure, and has been done in a full  $pf$  model space for only the lightest of several candidates,  $^{48}\text{Ca}$ . P.B. Radha *et al.* have performed first Monte Carlo calculations of the  $2\nu \beta\beta$  matrix elements in very large model spaces [106].

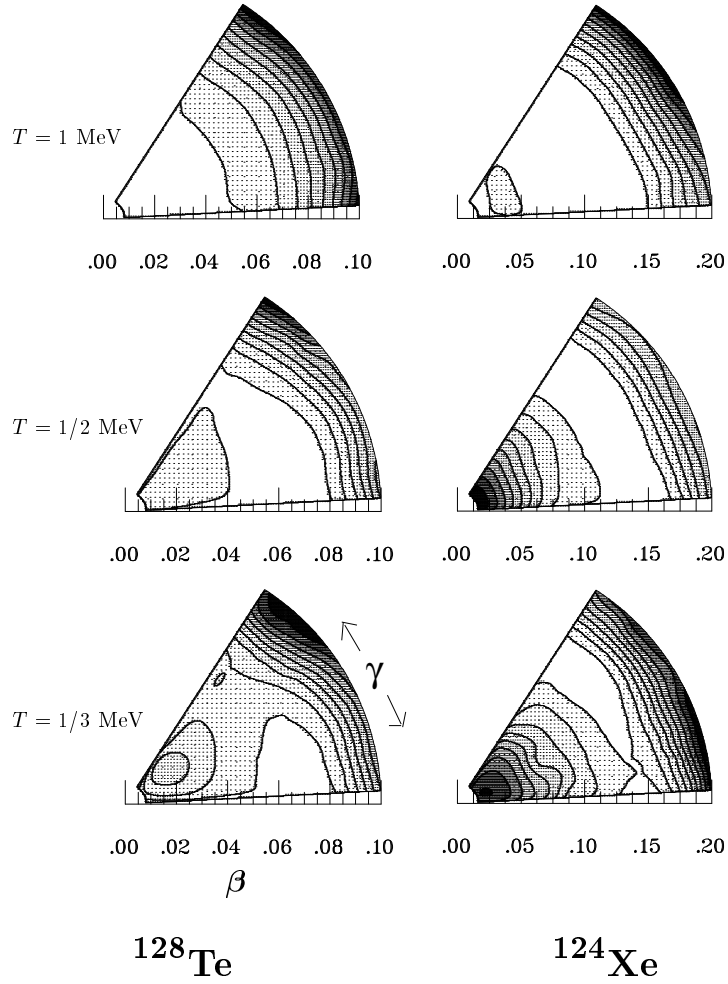


FIG 8.21. Contours of the free energy (as described in the text) in the polar-coordinate  $\beta - \gamma$  plane for  $^{128}\text{Te}$  and  $^{124}\text{Xe}$ . Contours are shown at 0.3 MeV intervals, with lighter shades indicating the more probable nuclear shapes (from [101]).

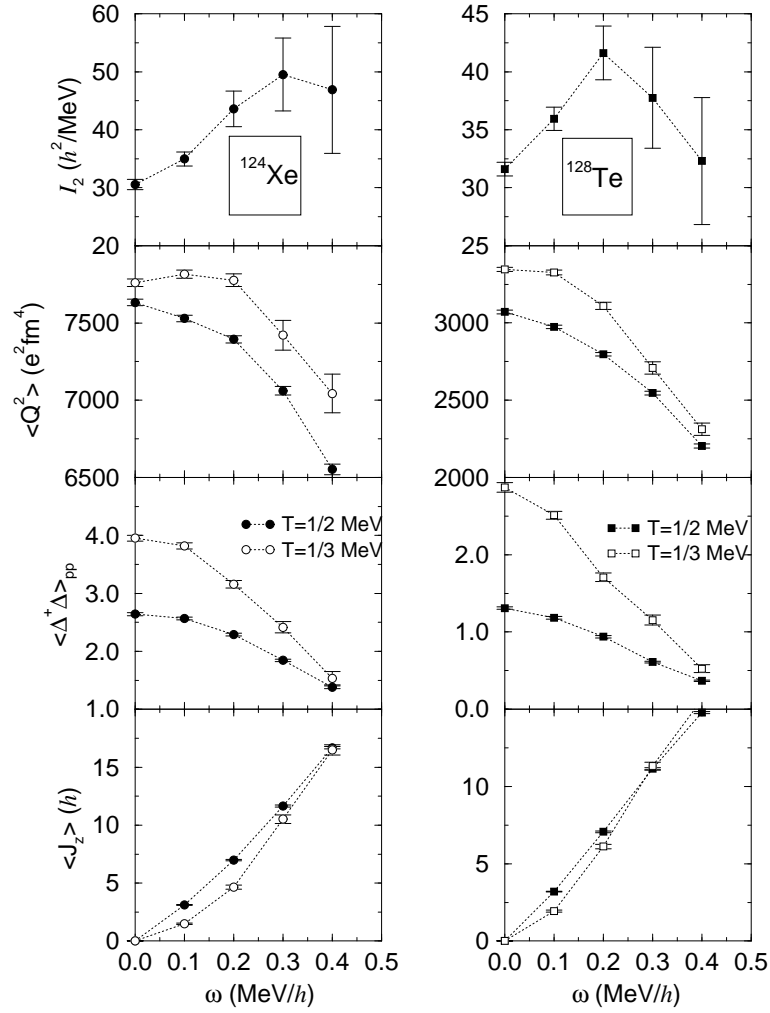


FIG 8.22. Observables for  $^{124}\text{Xe}$  and  $^{128}\text{Te}$  as a function of cranking frequency  $\omega$  and for two temperatures.  $I_2$  is the moment of inertia,  $Q$  is the mass quadrupole moment,  $\Delta$  is the  $J = 0$  pairing operator, and  $J_z$  is the angular momentum along the cranking axis (from [101]).

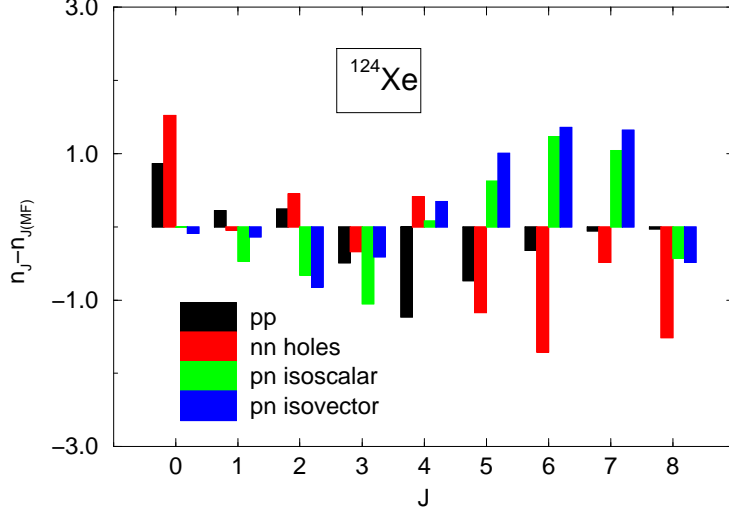


FIG 8.23. Number of correlated pairs of angular momentum  $J$  in  $^{124}\text{Xe}$ . Different shades correspond to p-p, n-n, isoscalar and isovector p-n pairs. Neutrons are treated as holes.

In two-neutrino double  $\beta$ -decay, the nuclear matrix element of interest is

$$M^{2\nu} \equiv \sum_m \frac{\langle f_0 | \hat{\mathbf{G}} | m \rangle \cdot \langle m | \hat{\mathbf{G}} | i_0 \rangle}{E_m - \Omega}, \quad (8.23)$$

where  $|i_0\rangle$  and  $|f_0\rangle$  are the  $0^+$  ground states of the initial and final even-even nuclei, and  $|m\rangle$  is a  $1^+$  state of the intermediate odd-odd nucleus; the sum is over all such states. In this expression,  $\hat{\mathbf{G}} = \sigma\tau_-$  is the Gamow-Teller operator for  $\beta^-$ -decay (i.e., that which changes a neutron into a proton) and  $\Omega = (E_{i_0} + E_{f_0})/2$ . A common approximation to  $M^{2\nu}$  is the closure value,

$$M^{2\nu} = \frac{M_c}{\bar{E}} \quad (8.24)$$

where  $\bar{E}$  is an average energy dominator and

$$M_c \equiv \sum_m \langle f_0 | \hat{\mathbf{G}} | m \rangle \langle m | \hat{\mathbf{G}} | i_0 \rangle = \langle f_0 | \hat{\mathbf{G}} \cdot \hat{\mathbf{G}} | i_0 \rangle. \quad (8.25)$$

SMMC methods can be used to calculate both  $M_c$  and  $M^{2\nu}$ . To do so, consider the function

$$\begin{aligned} \phi(\tau, \tau') &= \langle e^{\hat{H}(\tau+\tau')} \hat{\mathbf{G}}^\dagger \cdot \hat{\mathbf{G}}^\dagger e^{-\hat{H}\tau} \hat{\mathbf{G}} e^{-\hat{H}\tau'} \hat{\mathbf{G}} \rangle \\ &= \frac{1}{Z} \text{Tr}_A \left[ e^{-(\beta-\tau-\tau')\hat{H}} \hat{\mathbf{G}}^\dagger \cdot \hat{\mathbf{G}}^\dagger e^{-\tau\hat{H}} \hat{\mathbf{G}} e^{-\tau'\hat{H}} \hat{\mathbf{G}} \right], \end{aligned} \quad (8.26)$$

where  $Z = \text{Tr}_A e^{-\beta\hat{H}}$  is the partition function for the initial nucleus,  $\hat{H}$  is the many-body Hamiltonian, and the trace is over all states of the initial nucleus. The quantities  $(\beta - \tau - \tau')$  and  $\tau$  play the role of the inverse temperature in the parent and daughter nucleus respectively. A spectral expansion of  $\phi$  shows that large values of these parameters guarantee cooling to the parent and daughter ground states. In these limits, we note that  $\phi(\tau, \tau' = 0)$  approaches

$e^{-\tau Q}|M_c|^2$ , where  $Q = E_i^0 - E_f^0$  is the energy release, so that a calculation of  $\phi(\tau, 0)$  leads directly to the closure matrix element. If we then define

$$\eta(T, \tau) \equiv \int_0^T d\tau' \phi(\tau, \tau') e^{-\tau' Q/2}, \quad (8.27)$$

and

$$M^{2\nu}(T, \tau) \equiv \frac{\eta(T, \tau) M_c^*}{\phi(\tau, 0)}, \quad (8.28)$$

it is easy to see that in the limit of large  $\tau$ ,  $(\beta - \tau - \tau')$ , and  $T$ ,  $M^{2\nu}(T, \tau)$  becomes independent of these parameters and is equal to the matrix element in Eq. (8.23).

In the first applications, Radha *et al.* calculated the  $2\nu$  matrix elements for  $^{48}\text{Ca}$  and  $^{76}\text{Ge}$  [106]. The first nucleus allowed a benchmarking of the SMMC method against direct diagonalization. A large-basis shell model calculation for  $^{76}\text{Ge}$  has long been waited for, as  $^{76}\text{Ge}$  is one of the few nuclei where the  $2\nu\beta\beta$  decay has been precisely measured and the best limits on the  $0\nu$  decay mode have been established [107, 108, 109].

The SMMC calculation for  $^{48}\text{Ca}$  was performed for the complete  $pf$  shell using the KB3 interaction and compared to a direct diagonalization using an implementation of the Lanczos algorithm. To avoid the sign problem (section 7), the SMMC result was obtained by extrapolation from a family of sign-problem-free Hamiltonian  $\hat{H}_g$  with  $g \leq 0$  and  $\chi = 4$ . For both the exact and the closure matrix elements, the SMMC and direct diagonalization results agree well for all values of  $g \leq 0$  (Fig. 8.21). Upon extrapolation to the physical value  $g = 1$  the SMMC study yields  $M^{2\nu} = 0.15 \pm 0.07$  MeV, consistent with the matrix element obtained by direct diagonalization ( $M^{2\nu} = 0.08$  [110], with the erratum in [51]). Note that the  $g$ -dependence was found to be linear at  $g \leq 0$ . However, when monitoring the  $g$ -dependence for  $g > 0$  within the direct diagonalization, a small curvature in the extrapolation was found at  $g \approx 1$  which could not be detected in the SMMC results at  $g \leq 0$  and so leads to some uncertainty in the extrapolated SMMC result.

We note that the shell model estimate for the  $^{48}\text{Ca}$  lifetime [51] appears to be shorter than the recently established experimental value [111]. While this experimental lifetime might still be compatible with complete  $pf$ -shell model calculation after slight modifications of the important  $J = 0, T = 1$  and  $J = 1, T = 0$  matrix elements [112], it appears desirable to calculate the  $2\nu$  matrix element for  $^{48}\text{Ca}$  in the complete  $(0d1s)(1p0f)$  shells taking possible polarization effects into account. Such a challenging calculation is computationally feasible within the SMMC.

To monitor the possible uncertainty related to the  $g$ -extrapolation in the calculation of the  $2\nu$  matrix element for  $^{76}\text{Ge}$ , SMMC studies have been performed for two quite different families of sign-problem-free Hamiltonians ( $\chi = \infty$  and  $\chi = 4$ ). The calculation comprises the complete  $(0f_{5/2}, 1p, 0g_{9/2})$  model space, which is significantly larger than in previous shell model studies [113]. The adopted effective interaction is based on the Paris potential and has been constructed for this model space using the Q-box method developed by Kuo [114].

As is shown in Fig. 8.25, upon linear extrapolation both families of Hamiltonians predict a consistent value for the  $2\nu$  matrix element of  $^{76}\text{Ge}$ . The results  $M^{2\nu} = 0.12 \pm 0.07$  and  $M^{2\nu} = 0.12 \pm 0.06$  are only slightly lower than the experimental values ( $M^{2\nu} = 0.22 \pm 0.01$ , [109]). This comparison, however, should not be overinterpreted yet, as the detailed reliability of the effective interaction is still to be checked.

It is interesting that the closure matrix element found in the SMMC calculation and the average energy denominator ( $M_c = -0.36 \pm 0.37$ ,  $\bar{E} = -3.0 \pm 3.3$  MeV and  $M_c = 0.08 \pm 0.17$ ,  $\bar{E} = 0.57 \pm 1.26$  MeV for the two families of Hamiltonians with  $\chi = \infty$  and  $\chi = 4$ , respectively) are both significantly smaller than had been assumed previously. This is confirmed by a recent truncated diagonalization study [115].

## 9 Prospects

We have presented in section 8 a sampling of results from SMMC calculations. These demonstrate both the power and limitations of the methods and the physical insights they offer. SMMC calculations, while not a panacea, clearly have certain advantages over conventional shell model approaches, particularly for properties of ground states or thermal ensembles. Of the results discussed in this review, the most significant bear on the quenching of GT strength, the pairing structure, and nuclear shapes. Many of the first applications of the SMMC approach have significant bearing on astrophysical questions.

With respect to the technical aspects of these calculations we note the following.

- SMMC methods are computationally intensive. However, computing power is becoming both less expensive and more widely available at an astonishing rate. It is a great advantage that these calculations can efficiently exploit loosely connected "farms" of work-station-class machines.
- A number of interesting physics questions require multi-shell model spaces. Among these are the origin of the apparent renormalization of  $g_A = 1$  in Gamow-Teller transitions, strengths of first-forbidden weak operators, the properties of the giant dipole resonance, and nuclear behavior at temperatures above 1.5 MeV. Preliminary SMMC studies offer circumstantial evidence that center-of-mass (CM) motion is not a significant concern for some of the operators of interest. This is not too surprising at finite temperature, since the CM is only three degrees of freedom (far fewer than the internal dynamics).
- We lack the capability to treat odd- $A$  or odd-odd  $N \neq Z$  systems at temperatures below  $\sim 800$  keV, because of "sign" problems in the Monte Carlo sampling. However, meaningful results are possible at modest temperatures for such nuclei, as exemplified by the  $^{51}\text{V}$ ,  $^{55}\text{Mn}$ , and  $^{59}\text{Co}$  calculations in section 8.1. Similar problems prevent spin projection, which would enable yrast spectroscopy.

Otsuka and collaborators [116] have recently proposed a hybrid scheme whereby SMMC methods are used to select a many-body basis, which is then employed in a conventional diagonalization. The sign problems alluded to above are absent, and detailed spectroscopy is possible. Test applications to boson problems have shown some promise, although the utility for realistic fermion systems remains to be demonstrated. It is unfortunate that explicit angular momentum projection apparently plays an important role in these methods, as the numerical effort of that procedure increases strongly with the size of the model space.

Additional physics results in finite nuclei that should emerge in the future include: more realistic electron capture rates in pre-supernova conditions, the double-beta decay matrix

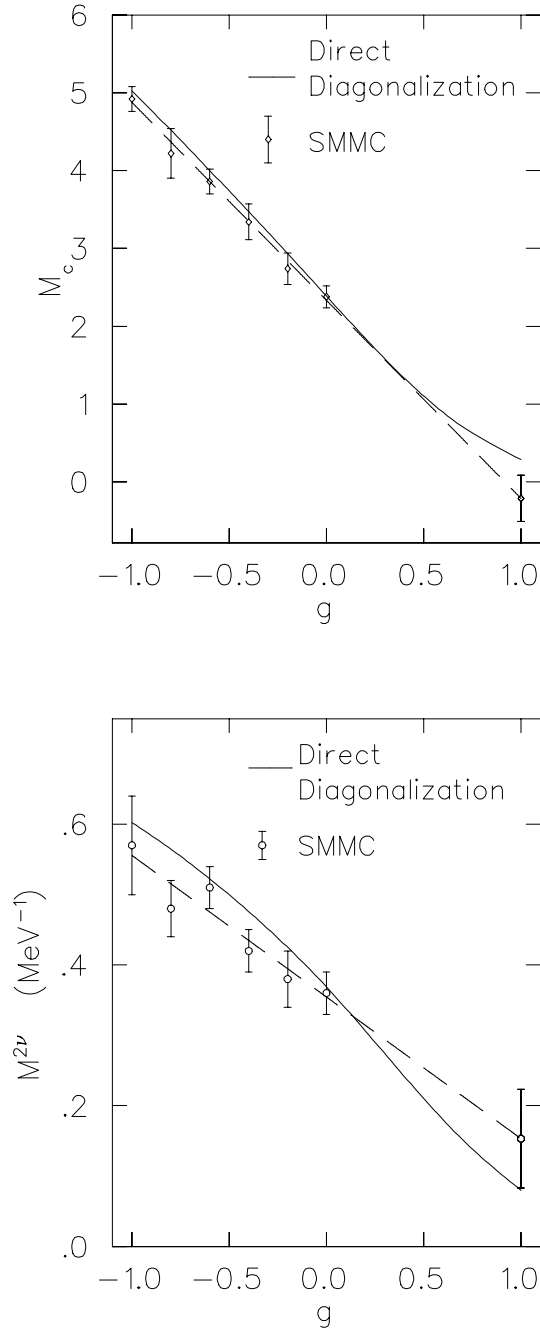


FIG 8.24. The closure matrix element (upper panel) and the exact matrix element (lower panel) for the double- $\beta$  decay of  $^{48}\text{Ca}$  as a function of  $g$ -values in the adopted family of Hamiltonian (see text). The SMCC results (open circles) are compared to the direct diagonalization (solid circles). The SMCC result at  $g = 1$  has been obtained by linear extrapolation (from [106]).

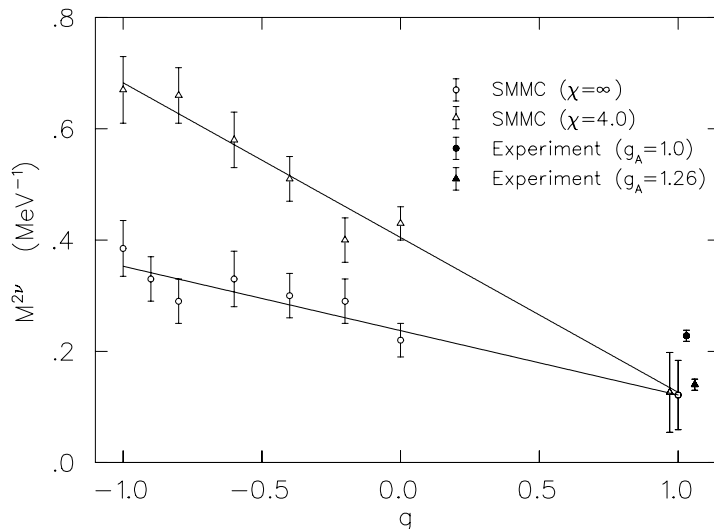


FIG 8.25. The  $2\nu$  matrix element for  $^{76}\text{Ge}$  calculated within SMMC studies based on two families of Hamiltonians which are free of sign problems. The physical values are obtained by linear extrapolation to  $g = 1$ . The experimental value for this matrix element [109] is indicated by the diamond (from [106]).

elements for candidates other than  $^{76}\text{Ge}$ , systematic studies of rare earth nuclei at finite temperature and spin, studies to improve the effective interactions used, tests of such models as the IBM and RPA, and predictions of nuclear properties far from  $\beta$ -stability.

The ground state and thermal properties of nuclear matter are another intriguing application of SMMC methods. One approach is to use single particle states that are plane waves with periodic boundary conditions and a G-matrix derived from a realistic inter-nucleon interaction; the formalism and algorithms we have presented here are then directly applicable. An alternative approach is to work on a regular lattice of sites in coordinate space and employ Skyrme-like effective interactions that couple neighboring sites; the calculation is then similar to that for the Hubbard model for which special techniques must be used to handle the large, sparse matrices involved [24]. Both approaches are currently being pursued.

## **Acknowledgements**

Many people have contributed to the development and initial application of SMMC methods. These include Y. Alhassid, C. Johnson, G. Lang, W.E. Ormand, P.B. Radha, and, more recently, M.T. Ressel, P. Vogel, J. White, and D.C. Zheng. T. Kuo supplied us with effective interactions for those large model spaces that had never been treated before. We also wish to thank A. Arima, G. Bertsch, A. Brown, B. Mottelson, W. Nazarewicz, and A. Poves for useful discussions. Finally, we would like to thank P. Vogel and G.E. Brown for careful and critical reading of the final manuscript.

This work was supported by NSF grants PHY91-15574, PHY94-12818, and PHY94-20470. Computational cycles on the Intel DELTA and PARAGON were provided by the Concurrent Supercomputing Consortium at Caltech. Cycles were also provided on the VPP500, a vector parallel processor at the RIKEN supercomputing facility, and on the IBM SP-2 at the Maui HPCC facility. We thank Drs. I. Tanihata and S. Ohta for their assistance with the former. The Maui HPCC facility is sponsored in part by the Phillips Laboratory, Air Force Materiel Command, USAF, under cooperative agreement number F29601-93-2-0001.

# A Appendix: Properties of one-fermion operators

In this appendix, we review some of the properties of one-fermion operators relevant to Monte Carlo methods for the shell model. A more complete discussion can be found in Ref. [27].

Consider a set of  $N_s$  single-particle states labeled by  $\alpha = 1, \dots, N_s$ . Corresponding to each state  $\alpha$  are anticommuting fermion creation ( $a_\alpha^\dagger$ ) and annihilation ( $a_\alpha$ ) operators that satisfy

$$\{a_\alpha, a_\beta\} = \{a_\alpha^\dagger, a_\beta^\dagger\} = 0; \quad \{a_\alpha^\dagger, a_\beta\} = \delta_{\alpha\beta}. \quad (\text{A.1})$$

The associated hermitian number operators,  $\hat{n}_\alpha \equiv a_\alpha^\dagger a_\alpha$ , are mutually commuting, and satisfy the operator identity

$$\hat{n}_\alpha^2 = \hat{n}_\alpha, \quad (\text{A.2})$$

implying that their eigenvalues are either 0 or 1; i.e., a single-particle state can either be empty or occupied. The total number operator is  $\hat{N} = \sum_\alpha \hat{n}_\alpha$ . The fermion vacuum,  $|\mathbf{0}\rangle$ , is annihilated by all operators,  $a_\alpha|\mathbf{0}\rangle = 0$ , and so satisfies  $\hat{n}_\alpha|\mathbf{0}\rangle = 0$ ; i.e., all single-particle states are empty.

A complete orthonormal basis of  $A$ -fermion states can be constructed by choosing  $A$  different single-particle states to be occupied (let them be labeled by  $i = 1, \dots, A$ ), and then constructing the Slater determinant

$$|\Phi\rangle = a_1^\dagger a_2^\dagger \dots a_A^\dagger |\mathbf{0}\rangle, \quad (\text{A.3})$$

where the product is over all occupied states and the order of the creation operators follows a fixed, predetermined sequence. This state is an eigenvalue of each  $\hat{n}_i$  with eigenvalue 1 or 0, depending upon whether the state  $i$  is occupied or not.

One-body operators are defined as

$$\hat{O} = \sum_{\alpha\beta} \mathbf{O}_{\alpha\beta} a_\alpha^\dagger a_\beta, \quad (\text{A.4})$$

where the  $\mathbf{O}_{\alpha\beta} \equiv \langle \alpha | O | \beta \rangle$  are the one-body matrix elements. (Note that we must be careful to distinguish between the second-quantized operator  $\hat{O}$  and the  $c$ -number matrix of its one-body matrix elements,  $\mathbf{O}$ .) When acting on a determinant, a one-body operator produces a linear combination of other determinants that differ from the original by at most the occupation number of one state.

Operators and determinants can be defined in any orthonormal single-particle basis. Suppose that there is a second basis  $\lambda\mu \dots$  distinct from the  $\alpha\beta \dots$  basis, and let  $T_{\lambda\alpha} = \langle \lambda | \alpha \rangle$  be the  $N_s \times N_s$  unitary matrix effecting transformations between them. Then the creation operators transform as

$$a_\lambda^\dagger = \sum_\alpha T_{\lambda\alpha} a_\alpha^\dagger \quad (\text{A.5})$$

and one-body matrix elements transform as

$$\mathbf{O}_{\lambda\mu} = \sum_{\alpha\beta} T_{\lambda\alpha} \mathbf{O}_{\alpha\beta} T_{\mu\beta}^*. \quad (\text{A.6})$$

Of particular relevance for SMMC are the exponentials of one-body operators. Consider the action of  $\hat{u} = e^{-\Delta\beta\hat{h}}$  on a determinant of the form (A.3), where  $\hat{h}$  is a one-body hamiltonian. Since the Baker-Hausdorff identity implies that

$$e^{-\Delta\beta\hat{h}}a_1^\dagger e^{\Delta\beta\hat{h}} = \sum_{\beta} [e^{-\Delta\beta\mathbf{h}}]_{\alpha 1} a_{\alpha}^\dagger \equiv \sum_{\beta} \mathbf{u}_{\alpha 1} a_{\alpha}^\dagger \quad (\text{A.7})$$

and  $\hat{u}|\mathbf{0}\rangle = |\mathbf{0}\rangle$ , then

$$\hat{u}|1, 2, \dots, A\rangle = \left( \sum_{\alpha} \mathbf{u}_{\alpha 1} a_{\alpha}^\dagger \right) \left( \sum_{\beta} \mathbf{u}_{\beta 2} a_{\beta}^\dagger \right) \dots \left( \sum_{\zeta} \mathbf{u}_{\zeta A} a_{\zeta}^\dagger \right) |\mathbf{0}\rangle. \quad (\text{A.8})$$

Thus, the action of the exponential of a one-body operator on a determinant is to redefine the occupied states by the linear transformation associated with  $\mathbf{u}$ . For evolution at a finite  $\beta$ , we deal with products of exponentials of one-body operators,  $\hat{U} = \dots \hat{u}_2 \hat{u}_1$ ; the net result of this operator on a determinant is clearly a linear transformation of the occupied states by the matrix  $\mathbf{U} = \dots \mathbf{u}_2 \mathbf{u}_1$ . It then follows that the expectation value of  $\hat{U}$  in a determinantal trial function, as is required in the zero-temperature formalism, is

$$\langle \Phi | \hat{U} | \Phi \rangle = \det U_{ij}, \quad (\text{A.9})$$

where  $U_{ij}$  is the  $A \times A$  matrix of one-body quantities,  $\langle i | U | j \rangle$ .

The grand-canonical trace of  $\hat{U}$  is the sum of the expectation values in all possible many-particle states:

$$\text{Tr} \hat{U} = \sum_{A=1}^{N_s} \text{Tr}_A \hat{U}, \quad (\text{A.10})$$

where  $\text{Tr}_A$  is the canonical trace (sum over all  $A$ -particle states). The enumeration of the canonical traces is straightforward:

$$\begin{aligned} \text{Tr}_0 \hat{U} &= \langle \mathbf{0} | \hat{U} | \mathbf{0} \rangle = 1 \\ \text{Tr}_1 \hat{U} &= \sum_1 \langle 1 | \hat{U} | 1 \rangle = \text{tr} \mathbf{U} \\ \text{Tr}_2 \hat{U} &= \frac{1}{2} \sum_{12} \langle 12 | \hat{U} | 12 \rangle = \frac{1}{2} [(\text{tr} \mathbf{U})^2 - \text{tr} \mathbf{U}^2] \\ &\vdots \\ \text{Tr}_{N_s} \hat{U} &= \det \mathbf{U}. \end{aligned} \quad (\text{A.11})$$

These can be summed into the single expression

$$\text{Tr} \hat{U} = \det(\mathbf{1} + \mathbf{U}), \quad (\text{A.12})$$

which can be verified by a direct expansion in powers of  $\mathbf{U}$ . Here, the symbol  $\text{tr}$  denotes the matrix trace, while  $\text{Tr}$  is reserved for many-body traces.

We will also be interested in the thermodynamic expectation values of few-body operators. For a one-body operator  $\hat{\Omega}$ , we require

$$\langle \hat{\Omega} \rangle \equiv \frac{\text{Tr } \hat{U} \hat{\Omega}}{\text{Tr } \hat{U}}. \quad (\text{A.13})$$

This expression is most conveniently evaluated by considering the operator  $\hat{U}_\varepsilon = \hat{U} e^{\varepsilon \hat{\Omega}}$ , so that

$$\langle \hat{\Omega} \rangle = \frac{d}{d\varepsilon} \ln \text{Tr } \hat{U}_\varepsilon |_{\varepsilon=0}. \quad (\text{A.14})$$

Since  $\text{Tr } \hat{U}_\varepsilon = \det(1 + \mathbf{U} e^{\varepsilon \mathbf{\Omega}})$  and  $\det(\mathbf{A} + \varepsilon \mathbf{B}) \sim (\det \mathbf{A})(1 + \varepsilon \text{Tr } \mathbf{A}^{-1} \mathbf{B})$  to linear order in  $\varepsilon$ , we have

$$\langle \hat{\Omega} \rangle = \text{tr} \frac{\mathbf{1}}{\mathbf{1} + \mathbf{U}} \mathbf{U} \mathbf{\Omega}. \quad (\text{A.15})$$

Similarly, the expectation value of the product of two one-body operators can be found to be

$$\langle \hat{\Omega}' \hat{\Omega} \rangle = \langle \hat{\Omega}' \rangle \langle \hat{\Omega} \rangle + \text{tr} \frac{\mathbf{1}}{\mathbf{1} + \mathbf{U}} \mathbf{U} \mathbf{\Omega}' \mathbf{\Omega} - \text{tr} \frac{\mathbf{1}}{\mathbf{1} + \mathbf{U}} \mathbf{U} \mathbf{\Omega}' \frac{\mathbf{1}}{\mathbf{1} + \mathbf{U}} \mathbf{U} \mathbf{\Omega}. \quad (\text{A.16})$$

## References

- [1] M.G. Meyer, Phys. Rev. **75** (1949) 1968; O.J. Haxel, J.H.D. Jensen and H.E. Suess, Phys. Rev. **75** (1949) 1766
- [2] A. Bohr and B. Mottelson *Nuclear Structure* (Benjamin, New York, 1969, 1975)
- [3] P. Ring and P. Schuck, *The Nuclear Many-Body Problem* (Springer, New York, 1980)
- [4] U. Mosel, Nucl. Phys. **A583** (1995) 29c
- [5] M.J. Musolf, T.W. Donnelly, J. Dubach, S.J. Pollock, S. Kowalski and E.J. Beise, Phys. Rep. **239** (1994) 1
- [6] T.E.O. Ericson and W. Weise, *Pions and Nuclei* (Clarendon Press, Oxford, 1988)]
- [7] D. Frekers, D.R. Gill and J. Speth (Eds) *Physics at KAON* (Springer, Berlin, 1990)
- [8] D. Axen, D. Bryman and M. Comyn (Eds.) *The Vancouver Meeting on Particles and Fields* (World Scientific, Singapore, 1992)
- [9] P. Schwandt in *Proceedings of the International Nuclear Physics Conference* (World Scientific, Singapore, 1990)
- [10] F. Osterfeld, Rev. Mod. Phys. **64** (1992) 491
- [11] H.A. Bethe, Rev. Mod. Phys. **62** (1990) 801
- [12] W.A. Fowler, in *Les Prix Nobel-1983* (Almqvist and Wiksell International, Stockholm, Sweden, 1984), p. 88
- [13] F. Iachello and A. Arima, *The Interacting Boson Model* ( Cambridge University Press, Cambridge, 1988)
- [14] B.S. Pudliner, V.R. Pandharipande, J. Carlson and R.B. Wiringa, Phys. Rev. Lett. **74** (1995) 4396
- [15] S. Cohen and D. Kurath, Nucl. Phys. **73** (1965) 1; **A141** (1970) 145; D. Kurath, Phys. Rev. **C7** (1973) 1390; D. Kurath and D.J. Millener, Nucl. Phys. **A238** (1975) 269
- [16] B. H. Wildenthal, Prog. Part. Nucl. Phys. **11** (1984) 5
- [17] J.B. French, E.C. Halbert, J.B. McGrory, and S.S.M. Wong, Adv. Nucl. Phys. **3** (1969) 193; E.C. Halbert, J.B. McGrory, B.H. Wildenthal, and S.P. Pandya, Adv. Nucl. Phys. **4** (1971) 375
- [18] K.W. Schmid and F. Grümmer, Rep. Prog. Phys. **50** (1987) 731; F. Donau, K.W. Schmid and A. Fässler, Nucl. Phys. **A539** (1992) 403
- [19] A. Poves and A.P. Zuker, Phys. Rep. **70** (1981) 235

- [20] M. Vallieres and A. Novoselsky, Nucl. Phys. **A570** (1994) 345c
- [21] B. H. Wildenthal, in *Shell Model and Nuclear Structure: where do we stand?*, 2nd International Spring Seminar on Nuclear Physics, edited by A. Covello (World Scientific, 1988).
- [22] J. Hubbard, Phys. Lett. **3** (1959) 77; R. D. Stratonovich, Dokl. Akad. Nauk., SSSR **115** (1957) 1907 [transl: Soviet Phys. Kokl. **2** (1958) 416]
- [23] G. Sugiyama and S.E. Koonin, Ann. Phys. **168** (1986) 1
- [24] W. von der Linden, Phys. Rep. **220** (1992) 53, and references therein.
- [25] J. E. Hirsch, Phys. Rev. **B28** (1983) 4059
- [26] C.W. Johnson, S.E. Koonin, G.H. Lang and W.E. Ormand, Phys. Rev. Lett. **69** (1992) 3157
- [27] G.H. Lang, C.W. Johnson, S.E. Koonin and W.E. Ormand, Phys. Rev. **C48** (1993) 1518
- [28] W.E. Ormand, D.J. Dean, C.W. Johnson, G.H. Lang and S.E. Koonin, Phys. Rev. **C49** (1994) 1422
- [29] Y. Alhassid, D.J. Dean, S.E. Koonin, G.H. Lang and W.E. Ormand, Phys. Rev. Lett. **72** (1994) 613
- [30] R.D. Lawson *Theory of the Nuclear Shell Model* (Clarendon Press, Oxford, 1980)
- [31] K. Heyde *The Nuclear Shell Model* (Springer, Berlin, 1991)
- [32] A. DeShalit and I. Talmi *Nuclear Shell Theory* (Academic Press, New York, 1963)
- [33] P.J. Brussard and P.M.W. Glaudemans *Shell Model applications in Nuclear Spectroscopy* (North-Holland, Amsterdam, 1977)
- [34] T.T.S. Kuo and G.E. Brown, Nucl. Phys. **85** (1966) 40; T.T.S. Kuo, Ann. Rev. Nucl. Sci. **24** (1974) 101
- [35] B.R. Barrett and M.W. Kirson, Adv. Nucl. Phys. **6** (1973) 219
- [36] M.W. Jiang, R. Machleidt, D.R. Stout and T.T.S. Kuo, Phys. Rev. **C46** (1992) 910
- [37] B.A. Brown and B.H. Wildenthal, Ann. Rev. Nucl. Part. Sci. **38** (1988) 29
- [38] W. A. Richter, M. G. Vandermerwe, R. E. Julies, and B. A. Brown, Nucl. Phys. **A523** (1991) 325
- [39] M. Dufour and A. Zuker, preprint (Universite Louis Pasteur, Strasbourg, 1994)
- [40] K. Kumar and M. Baranger, Nucl. Phys. **110** (1968) 529; **A122** (1968) 27, 273, 522

- [41] P. Quentin and H. Flocard, *Ann. Rev. Nucl. Part. Sci.* **28** (1978) 523
- [42] K. Goeke and P.-G. Reinhard *Lecture Notes in Physics* (Springer-Verlag, Heidelberg) **171** (1982)
- [43] G. Bertsch and S.F. Tsai, *Phys. Rep.* **18** (1975) 126
- [44] R.R. Whitehead, A. Watt, B.J. Cole and L. Morrison, *Adv. Nucl. Phys.* **9** (1977) 123
- [45] D.A. Resler and S.M. Grimes, *Computers in Physics*, May-June (1988) 65
- [46] A. Etchegoyen, W.D.M. Rae, N.S. Godwin, W.A. Richter, C.H. Zimmerman, B.A. Brown, W.E. Ormand and J.S. Winfield, MSU-NSCL Report **524** (1985)
- [47] W. D. M. Rae, A. Etchegoyen, and B. A. . Brown, *OXBASH, The Oxford-Buenos Aires-MSU shell-model code*, Michigan State University Cyclotron Laboratory Report No. 524, 1988.
- [48] M. Vallieres, *The Nuclear Shell Model in Computational Nuclear Physics* ed. K. Langanke, J.A Maruhn, and S.E. Koonin (Springer, Berlin, 1991)
- [49] C. Lanczos, *J. Res. Nat. Bur. Stand.* **45** (1950) 55
- [50] S.E. Koonin and D.C. Meredith *Computational Physics* (Addison-Wesley, Redwood City, 1990)
- [51] E. Caurier, A.P. Zuker, A. Poves and G. Martinez-Pinedo, *Phys. Rev.* **C50** (1994) 225
- [52] E. Caurier, G. Martinez-Pinedo, A. Poves and A.P. Zuker, *Phys. Rev.* **C52** (1995) R1736
- [53] E.Y. Loh, Jr., and J.E. Gubernatis, *Electronic Phase Transitions*, ed by W. Hanke, and Yu.V. Kopaev (1992) 177
- [54] S.V. Meshkov and D.V. Berkov, *Int. J. of Mod. Phys.* **C5** (1994) 987
- [55] K. Langanke, D.J. Dean, P.B. Radha, Y. Alhassid and S.E. Koonin, *Phys. Rev.* **C52** (1995) 718
- [56] B. Lauritsen, P. Arve and G.F. Bertsch, *Phys. Rev. Lett.* **61** (1988) 2835
- [57] W.H. Press, B.P. Flannery, S.A. Teukolsky and W.T. Vetterling, *Numerical Recipes* (Cambridge University Press, Cambridge, 1986)
- [58] N. Metropolis, A. Rosenbluth, M. Rosenbluth, A. Teller and E. Teller, *J. Chem. Phys.* **21** (1953) 1087
- [59] D.J. Dean, S.E. Koonin, G.H. Lang, P.B. Radha, and W.E. Ormand, *Phys. Lett.* B317 (1993) 275

- [60] E. V. Condon and G. H. Shortley, *The Theory of Atomic Spectra*, Ch. III (Cambridge University Press, 1935).
- [61] If all single-particle orbits in the model space have the same parity,  $\pi = +1$  and the sign rule of Ref. [27] is reproduced. The sign rule of Ref. [27] holds in the Biedenharn-Rose convention, but in the calculation of the two-body matrix elements the spherical harmonics  $Y_{lm}$  should be multiplied by  $i^l$ .
- [62] A.L. Williams *et al.*, Phys. Rev. **C51** (1995) 1144
- [63] W.P. Alford *et al.*, Nucl. Phys. **A514** (1990) 49
- [64] M.C. Vetterli *et al.*, Phys. Rev. **C40** (1989) 559
- [65] S. El-Kateb *et al.*, Phys. Rev. **C49** (1994) 3129
- [66] T. Rönquist *et al.*, Nucl. Phys. **A563** (1993) 225
- [67] S.E. Koonin and K. Langanke, Phys. Lett. **B326** (1994) 5
- [68] G.F. Bertsch and I. Hamamoto, Phys. Rev. **C26** (1982) 1323
- [69] M. Ericson, A. Figureau and C. Thevenet, Phys. Lett. **45B** (1973) 19; E. Oser and M. Rho, Phys. Rev. Lett. **42** (1979) 47; I.S. Townes and F.C. Khanna, Phys. Rev. Lett. **42** (1979) 51; A. Bohr and B. Mottelson, Phys. Lett. 100B (1981) 10
- [70] D.I. Sober, B.C. Metsch, W. Knüpfer, G. Eulenberg, G. Kuchler, A. Richter, E. Spamer and W. Steffen, Phys. Rev. **C31** (1985) 2054
- [71] E. Suraud, Ch. Gregoire, and B. Tamain, Prog. Nucl. Part. Phys. **23** (1989) 357
- [72] K. Snover, Ann. Rev. Nucl. Part. Sci. **36** (1986) 545
- [73] Y. Alhassid, in *New Trends in Nuclear Collective Dynamics*, edited by Y. Abe *et al.* (Springer Verlag, New York, (1991) p. 41-91
- [74] J.L. Egido and P. Ring, J. Phys. **G19** (1993) 1; Nucl. Phys. **A388** (1982) 19
- [75] J. Dukelsky, A. Poves and J. Retamosa, Phys. Rev. **C44** (1991) 2872
- [76] D. J. Dean, P. B. Radha, K. Langanke, Y. Alhassid, S. E. Koonin, and W. E. Ormand, Phys. Rev. Lett. **72** (1994) 4066
- [77] K. Langanke, D.J. Dean, P.B. Radha, and S.E. Koonin, submitted to Nucl. Phys. A
- [78] O. Civitarese, G. G. Dussel, and A. P. Zuker, Phys. Rev. **C40** (1989) 2900
- [79] M. B. Aufderheide, I. Fushiki, S. E. Woosley, and D. H. Hartmann, Astrophys. J. Suppl. 91 (1994) 389
- [80] R. Schneider *et al.*, Nucl. Phys. **A588** (1995) 191c

- [81] M. Lewitowicz *et al.*, Nucl. Phys. **A588** (1995) 197c
- [82] A. Plochocki *et al.*, Z. Phys. A **342** (1992) 43
- [83] L.D. Skouras and P. Manakos, J. Phys. G **19** (1993) 731
- [84] B.A. Brown and K. Rykaczewski, Phys. Rev. **C50** (1994) R2270
- [85] I.S. Towner, Nucl. Phys. A **444** (1985) 402
- [86] I.P. Johnstone, Phys. Rev. **C44** (1991) 1476
- [87] D.J. Dean, S.E. Koonin, T.T.S. Kuo, K. Langanke and P.B. Radha, Phys. Lett. (in press)
- [88] W.D. Myers and W.J. Swiatecki, preprint LBL-36803; UC-413 (1994)
- [89] G.M. Fuller, W.A. Fowler and M.J. Newman, ApJS **42** (1980) 447; **48** (1982) 279; ApJ **252** (1982) 715; **293** (1985) 1
- [90] M.B. Aufderheide, S.D. Bloom, D.A. Resler and G.J. Mathews, Phys. Rev. **C47** (1993) 2961; Phys. Rev. **C48** (1993) 1677
- [91] G.E. Brown, in *Nuclei in the Universe*, ed. M.W. Guidry and M.R. Strayer (Hilger, London, 1993)
- [92] P. Donati, P.M. Pizzochero, P.F. Bortignon and R.A. Broglia, Phys. Rev. Lett. **72** (1994) 2835
- [93] D.J. Dean, S.E. Koonin, K. Langanke and P.B. Radha, Phys. Lett. **B356** (1995) 429
- [94] M.A. Preston and R.K. Bhaduri, *Structure of the Nucleus* (Addison-Wesley, Reading, MA 1975).
- [95] S. Levit and Y. Alhassid, Nucl. Phys. **A413** (1984) 439
- [96] J.D. Jackson, *Classical Electrodynamics* (Wiley, New York, 1962).
- [97] L. Willets and M. Jean, Phys. Rev. **102** (1956) 788
- [98] O.K. Vorov and V.G. Zelevinsky, Nucl. Phys. A **439** (1985) 207
- [99] W. Krips *et al.*, Nucl. Phys. A **529** (1991) 485
- [100] T. Otsuka, Nucl. Phys. A **557** (1993) 531c
- [101] Y. Alhassid, G.F. Bertsch, D.J. Dean, and S.E. Koonin, submitted to Phys. Rev. Lett. (1995).
- [102] R. Broglia, D.R. Bes and B.S. Nilsson, Phys. Lett. B **50** (1974) 213
- [103] R. Wyss and W. Nazarewicz, private communication.

- [104] S. Raman *et al.*, Atomic Data and Nuclear Data Tables **36** (1987) 1
- [105] W. Gast *et al.*, Z. Phys. A **318** (1984) 123
- [106] P.B. Radha, D.J. Dean, S.E. Koonin, T.T.S. Kuo, K. Langanke, A. Poves, J. Retamosa and P. Vogel, submitted to Phys. Rev. Lett. (September 1995)
- [107] A.A. Vasenko *et al.*, Mod. Phys. Lett. **A5** (1990) 1229
- [108] F.T. Avignone *et al.*, Phys. Lett. **B256** (1991) 559
- [109] M. Beck *et al.*, Phys. Rev. Lett. **70** (1993) 2853; A. Balysh *et al.* Phys. Lett. **B322** (1994) 176
- [110] E. Caurier, A. Poves and A.P. Zuker, Phys. Lett. **B252**, (1990) 13
- [111] P. Vogel, private communication
- [112] A. Poves, P.B. Radha, K. Langanke and P. Vogel, Phys. Lett. B, **B361** (1995) 1
- [113] W.C. Haxton and G.J. Stephenson Jr., Prog. in Part. and Nucl. Phys. **12** (1984) 409
- [114] T.T.S. Kuo and E. Osnes, *Lecture Notes in Physics* **364** (Springer-Verlag, Berlin, 1990) 1
- [115] E. Caurier, F. Nowacki, A. Poves and J. Retamosa, preprint (Universite Louis Pasteur, Strasbourg; Universidad Autonoma de Madrid (January 1996)
- [116] M. Honwa, T. Mizusaki and T. Otsuka, Phys. Rev. Lett. **75** (1995) 1284